1-1-2019

# The Pleistocene geoarchaeology and geochronology of Con Moong Cave, North Vietnam: Site formation processes and hominin activity in the humid tropics

Conor Mcadams
*University of Wollongong*, cm065@uowmail.edu.au

Mike W. Morley
*Oxford Brookes University*, mmorley@uow.edu.au

Xiao Fu
*Zhejiang University*

Alexander Kandyba
*Russian Academy of Sciences*

Anatoly Derevianko
*Altai State University*

*See next page for additional authors*

# The Pleistocene geoarchaeology and geochronology of Con Moong Cave, North Vietnam: Site formation processes and hominin activity in the humid tropics


## Abstract

This paper presents the results of geoarchaeological and geochronological investigations at Con Moong Cave, North Vietnam. Beneath the published, terminal Pleistocene sequence, recent excavations have uncovered a ~5 m stratigraphic sequence containing flaked stone artifacts and sedimentary features that indicate extensive post-depositional change. As the effects of tropical conditions on Pleistocene cave sediments are poorly resolved, a range of complementary techniques was selected to reconstruct the nature of on-site sedimentation and occupation, while assessing the taphonomy of archaeological and palaeoecological materials. Our approach incorporates microstratigraphic, geochemical and sedimentological analyses, using optically stimulated luminescence (OSL) dating to estimate the time of sediment deposition in the cave. This case study has broad application to tropical zones worldwide. Sedimentation began in early Marine Isotope Stage (MIS) 4, while micromorphologically observed human occupation commenced before 42 thousand years ago (ka). By placing our results within the context of published, high-resolution regional records of climate, we demonstrate that on-site rhythms of Pleistocene occupation correlated with environmental changes in the region. During MIS 3, episodic abandonment of the site coincided with periods of drier conditions, while rapid climate fluctuations in MIS 2 corresponded with short-lived occupation events and a switch to predominantly geogenic deposition in the cave.



## Publication Details

Mcadams, C., Morley, M. W., Fu, X., Kandyba, A. V., Derevianko, A. P., Nguyen, D. T., Doi, N. G. & Roberts, R. G. (2019). The Pleistocene geoarchaeology and geochronology of Con Moong Cave, North Vietnam: Site formation processes and hominin activity in the humid tropics. Geoarchaeology: an international journal, Online First 1-26.



## Authors

Conor Mcadams, Mike W. Morley, Xiao Fu, Alexander Kandyba, Anatoly Derevianko, Dong Nguyen, Nguyen Doi, and Richard G. Roberts

# The Pleistocene geoarchaeology and geochronology of Con Moong Cave, North Vietnam: site formation processes and hominin activity in the humid tropics

Conor McAdams[1,*], Mike W. Morley[1,†], Xiao Fu[1,‡], Alexander V. Kandyba[2], Anatoly P. Derevianko[2], Dong Truong Nguyen[3], Nguyen Gia Doi[3], Richard G. Roberts[1,4].

[1]Centre for Archaeological Science, School of Earth, Atmospheric and Life Sciences, University of Wollongong, Wollongong, NSW 2522, Australia; [2]Institute of Archaeology and Ethnography, Siberian Branch of the Russian Academy of Sciences, Novosibirsk 630090, Russia; [3]Vietnamese Institute of Archaeology, Vietnam Academy of Social Sciences, Hanoi, Vietnam; [4]Australian Research Council Centre of Excellence for Australian Biodiversity and Heritage, University of Wollongong, Wollongong, NSW 2522, Australia.

*Corresponding author, email: cm065@uowmail.edu.au

† Present address: College of Humanities, Arts and Social Sciences, Flinders University, Adelaide, SA 5001, Australia

‡ Present address: School of Earth Sciences, Zhejiang University, Hangzhou 310027, China



**Conflict of interest statement**

The authors have no conflicts of interest to declare.

**Data availability statement**

The data that support the findings of this study are available from the corresponding author upon reasonable request.

**Abstract**

This paper presents the results of geoarchaeological and geochronological investigations at Con Moong Cave, North Vietnam. Beneath the published, terminal Pleistocene sequence, recent excavations have uncovered a ~5 m stratigraphic sequence containing flaked stone artefacts and sedimentary features that indicate extensive post-depositional change. As the effects of tropical

conditions on Pleistocene cave sediments are poorly resolved, a range of complementary techniques was selected to reconstruct the nature of on-site sedimentation and occupation, while assessing the taphonomy of archaeological and palaeoecological materials. Our approach incorporates microstratigraphic, geochemical and sedimentological analyses, using optically stimulated luminescence (OSL) dating to estimate the time of sediment deposition in the cave. This case study has broad application to tropical zones worldwide.

Sedimentation began in early Marine Isotope Stage (MIS) 4, while micromorphologically-observed human occupation commenced before 42 thousand years ago (ka). By placing our results within the context of published, high-resolution regional records of climate, we demonstrate that on-site rhythms of Pleistocene occupation correlated with environmental changes in the region. During MIS 3, episodic abandonment of the site coincided with periods of drier conditions, while rapid climate fluctuations in MIS 2 corresponded with short-lived occupation events and a switch to predominantly geogenic deposition in the cave.

**Keywords:** Micromorphology; Guano; Southeast Asia; Sediment diagenesis; Geochemistry



## 1. Introduction

The late Pleistocene (~130–14 ka; Lisiecki and Raymo, 2005) prehistory of mainland Southeast Asia (MSEA) remains poorly resolved due to a paucity of dated fossil and archaeological records (Marwick, 2009; Dennell and Porr, 2014; Morley, 2017; Rabett, 2018). Hominin fossils in MSEA are restricted to heavily-worn teeth or bone fragments, predominantly found in cave breccias or other sediments with uncertain depositional histories or equivocal chronologies. Recent fossil discoveries have pushed back the projected arrival of anatomically modern humans (AMH) in the region into Marine Isotope Stage (MIS) 4, 57 thousand years ago (ka) or earlier (Demeter et al., 2017; Westaway

et al., 2017; Rabett, 2018; Shackelford et al., 2018), while morphological and genetic studies of fossil and modern populations hint at a complex history of interactions between diverse hominin species, including successive waves of modern humans (Liu et al., 2015; Bae et al., 2017; Corny et al., 2017; Sikora, 2017; Lipson et al., 2018; McColl et al., 2018).

Archaeological evidence related to the environmental context and the settlement and subsistence practices of the pioneering communities of modern humans remains scant. While Pleistocene lithic assemblages are relatively common in Southeast Asia, they are frequently from unstratified contexts or associated with tenuous stratigraphic relationships (Brumm and Moore, 2012). Upper Pleistocene flaked tool assemblages in the region show remarkably limited variation across a vast geographic and temporal expanse (Marwick, 2018), but a shift in manufacturing practice from small flakes to unifacially flaked cobbles, the so-called "Hoabinhian phenomenon," is evident in MSEA (Van Tan, 1997). In North Vietnam, such assemblages are often associated with shell middens in cave sites such as Con Moong Cave (Thong, 1980; Su, 2009) and Hang Boi (Rabett et al., 2011; Moser, 2012), dating to the terminal Pleistocene and later. However, new discoveries across MSEA have blurred the temporal and geographical boundaries of this technological change, rendering the "Hoabinhian" a nebulous archaeological concept, with no demonstrated environmental or economic driver (Ji et al., 2016; Marwick, 2018). As research across Southeast Asia suggests communities employed complex, forest-based procurement strategies from ~40 ka and earlier (Barker et al., 2007; Hunt et al., 2012; Hunt and Barker, 2014; O'Connor and Bulbeck, 2014; Piper and Rabett, 2014; Roberts et al., 2015a; Bae et al., 2017; Rabett, 2018; Wedage et al., 2019), the vectors and chronology of hominin dispersal and adaptation within MSEA persist as enigmas.

Elevated temperatures and high, seasonal precipitation impact on archaeological records in tropical regions worldwide through accelerated weathering and erosion or diagenetic alteration of archaeological material (Anderson, 1997; Barker et al., 2005; Wurster and Bird, 2016; Morley, 2017;

Morley and Goldberg, 2017; O'Connor et al., 2017). Caves mitigate weathering processes and as such, they are the major archaeological resource in tropical zones. Nevertheless, geoarchaeological research has demonstrated that caves are taphonomically complex spaces, due to the interaction of diverse depositional and post-depositional agencies within a confined space (Weiner et al., 1993; Karkanas et al., 2000; Stiner et al., 2001; Goldberg and Bar-Yosef, 2002; Goldberg and Sherwood, 2006; Mallol and Goldberg, 2017; Morley and Goldberg, 2017; Morley et al., 2017). The small body of geoarchaeological research targeting caves in Southeast Asia suggests that tropical conditions may have a profound effect upon archaeological site formation processes (Barker et al., 2007; Lewis, 2007; Bacon et al., 2008; Gillieson, 1986; Mijares et al., 2010; Morley, 2017; Rabett et al., 2017; Stephens et al., 2017; cf. Shahack-Gross, 2017). Recent investigations and regional reviews demonstrate the potential of microstratigraphic assessment to refine interpretations of environmental context, chronology and hominin behaviour (Kourampas et al., 2009; Hunt and Barker, 2014; Sutikna et al., 2016; Clarkson et al., 2017; Mallol and Mentzer, 2017; Morley, 2017; Morley et al., 2017), but site-scale to micro-scale geoarchaeological methodologies are not yet routinely employed in MSEA or other tropical regions. As these sites have the potential to address archaeological questions of global significance (Barker et al., 2007; Pääbo, 2015; Reyes-Centeno, 2016; Rabett, 2018), the development of a geoarchaeological framework of interpretation tailored to the taphonomic, stratigraphic and diagenetic factors active under humid tropical conditions is critical (Morley and Goldberg, 2017).

Con Moong Cave (Thong, 1980; Su, 2009; Higham, 2014), henceforth CMC, is located in Cúc-phương National Park, Thanh Hóa province, North Vietnam (Fig. 1a–c). It is a key site for understanding the terminal Pleistocene and Holocene archaeology of MSEA and also provides the opportunity to understand of the effects of tropical conditions upon Pleistocene cave sediments more generally. Here we present the results of a multi-parameter, geoarchaeological and geochronological study of the Pleistocene sediments excavated at CMC. We investigate the site's depositional and post-

depositional history, generating age determinations on the sediments using radiocarbon and single-grain optically stimulated luminescence (OSL) dating. By combining field observations, sediment micromorphology (microstratigraphy) and a range of sedimentological, geochemical and mineralogical characterisations, we systematically explore the processes of archaeological site formation, preservation and degradation in this humid tropical environment. We contextualise the reconstructed depositional history through reference to published regional palaeoecological reconstructions and assess the relationship between sedimentation and geomorphic change, regional shifts in Pleistocene climate and human occupation of CMC.

## 2. Con Moong Cave: climatic, geomorphological and archaeological context

MSEA is situated at the interface between two Asian monsoon subsystems: the Indian Ocean monsoon and the East Asian monsoon (Wang, 2002; Wang et al., 2005; Chabangborn et al., 2018). Interactions between these monsoon subsystems are complex. The prevailing Westerlies related to the Indian Ocean monsoon transfer moisture from the Bay of Bengal to the Indochinese landmass during summer (Amory-Mazaudier et al., 2006; Nguyen-Le et al., 2014), while the subtropical high brings moisture laden-air westwards and inland from the South China Sea. Heavy rain events are associated with cyclones, which frequently form in the South China Sea and move inland from July to August (Hien et al., 2002; Sterling et al., 2006; Chabangborn et al., 2018).

Isotopic records from speleothems at Xiaobailong Cave and other sites in southern China suggest that changes in Pleistocene Indian Ocean monsoon intensity correlate with millennial-scale northern hemisphere climate fluctuations, including stadials and Heinrich events, as recognised in northern hemisphere ice cores (Cai et al., 2006; 2015; Zhang et al., 2017). Speleothem records from further east in China suggest southern hemisphere climate change was an important, additional control on Pleistocene East Asian monsoon intensity, particularly during glacial periods (Rohling et al., 2009). While Chinese speleothems provide high-resolution proxy records of precipitation for the wider

region, the resulting effects on landscape- to site-scale palaeoenvironments remain poorly resolved, due to the poor preservation of traditional palaeoecological proxies and the complex environmental mosaics that characterise MSEA (Wurster and Bird, 2016). At Niah Cave, in Borneo, Hunt et al. (2012) inferred more open environments during MIS 2, while Wurster et al. (2010) reported a spatially-varied pattern of climate-driven forest contraction across Pleistocene Sundaland. Rabett et al. (2017) and Mai Huong and Van Hai (2009) noted the persistence of limestone forest in North Vietnam during MIS 2 and the terminal Pleistocene, respectively, and Rabett et al. (2017) suggested local karst uplands may have formed forest refugia in MSEA during glacial periods.

North Vietnam is positioned on the boundary of the colliding South China and Indochina Plates (Hutchison, 2005) and at the interface between tropical and subtropical climatic zones (Kottek et al., 2006) and the South China, Indochina and Coastal Indochina biogeographic units (Nam, 1995; Sterling et al., 2006; Hall, 2009). The Hanoi basin is the dominant feature in the North Vietnam plain (Gupta, 2005), a coastal lowland surrounded by extensive and varied karst formations that have been subject to folding, faulting and neotectonic movement throughout the area's complex history of rifting and collision (Khang, 1985; Nam, 1995; Gillieson, 2005; Sterling et al., 2006). Folded and faulted Triassic limestones dominate the carbonate formations of North Vietnam, with thick limestone strata (including the Dong Giao and Muong Trai formations) stretching from the northwest border of Vietnam, along the southern extent of the Hanoi basin, where they border the upper extent of the Annamite Cordillera in the region of Huong Tich (Khang, 1985). These rocks display marked karstification due to the humid tropical and subtropical climates, dense vegetation and thick soil cover (Khang, 1985; Gillieson, 2005).

Vietnam's narrow coastal plain has been highlighted as a plausible north/south route of Pleistocene hominin dispersal (Demeter et al., 2003). Despite the regions' dense networks of caves and rich archaeological record, however, the sparsity of dated sites means any existing models remain

somewhat speculative (Marwick, 2009; Morley, 2017). Bordering this zone, the rugged karst terrain of Cúc-phương National Park has created a patchwork of climatically-diverse microenvironments that supports exceptional biodiversity with a range of intersecting floral and faunal communities, characteristic of humid tropical forest, dry tropical grasslands and temperate forest (Rugendyke and Son, 2005; Bich et al., 2009). The dominant soil types in this region are ultisols, ferric acrisols, and lithosols on steep slopes (Moormann, 1961; Sehgal, 1989; Olson and Morton, 2017), which are reflective of the udic moisture regimes driven by prevailing humid tropical and subtropical conditions (U.S. Department of Agriculture, 1997: O'Geen, 2012).

CMC is a karstic cave formed in a low hill, 147 m above sea level and part of the Dong Giao formation (Fig. 1c; Mai Huong and Van Hai, 2009; Lam and Su, 2014). The cave has two entrances (Fig. 2b): the west-facing entrance overlooks the broad valley of the Đà River, a tributary of the Red River (Su, 2009), while the southeast-facing entrance, situated higher and towards the south is associated with a large talus slope. The remains of a phreatic tube form the uppermost extent of CMC, and steep walls with scalloping indicate a subsequent episode of vadose conditions (Fig. 2a). Further palaeohydrological and geomorphic changes are indicated by relict speleothems, some of which preserve fragmentary shell-rich breccia, elevated above the current cave floor.

Excavations during the 1970s were carried out by the Vietnamese Institute of Archaeology on a slope towards the western entrance (Fig. 2b; Van Tan, 1997). These revealed a series of shell middens, occupation deposits and burials associated with a late Pleistocene, “Son Vian” flaked tool assemblage, a terminal Pleistocene to Holocene “Hoabinhian” assemblage and a Holocene “Bac Sonian” early-farmer assemblage, respectively (Thong, 1980; Mai Huong and Van Hai, 2009; Su, 2009). The 2008–2014 trench sits southeast and downslope of the 1970s trenches. Here, excavations undertaken by researchers from the Russian Academy of Sciences and the Vietnamese Institute of Archaeology have revealed a series of underlying Pleistocene deposits associated with lithics,

combustion residues and a suite of sedimentary features that indicate significant physical and chemical post-depositional alteration of the sediments (Fig. 3a,b; Derevianko et al. 2012a; 2012b; 2014)

## 3. Methods

This paper presents the results of geoarchaeological and geochronological analyses, applied to the sediments uncovered during the 2008–2014 excavations at CMC (Figs 2b, 3a,b, 4a,b, 5). Field descriptions were recorded during excavation and sampling, then combined with micromorphological analyses targeting major stratigraphic changes. Sedimentological analyses were carried out on bulk samples ($n$ = 57), which provide numerical data related to texture, geochemistry and mineralogy, allowing the micromorphological observations to be related to the rest of the sequence.

### 3.1. Field observations

Lithostratigraphic Units (LSUs) were defined based on characteristics observed in the southeast-facing section of the 2008–2014 excavations during fieldwork (Figs 2b, 3a). These include colour, texture and sedimentary features. LSUs form the basis of site interpretation and relative chronology. All other analyses were targeted to correlate with and further resolve field observations of stratigraphic change.

### 3.2. Dating

The chronology of deposition at CMC is constrained by five radiocarbon ages and 14 OSL ages. OSL dating of individual grains was performed on all samples using a Risø DA-20 TL/OSL reader, and the equivalent dose ($D_e$) of each grain was estimated using a single-aliquot regenerative-dose procedure (Galbraith et al., 1999; Murray and Wintle, 2000). The resulting $D_e$ values of all samples are distributed around a central value, without no obvious clusters or other patterns in the data

indicative of insufficient exposure to sunlight prior to sediment deposition or discrete dose components suggestive of post-depositional disturbance (Jacobs and Roberts, 2007; Roberts et al., 2015b). Accordingly, the weighted mean $D_e$ of each sample was calculated using the central age model (Galbraith et al., 1999; Galbraith and Roberts, 2012). For all samples, beta dose rates were measured using a Risø GM-25-5 beta counter (and by inductively-coupled plasma mass spectrometry/optical emission spectroscopy for eleven of the samples) and gamma dose rates were measured in the field using an ORTEC digiDART gamma spectrometer. A more detailed summary of the results of OSL dating is provided in Supplementary Information. For additional chronological control, two charcoal samples and three freshwater gastropod shell samples were collected from the upper section of the CMC profile for radiocarbon dating (see Supplementary Information for details).

### 3.3. Micromorphological (microstratigraphic) analysis

Six blocks of undisturbed sediment were collected from CMC, targeting key stratigraphic transitions observed in the exposed profile (Figs 4a,b, 5). Blocks were dried before impregnation with polyester resin under vacuum (Macphail and Cruise, 2001). The cured blocks were cut into fifteen 10 mm-thick wafers. Spectrum Petrographics (Vancouver, WA) produced fifteen thin sections (50 mm x 75 mm), ground to standard geological thin-section thickness (~30 μm) and left without coverslips to facilitate future targeted analyses (e.g., Mentzer and Quade, 2013; Morley et al., 2017). Thin-sections were scanned in a flatbed scanner (after Arpin et al., 2002) and analysed using polarising microscopes at a range of magnifications (8 × to 200 ×). Descriptions of micromorphological features follow Stoops (2003).

### 3.4. Bulk sediment analyses

Bulk samples were taken at 10 cm depth intervals from two sediment columns, which were selected to characterise the entire sequence (Fig. 5). Samples were heated to 120°C for 2 hr (to comply with biosecurity regulations) before analyses were carried out. Particle-size analysis was carried out on a

subsample of each bulk sediment sample, with the <2 mm fraction measured for the particle-size distribution. Analysis was carried out using a Malvern Mastersizer 2000, with the ultrasonic probe used throughout measurement and water as a dispersant. Some of the remaining raw sample was homogenised in a TEMA rock crusher. While sedimentological and geochemical analyses are often performed on the <2 mm fraction, the extent of diagenetic changes visibly affecting the coarser inclusions suggested that chemical alteration was not restricted to the fine fraction.

Portable X-Ray fluorescence (pXRF) measurements of multi-element concentrations were taken from each sample, within a polyethelene sample bag, using a hand-held Thermo Niton XL3T analyser. Results are reported in ppm (µg/g) following internal machine calibration. As no matrix-matched standards were available at the time of publication only qualitative analyses and observations are reported here. X-ray diffraction (XRD) analyses were carried out on the homogenised sediment samples from the two columns, stratigraphically equivalent to the positions of manufactured thin sections, and from lithostratigraphic units E and F, which were not targeted for micromorphological analysis. The mineralogy of these samples was assessed using µPDSM (Micron Powder Diffraction Search Match), by comparing the sample diffractograms to a reference library of mineral phases.

Loss on ignition (LOI) analysis was carried out to determine two values, the percentage LOI for the organic fraction (%LOI organic) and the percentage LOI at 1000° C (%LOI 1000° C). %LOI organic was determined by heating dried and pre-weighed samples to 425° C for 8 hr and measuring the associated weight loss (Davies, 1974). %LOI 1000° C was determined by subsequently heating these samples to 1000° C for 8 hr and measuring the associated weight loss. %LOI 1000° C is a useful indicator of carbonate content, although it is likely to include some weight loss related to dehydration of clays and other minerals (Heiri et al., 2001).

Statistical analyses and graphical representation of results were carried out using R and RStudio (R Core Team, 2013)

## 4. Results

A summary of the results is presented below and in Tables 1–3. Details of dating and thin-section micromorphology are presented in the Supplementary Information along with the raw data from the sedimentological investigations.

### 4.1. Dating

Sediment ages range from ~74 ka to ~19 ka (the lower parts of LSUs B and T, respectively; Fig. 5). Table 1 summarises the ages of all samples and detailed results are presented in Supplementary Information (Figs S1–S3; Tables S1–S4). The OSL ages are consistent with stratigraphic order, three samples from LSU F (CMC14-12, CMC18-1, CMC18-2) returned younger ages than that of CMC14-11 from the overlying LSU G although the age differences are not significant at 2σ. The radiocarbon ages are also mostly stratigraphically consistent; an exception is the sample V14-4 from the lower part of LSU P, which returned an age younger than those of two overlying samples, V14-3 from stratigraphically higher in LSU P and V14-2 from LSU R. The OSL age for sample CMC14-3 from LSU S is a few millennia older than radiocarbon ages for the underlying sediments, but all of the age estimates for LSUs O–T fall within MIS 2.

### 4.2. Field observations and micromorphology (microstratigraphy)

The 2008–2014 excavations at CMC revealed a sequence of Pleistocene deposits that extend a further ~5m below the previously published sequence. On field observation alone, these deposits were divided into two main aggradational phases, separated by a sloping contact (Figs 3a,b, 5; Table 1). The lowest phase consists of an undated basal diamict, LSU A, overlain by a ~2.5 m-thick suite of silts and clays, LSUs B–F (Figs 3a,b, 4a), with OSL ages ranging from 73.9 ± 9.9 to 40.3 ± 3.3 ka

(uncertainties at 1σ). Macroscopic features in LSUs B, C and D include dense concentrations of nodules, faunal voids and flame/load structures (Fig. 3b), which indicate the sediments have been subject to extensive physical deformation and diagenetic change under very wet conditions. In LSU F, faunal burrowing is so extensive that its stratigraphic relationships to other units, particularly LSU G, have been obscured and the associated age estimates must be treated with some caution (Fig. 3a, 5; Table 1). We interpreted the sloping, upper surface of this LSU F as a stratigraphic unconformity, noting that the varied sedimentary records in caves are frequently subject to depositional hiatuses, truncation, and other forms of reworking (Hunt et al., 2015; Sutikna et al., 2016; Mallol and Goldberg, 2017; Morley et al, 2017; O'Connor et al., 2017).

Overlying this lower aggradational phase, a sequence of horizontally bedded deposits (LSUs G–V) contains varied features, including bone, shell and combustion residues (Figs 3a,b, 4b), indicative of sedimentation in a drier cave-floor environment and of potential hominin activity. These sediments are generally coarser than the underlying layers, returning OSL ages that span the period from 51.3 ± 5.2 ka to 26.0 ± 1.3 ka and radiocarbon ages from LSUs O–T of ~22-19 ka (Table 1). While indicators of post-depositional alteration are less pronounced in this upper aggradational phase, pink and yellow colouration of the cave sediments, as visible in LSUs M and K (Fig. 4b), is suggestive of guano content (Shahack-Gross et al., 2004; Bird et al., 2007). For detailed micromorphological results, see Supplementary Information (Table S6).

#### *4.2.1. Sample MM3: LSU A and LSU B boundary*

The location of sediment block MM3 was chosen to resolve the interface between LSU A, a basal diamict containing gravel-sized clasts, and overlying LSU B, a reddish-brown silt/clay (Figs 4a, 6a–c). The micromorphology shows that LSU A has a poorly sorted spongey matrix, including phosphatised rock fragments, soil aggregates and biomineral pseudomorphs (Fig. 6d–g).

LSU B lower consists of spongey, oxide-stained, isotropic silt and dusty clays, with phosphatised gravels concentrated towards the lower boundary (Fig. 6b,c). Laminations are visible in a restricted fabric unit (<5% of groundmass) in MM3C upper (Fig. 6c), and concentrations of lenticular gypsum crystals are present, infilling rounded voids and partially infilling passage features (Fig. 6i,j). Cracked, rounded clay-rich aggregates are recorded throughout the groundmass (Fig. 6k).

### *4.2.2. MM2: LSU B and LSU C interface*

MM2 is taken from the diffuse interface between LSU B upper, a red/brown deposit containing interbedded lenses of grey/black silt/clay, and LSU C, which is dominated by grey silt (Figs 4a, 7a–c). Thin-section MM2A contains a lower fabric unit that is similar to LSU B lower, as visible in MM3B/MM3C (Section 4.2.1). The overlying fabric unit consists of rounded, greyish nodules (<2 mm in diameter) within a spongey groundmass of red/brown to grey/brown silts (Fig. 7a,d,e), with clays restricted to rounded, sand-sized nodules (Fig. 7e,g,h). Above this fabric unit the spongey groundmass is dominated by red/brown, isotropic silt and dusty clays.

A diffuse interface between LSU B and LSU C is observed in MM2C (Fig. 7c), where within a spongey groundmass of red/brown and grey/brown isotropic silts, concentrations of grey silt grade upwards (from 30% to 80% of groundmass). Passage features, greyish nodules and redoximorphic features are common (Fig. 7h–k).

### *4.2.3. MM1: LSU C and LSU D interface*

Sample MM1 was extracted to resolve the irregular interface between LSU C and LSU D, associated with a dark lens (Figs 4a, 5). LSU C upper, visible in thin-sections MM1A and MM1B (Fig. 8a,b), exhibits a spongey groundmass of grey/buff silt with organic punctuations and grey, sand-sized nodules throughout. Clays form amorphous, horizontally-banded concentrations (Fig. 8b), rounded

sand-sized nodules (<2%) and multi-phase, phosphatised nodules (Fig. 8h,i). Zones of laminar fabric (<10% of groundmass) and erosive contacts are associated with clays and phosphatic nodule concentrations (Fig. 8a,d–f). Void coatings/infills include crystalline and isotropic minerals, and occasional limpid clay coatings/hypocoatings (Fig. 8g). Clay and opaline root pseudomorphs are present (Fig. 8k), as are infrequent siliceous plant microfossils and soil diatoms.

The macroscopically-visible, sloping lens at the boundary of LSU C and LSU D is visible as a series of upward-fining microlaminations in MM1C upper (Fig. 8j).

### *4.2.4. MM6: LSUs G and H*

LSUs G and H are associated with the stratigraphic unconformity that separates the lower, silt- and clay-rich sediments from the coarser, carbonate-rich overlying sediments (Figs 2b, 3a, 5). LSU G, visible in thin-section MM6A (Fig. 9a), consists of isotropic, reddish-grey/brown silt in a double-spaced, fine enaulic to gefuric fabric. The groundmass grades red towards the bottom of the slide, with increasing concentrations of soil aggregates, fragmentary clay crusts and Fe/Mn coatings/nodules (Fig. 9a). Altered sand-sized bone fragments are distributed throughout the groundmass (<2%; Fig. 9c, d), while altered sand-sized shell fragments are infrequent.

In MM6B, LSU H (Fig. 9b) displays distinct upper and lower fabric units (Fig. 9e,f). They appear similar in plane-polarised light (PPL), with grey/brown silt aggregates in a spongey fabric of ashy grey silt. In cross-polarised light (XPL) the difference in b-fabric is pronounced, forming a sharp boundary between the lower section (isotropic matrix, stipple-specked b-fabric and concentrations of Fe/Mn nodules; Fig. 9g) and the upper section (increasingly welded, micritic to sparitic calcite b-fabric, grading upwards; see Fig. 9f). Sand-sized bone fragments are present in both units (<2% of groundmass), displaying a range of alterations including calcite replacement, in-situ fracture and bioerosion (see Fig. 9h,i).

### *4.2.5. MM5: LSUs L, M and N*

Located to resolve the relationship between layers displaying pronounced pinkish and yellow colour changes (LSUs L to O; Fig. 4b), MM5A reveals an isotropic crust at the boundary between LSUs L and M (Fig. 10a,e,f). LSU L displays laminations (~2 mm thick) of welded, ashy silt, preserved as a localised fabric unit (Fig. 10c,d) within a spongey groundmass of greyish silt and microcharcoal. The overlying isotropic crust is sharply delineated, although the sediment in a restricted zone directly underneath displays a Ca-depleted, stipple-specked b-fabric (Fig. 10e,f). The overlying unit, LSU M, consists of spongey, pinkish silts (Fig. 10a,b,e) that display a stipple-specked b-fabric and weakly-expressed calcite hypocoatings. Subangular, coarse sand grains of quartz within LSU M show extensive alteration and are associated with soil aggregates.

The interfaces between LSUs M, N and O, visible in MM5B, are also evident macroscopically (Fig. 10b). LSU N is represented by an aggregate of welded, ashy micritic calcite, separating LSUs M and O (Fig. 8b). The brownish, calcareous silts of LSU O are arranged in double-spaced, fine enaulic fabrics. Fragments of mollusc shell (up to 20mm in maximum dimension) are predominantly preserved as aragonite (Fig. 10h), and infrequent sand-sized bone fragments display typical, ropey interference colours in XPL.

### *4.2.6. MM4: LSUs Q, R and S*

MM4 was placed to resolve the transitions between LSUs Q, R and S, in a zone with high concentrations of macroscopically identified combustion residues (Figs 3b, 11a). LSU Q, visible in MM4A, consists of a chaotic mix of reddish-brown and grey-brown silt/dusty clay, carbonate sand and gravel. Sand-sized shell is present, as is infrequent, sand-sized, fractured and degraded charcoal. The upper boundary is difficult to locate in thin-section, due to the spongey fabric, but is associated with increased concentrations of dusty clay throughout the groundmass.

The overlying unit, LSU R (Fig. 11a), is distinguished by a groundmass of charcoal-rich, ashy grey/brown silts. Sand-sized to silt-sized charcoal fragments exhibit fracturing, rounding and clay and calcite infills of internal voids (Fig. 11d–h). Ash rhombs form frequent groundmass components (Fig. 11c) and aragonite shell is common. Bone fragments are less common and display extensive bioerosion. Visible throughout are a range of burnt and baked clastic components, including soil aggregates, speleothem fragments, rip-up clasts and rounded concentrations of oxide-replaced organic matter.

The diffuse boundary between LSUs R and S is visible in MM4B. The groundmass reddens upwards where the fabric becomes increasingly spongey and rounded aggregates of oxidised organic matter are more abundant. The difference in b-fabric is pronounced, transitioning sharply upwards from stipple-specked to undifferentiated, with superimposed ashy calcite coatings and calcite hypocoatings arounds vughs. Coarse carbonates are present in this unit, and some carbonate rock fragments have weakly expressed reaction rims. A further ashy unit is just visible above.

### 4.3 X-ray diffraction

The results of XRD analysis (Table 2) show a shift from iron and aluminium phosphate-dominated sediments in the samples associated with MM3, MM2 and MM1, to predominantly calcium carbonate-dominated sediments in MM4 and MM5. LSU E is dominated by iron and aluminium phosphates, while LSU F chiefly comprises gypsum and bassanite. In MM6, there is a transition from calcium phosphates in LSU G and the lower part of LSU H lower, to calcium carbonate in the upper part of LSU H. Calcium phosphates are also present in LSUs M and S. Diffractograms are provided in Supplementary Information (Table S7).

### 4.4 Particle-size

Particle-size data from Column 2 show considerable variation in sediment texture, both within and between stratigraphic units (Fig. 12c). Although silt dominates the sediment (mean concentration = 70%), LSU A is poorly sorted with high concentrations of clay (minimum = 30%). The proportions of sand and silt vary throughout LSU B, reflecting its heterogeneity (Table 1; Figs 6, 7). In LSUs C and D the clay content is much lower, (median = 4.5%), while ratios of silt and clay vary considerably in LSUs E and F (Fig. 12c).

The particle-size results from Column 1 reveal generally low proportions of clay (median = 5%, maximum = 14%) and sand content varies from 8 to 37% with silt dominating (mean = 77%, minimum = 59%; Fig. 12a).

### 4.5 Loss-on-ignition

%LOI organic values are highest in Column 2 (Fig. 12a, c; LSUs A–F %LOI organic mean = 10%). Column 1 values are generally lower (mean = 4%), but LSU G has produced higher %LOI organic values than the other Column 1 samples, (maximum = 11%). %LOI 1000°C is low in LSUs A–E and LSU G, and higher in LSUs H–V, and also LSU F.

### 4.6 pXRF

Details of the pXRF results and multivariate statistical analyses are provided in Supplementary Information (Table S8; R_Code.txt). Variables (element concentrations) were omitted when returning null values (i.e., below limit of detection) or high correlation values that were most likely erroneous. Fe shows strong correlations with Zr (Spearman's, r = 0.97 n = 23 p=<0.0001) and Ti (r = 0.95, n = 23, p=<0.0001), and variable clustering suggests their variance is strongly related. P shows a strong correlation with Cu (r = 0.83, p = <0.0001, n = 23) and Zn (r = 0.71, p = <0.0001, n=23); however, clustering of variables did not group these elements.

Heirarchical clustering was carried out on the entire assemblage to identify two clusters (Fig. 12b), as suggested by plotting within cluster sum of squares. The Column 1 and Column 2 samples separated

neatly and LSUs F and G were grouped with the Column 1 samples. The groupings within the Column 2 samples reflect the mineralogical differences observed in XRD analysis (Table 2). Principal component analysis (PCA) also separated the Column 1 and Column 2 samples, with LSUs F and G forming an intermediate population (Fig. 12d). PCA indicates that the first principal component is strongly associated with K and P, and to a lesser extent with Fe and is strongly negatively associated with Ca (Table 3). A scatterplot of Ca/P values for all sampled sediments can be divided into 4 k-means clusters (Fig. 12e). Overall, Column 1 samples are enriched in Ca and depleted in P, while Column 2 samples are depleted in Ca and enriched in P. In addition to LSUs F and G, a number of other samples from Column 1, LSUs K, M, S and one sample from LSU L, may form an intermediate population.

## 5. Discussion

### 5.1. Pleistocene sedimentation at Con Moong Cave

Pleistocene sedimentation at CMC (Fig. 13) can be divided broadly into four phases, based on the combined results of micromorphological, geochemical and geochronological analyses.

- Phase 1: the poorly-resolved depositional period represented by LSU A, a diamict that accumulated prior to (and possibly during) MIS 4 and has been subject to extensive phosphatic diagenesis (Fig. 13a);
- Phase 2: the accumulation and diagenetic alteration of guano-dominated sediments under very humid conditions during MIS 4 and early MIS 3 (LSUs B–E; Fig. 13b–d);
- Phase 3: the accretion of colluvially redeposited combustion residues during prolonged periods of human occupation, punctuated by episodic abandonment and bat recolonisation during MIS 3 (LSUs G–M and possibly LSU F; Fig. 13e);

- Phase 4: a switch to predominantly geogenic sedimentation during MIS 2, with evidence for sporadic occupations by humans and bats (LSUs N–V), most likely at different times (Fig. 13f).

### *5.1.1. Phase 1: Deposition and extensive alteration of basal sediments (deposited before 73.9 ± 9.9 ka)*

LSU A has been subject to extensive bioturbation and diagenesis (Fig. 13a–c). The phosphatic alteration affecting clasts in LSU A is severe and obscures their original lithology. The geology of the extensively folded Triassic formations surrounding CMC is diverse (Nam, 1995; Quang, 2009) and similar, lithologically diverse allogenic sediments may accumulate through fluvial and colluvial processes (e.g., Gillieson, 1986).

### *5.1.2. Phase 2: Guano deposition under saturated conditions from 73.9 ± 9.9 ka*

LSUs B–G are the diagenetically altered remains of a sequence of guano deposits, dominated by suites of authigenic phosphate and sulphate minerals. Different phosphate mineral species precipitate under specific physico-chemical conditions, often related to the decomposition of guano and the development of acidic sedimentary environments (Shahack-Gross et al., 2004). They serve as useful indicators of past burial conditions and measures of the taphonomic integrity of archaeologically significant material (Karkanas et al., 2000; Bird et al., 2007; Karkanas, 2010).

LSU B was deposited on a submerged floor (Fig. 13a,b), as inferred from the laminar fabrics, Fe/Mn concentrations and the presence of vivianite, a reduced iron phosphate mineral that forms under anoxic, waterlogged conditions (Heiberg et al., 2012; Rothe et al., 2016). We are uncertain about subsequent developments in the burial environment (Fig. 13c–f), due to the apparent co-occurrence of vivianite with both leucophosphite, an iron phosphate indicating wet and very acidic conditions (Karkanas et al., 2000; cf. Tatur and Keck, 1990), and gypsum, which is a soluble sulphate mineral.

The behaviour of phosphate in extreme redox environments is poorly understood (Roden and Edmonds, 1997; Heiberg et al., 2012; Rothe et al., 2016), and it is probable that these incongruous associations result from diachronous episodes of diagenetic change related to fluctuations in sedimentary hydrology and resulting shifts in redox and pH in the burial environment (cf. Wurster et al., 2015). We suggest the gypsum crystals precipitated due to oxidation of reduced sulphide compounds during a shift to drier conditions, a process analogous to the genesis of acid sulphate soils (Mees and Stoops, 2010). As gypsum is a soluble mineral, these dry conditions may have persisted since the time of gypsum crystallisation. Alternatively, the gypsum crystals may have formed during excavation or sample preparation. The %LOI results in Table S3 may lend weight to the latter interpretation, as they suggest these lower sediments were waterlogged when initially sampled.

The OSL ages for LSU B, 73.9 ± 9.9 to 63.0 ± 7.3 ka, suggest deposition during early MIS 4. As guano continued to accumulate, an upper section formed a very wet but aerobic zone (LSU C) dated to 64.7 ± 5.5 ka (Fig. 13c). LSU C is dominated by taranakite (table 2), a phosphate mineral product of clay weathering in very wet, acidic environments (Weiner et al., 2002; Onac and Vereş, 2003; Shahack-Gross et al., 2004; Bird et al., 2007; Frost et al., 2011; Wurster et al., 2015). Erosive contacts and sorting of fines correspond with macroscopically observed flame and load structures, which are features indicative of episodic mass movements of water-saturated sediment (Gilbertson et al., 2005; Bird et al., 2007; Dykes, 2007). The stratified, grey silt lenses within LSU B (Fig. 4a; Table 1) are geochemically, mineralogically and sedimentologically similar to LSU C, indicating that a series of alternating oxic and anoxic microenvironments formed as the guano mound accumulated. These differences in sedimentary conditions may relate to fluctuating water levels or the activity of microbial decomposers.

At the lower interface of LSU D (Fig. 6j), water-sorted, clay-rich sediments have formed crusts, indicating intermittent waterlogging or ponding. Field observations show that this is a lens of material and LSU D, overall, have a similar mineral composition to LSU C (Table 2). LSU D is dated to 55.8 ± 4.8 ka (early MIS 3). No thin sections are available for LSUs E or F, but XRD analysis indicates a shift in dominance from Al/Fe phosphates in LSUs D and E, to bassanite and gypsum in LSU F. While sulphate minerals are considered less useful than phosphates as environmental indicators (Karkanas and Goldberg, 2010; Wurster et al., 2015; Mallol and Goldberg, 2017), these soluble, evaporitic species are unlikely to persist in acidic sediments with percolating water (Karkanas et al., 2000; Karkanas, 2010; Wurster et al., 2015; Karkanas, 2017). Without microstratigraphic data it is difficult to make further inferences about the environment and relative timing of the formation of these authigenic minerals in LSU F.

The ages of the three samples from layer F range from 40.3 ± 3.3 to 45.4 ± 3.3 ka. These ages are systematically younger than that of the sample from the overlying LSU G (51.3 ± 5.2 ka), but consistent at 2σ, which suggests that LSUs F and G and adjacent LSU K (42.0 ± 2.6 ka), were deposited in during the middle part of MIS 3 (50-40 ka). The stratigraphic relationship of these geochemically similar units is poorly resolved, due to the extensive bioturbation obscuring the upper boundary of LSU F (Fig. 5). The single-grain $D_e$ datasets of the three samples from LSU F show low to moderate dispersion and no discrete $D_e$ components were identified. Accordingly, LSU F and LSU G may be part of the same depositional unit that has been subject to spatially discrete post-depositional bioturbation and diagenesis. Alternatively, they may be separate units and faunal disturbance did not transport material significantly between them. If any grains were translocated between these units by bioturbation, then it would not be possible to identify the intrusive grains if their $D_e$ values are similar to those of the host deposit or if they are limited in number or emit dim OSL signals. The OSL ages therefore reflect the time of deposition of the vast majority of grains in each unit.

***5.1.3. Phase 3: Colluvial sedimentation and human occupation under drier on-site conditions***

LSUs G–M date to MIS 3 and derive from colluviation of autocthonous and allogenic sediments, including soil aggregates, carbonate spall, speleothem fragments and guano (Fig. 13e,f). An OSL age of 51.3 ± 5.2 ka was obtained for LSU G, which bears a geochemical and mineralogical fingerprint similar to that of the adjacent guano profile (Table 2; Fig. 12). The dominance of whitlockite, a calcium phosphate, and the preservation of bone and shell fragments suggest that burial conditions were less acidic than in LSUs C–E, but a moist environment is indicated by the presence of fragmentary clay coatings and redoximorphic features. Rounded soil aggregates reflect colluvial inputs from the entrance slope and possibly by faunal transport.

The overlying unit (LSU H) is an ashy, anthropogenic detrital sediment that has been subject to localised decalcification and carbonate recrystallisation due to groundwater fluctuations. A sharp interface demarcates the boundary between an upper zone of carbonate preservation (Figs 9f, 13e), and a lower, phosphatised zone that was episodically waterlogged. Groundwater passing through or over guano deposits may transport phosphatic material (Frost et al., 2011), and the position of LSU H relative to the sloping guano deposit suggests that this process was likely responsible for the observed changes (Fig. 5). The chaotic mix of bone, shell, soil aggregates and other material within LSU H suggest that it has resulted from syn-depositional dumping, colluviation and bioturbation of occupation waste, presumably derived from upslope sources near the entrance.

LSU L is an extensively bioturbated, ashy deposit. Laminar fabrics indicate slopewash processes in cave sediments (Mücher et al., 2010; Mentzer, 2014; Mallol and Goldberg, 2017), here transporting occupation debris downslope from the CMC entrance area. Micritic calcite recrystallisation is a further indicator of moist conditions in the burial environment. Deposited near the end of MIS 3 (30.8 ± 1.7ka), LSU M exhibits a pinkish, spongey groundmass and a phosphatic mineralogy, both

indicators of guano content in cave sediment, suggesting a hiatus in human occupation. Leachates from this deposit have resulted in the phosphatic crust precipitated at the boundary between LSUs L and M and in the limited zone of decalcification beneath. While calcite coatings of voids indicate carbonate-laden pore water circulation through LSU M, which would have buffered the sediment pH, the preserved range of autogenic and allogenic material (including carbonate spall and cracked, rounded soil aggregates) indicate a generally drier sedimentary environment; this would have limited the extent of guano-driven diagenetic change. The overlying unit (LSU N) is an ashy aggregate, resulting from a further, short-lived episode of human activity, with increased humidity promoting wet colluviation and carbonate recrystallisation.

***5.1.4. Phase 4: Geogenic sedimentation and sporadic occupation during MIS 2***

Overlying Phase 3, LSU O is a geogenic mix of carbonate silt and sand, with clasts including mollusc shell, reflecting a significant change in depositional regime. LSU Q, visible in MM4, is similarly geogenic and contains an increase in gravel-sized limestone spall weathered from the cave walls and roof, alongside significant proportions of rounded soil aggregates and dusty clays. Evidence for a human presence in these units is limited, suggesting less intensive occupation than that represented in LSUs H and L.

LSU R is chaotic mix of ash and charcoal-rich sediment, indicative of an ephemeral period of dumping or colluviation of human occupation waste. Ash rhombs are preserved, reflecting limited water circulation through this unit, but the incorporated charcoal has been subject to extensive humification, bioturbation and diagenesis. The poor preservation of bone, compared to aragonite shell, suggests microbial degradation is an important taphonomic process, operating even in burial environments where conditions otherwise appear favourable to biomineral preservation.

A subsequent period of site abandonment is suggested by the spongey, decalcified groundmass of LSU S, indicative of guano deposition (Bird et al., 2007). The limited diagenetic changes affecting the underlying units in phase 4 are consistent with generally drier conditions during MIS 2. Although coarse carbonates are preserved, rare bone fragments show evidence of extensive bacterial attack and reaction rims on the carbonate gravel clasts indicate some phosphatisation. Preserved ashy carbonates, visible towards the top of thin-section MM4B, suggest a subsequent episode of human occupation.

### 5.2 Human occupation of Con Moong Cave in its regional environmental context

This study provides a glimpse into the history of human settlement of North Vietnam during the late Pleistocene. During the deposition of LSUs A–E, from before and during MIS 4 until early MIS 3, our environmental reconstruction indicates a malodorous, wet and colluvially active depositional environment. It is unlikely that the inferred large bat population would co-exist with hominins at such a site (Hawkins et al., 2016), however, guano-rich burial environments are likely to remove many indicators of human occupation, including ash and bone (Weiner et al., 1995; Karkanas et al., 2000; Karkanas, 2010).

We observe an overall drier environmental signal from ~51 ka, with analysis of the less-altered sediments of LSUs H–V indicating a complex history of human activity during MIS 3 and MIS 2. The micromorphological features in LSUs M and S, both interstratified between ash layers, suggest guano deposition during periods of site abandonment by people. LSU M was deposited under drier conditions and is dated to the MIS 3/2 transition at 30.8 ± 1.7 ka. This timing is broadly coincident with an abrupt decrease in regional precipitation at 30.1 ka, observed by in the speleothem $\delta^{18}O$ record from Xiaobailong Cave in Southern China (Cai et al., 2015). LSU S is dated to 26.0 ± 1.3 ka and forms part of the sequence of LSUs O–V that were deposited during MIS2, as indicated also by the

radiocarbon chronology for LSUs O–T (22–19 ka) and the OSL age for the sediment sample from LSU Q (24.7 ± 1.6 ka).

By plotting element ratios generated from LSUs G–S against an interpolated age/depth model we can further investigate the relationship between sedimentation at CMC and the published record of regional climate from Xiaobailong Cave (Fig. 14; Cai et al., 2015). Variations in Ca/P and Ca/Fe ratio in LSUs G–V can be related to specific depositional changes at Con Moong Cave (Section 4.6). PCA demonstrates that the guano-dominated Column 2 samples and carbonate-dominated Column 1 samples can be neatly separated on the basis of their geochemical signature (Fig 12d; Table 3), particularly the ratio of Ca to P; an intermediate population including LSUs that have a mix of phosphatic guano and carbonate-rich material (LSUs F, G, K, L, M and S) represents an exception (Fig 12e).

Pinkish deposit LSU K, dated to 42.0 ± 2.6 ka and stratified below ashy LSU L (Fig. 4b; Table 1), has a similar Ca/P ratio to guano-rich LSUs M and S (Fig. 12e). This suggests an earlier episode of anthropogenic abandonment and bat colonisation, coincident with a shift to drier conditions at the end of Greenland Interstadial 12 at ~43.5 ka, as recognised by Cai et al. (2006) in Xiaobailong Cave. Our interpolated chronology suggests that the deposition of LSU L occurred during a period of greatly reduced precipitation, which Cai et al. (2006) associate with Heinrich event H4. LSU L, however, contains evidence for wet, slopewash processes, suggesting deposition during a period of humid on-site conditions, and is directly dated to 36.0 ± 1.9 ka.

During MIS 2, starting ~30 ka, the variation in sedimentary Ca/P ratio between LSUs reflects the climate instability observed in the regional record (Marwick and Gagan, 2011; Cai et al., 2015).

Anthropogenic occupation during this period was episodic, consisting of short-lived pulses of activity relative to the intensive deposition of combustion residues during MIS 3 (Fig. 4b). Ca/Fe ratios, used here as a corollary of pedogenic inputs (see Section 4.6), are lowest in LSUs with a high clay and guano content and, within the Column 1 samples, particularly those deposited during MIS 2. This may be an indicator of landscape instability and soil erosion, resulting from climate-driven, geomorphic processes operating in the catchment.

Combined, our results suggest human occupation of CMC during MIS 3 correlates with periods of strong monsoon circulation and increased precipitation, with site abandonment occurring during drier conditions. While climate instability during MIS 2 correlates with a reduced intensity of ash deposition in CMC, occupation continued sporadically and the ashy layers, burials and shell middens overlying LSU S (Table 1; Thong, 1980; Mai Huong and Van Hai, 2009; Lam and Su, 2014) suggest increasingly intense occupation approaching the terminal Pleistocene. The complex relationship between human occupation and climate recorded at CMC suggests that further analyses of excavated assemblages and biogeochemical reconstructions of environmental conditions may help resolve long-standing questions related to the origins and nature of the “Hoabinhian phenomenon (Van Tan, 1997)”, its associated shell middens and the chronology of human adaptation to the upland landscapes of MSEA. Further geochronological research in the region may also help improve the age control for the major turning points in human occupation and environmental change recorded in the cave deposits.

## 6. Conclusions

This study has demonstrated the power of an integrated geoarchaeological approach to disentangle the complex environmental and anthropogenic signals stored in tropical cave sediments. The

destructive effects of sediment transport, bioturbation and guano-driven diagenetic change are visible throughout the sequence at CMC. These processes commonly affect cave deposits in the tropics to a greater extent than those at higher latitudes (Morley, 2017; Morley and Goldberg, 2017; O'Connor et al., 2017; Shahack-Gross, 2017). The related loss of (micro)stratigraphic relationships and sedimentary constituents means that the environmental histories of the sediments cannot be reconstructed solely from micromorphological analysis of thin-sections (Mallol et al., 2009; Karkanas, 2010; Mentzer and Quade, 2013).

Our results have confirmed the efficacy of a combined approach, incorporating micromorphology and geochemical analysis, to generate detailed stratigraphic, environmental and taphonomic assessments, even where the sediments have been subject to pronounced post-depositional changes. Additionally, bulk sediment analysis using pXRF multi-element characterisation and a battery of sedimentological techniques has enabled observations made in thin-section to be supported and extrapolated to the rest of the sequence, generating a more complete model of Pleistocene sedimentation at CMC.

The unusual, observed associations between mineral species, the lack of documented analogues in present-day burial environments, and the prominent role of bacteria as taphonomic agents highlight ongoing uncertainties related to the effects of tropical conditions upon the site formation processes in caves. The features observed in the CMC sediments offer opportunities for future investigations to further illuminate the history of changing palaeoenvironments at this site and others in MSEA and also to contribute further to an interpretative framework for cave sediments in other tropical regions.

The record of human activity at CMC, and our tentative association between episodes of occupation and abandonment and changes in monsoon intensity provides novel insights in a region where current narratives of the Palaeolithic are based largely on scattered human remains and lithic finds (Marwick, 2009; Dennell and Porr, 2014; Morley, 2017; Marwick, 2018). To resolve the regional history of human–environment interactions and more fully understand the processes driving settlement, demographic change and adaptation in this diverse and challenging region, will require the combination of a range of complementary techniques and approaches, such as those used in this study.



## Acknowledgements

This research was funded by the Australian Research Council, through Australian Laureate Fellowship [FL130100116] to R. G. R., and by the University of Wollongong (UOW) through a Postgraduate Award and an International Postgraduate Research Scholarship to C.M$^{c}$A. Many thanks to A/Prof. Brian Jones at UOW, for his help with using the X-ray diffraction software. Many thanks to Prof. Paul Goldberg (UOW and Boston University) for his help and advice related to thin-section preparation and cave sediment interpretation. Thanks to Dr. Sam Lin (UOW) and A/Prof. Ben Marwick (University of Washington), for their help with R and RStudio. Thanks to Jose Abrantes (UOW) for processing samples for X-ray diffraction. We also thank the editors and our reviewers for their constructive comments.

## References

Amory-Mazaudier, C., Huy, M.L., Cohen, Y., Doumbia, V., Bourdillon, A., Fleury, R., Fontaine, B., Duyen, C.H., Kobea, A., Laroche, P., Duchesne, P.L., Viet, H.L., Truong, T.L., Viet, H.L., Menvielle, M., Chien, T.N., Xuan, A.N., Ouattara, F., Petitdidier, M., Thu, H.P.T., Xuan, T.P., Philippon, N., Tran Tihi, L., Vu Thien, H., Vila, P. (2006). Sun-Earth system interaction studies over Vietnam: An international cooperative project. *Annales Geophysicae*, *24*, 3313–3327.

Anderson, D.D. (1997). Cave archaeology in southeast Asia. *Geoarchaeology*, *12*(6), 607–638. DOI:10.1002/(SICI)1520-6548(199709)12:6<607::AID-GEA5>3.0.CO;2-2

Arpin, T.L., Mallol, C., Goldberg, P. (2002). Short contribution: A new method of analyzing and documenting micromorphological thin sections using flatbed scanners: Applications in geoarchaeological studies. *Geoarchaeology*, *17*(3), 305–313. DOI:10.1002/gea.10014

Bacon, A.-M., Demeter, F., Duringer, P., Helm, C., Bano, M., Long, V.T., Thuy, N.T.K., Antoine, P.-O., Mai, B.T., Mai Huong, N.T., Dodo, Y., Chabaux, F., Rihs, S. (2008). The late Pleistocene Duoi U'Oi cave in northern Vietnam: Palaeontology, sedimentology, taphonomy and palaeoenvironments. *Quaternary Science Reviews*, *27*(15–16), 1627–1654. DOI:10.1016/j.quascirev.2008.04.017

Bae, C.J., Douka, K., Petraglia, M.D. (2017). On the origin of modern humans: Asian perspectives. *Science*, *358*(6368), eaai9067. DOI: 10.1126/science.aai9067

Barker, G., Barton, H., Bird, M., Daly, P., Datan, I., Dykes, A., Farr, L., Gilbertson, D., Harrisson, B., Hunt, C., Higham, T., Kealhofer, L., Krigbaum, J., Lewis, L., McLaren, S. J., Paz, V., Pike, A., Piper, P., Pyatt, B., Rabett, R., Reynolds, T., Rose, J., Rushworth, G., Stephens, M., Stringer, C., Thompson, J., Turney, C. (2007). The 'human revolution'in lowland tropical Southeast Asia: The antiquity and behavior of anatomically modern humans at Niah Cave (Sarawak, Borneo). *Journal of Human Evolution*, *52*(3), 243–261. DOI:10.1016/j.jhevol.2006.08.011

Barker, G., Reynolds, T., Gilbertson, D. (2005). The human use of caves in Peninsular and Island Southeast Asia: Research themes. *Asian Perspectives*, *44*(1), 1–15. DOI:10.1353/asi.2005.0003

Bich, T.Q., Lap, D.T., Dat, L.T., Cuong, N.M. (2009). Biological diversity at Cuc Phuong National Park. *Vietnam Archaeology, 4,* 14–23.

Bird, M.I., Boobyer, E.M., Bryant, C., Lewis, H.A., Paz, V., Stephens, W.E. (2007). A long record of environmental change from bat guano deposits in Makangit Cave, Palawan, Philippines. *Earth and Environmental Science Transactions of the Royal Society of Edinburgh*, *98*(1), 59–69. DOI:10.1017/S1755691007000059

Brumm, A., Moore, M.W. (2012). Biface distributions and the Movius Line: A Southeast Asian perspective. *Australian Archaeology*, *74*(1), 34–46. DOI:10.1080/03122417.2012.11681933

Cai, Y., An, Z., Cheng, H., Edwards, R.L., Kelly, M.J., Liu, W., Wang, X., Shen, C.-C. (2006). High-resolution absolute-dated Indian monsoon record between 53 and 36 ka from Xiaobailong Cave, southwestern China. *Geology*, *34*(8), 621–624. DOI:10.1130/G22567.1

Cai, Y., Fung, I.Y., Edwards, R.L., An, Z., Cheng, H., Lee, J.-E., Tan, L., Shen, C.-C., Wang, X., Day, J.A., Zhou, W., Kelly, M.J., Chiang, J.C.H. (2015). Variability of stalagmite-inferred Indian monsoon precipitation over the past 252,000 y. *Proceedings of the National Academy of Sciences*, *112*(10), 2954–2959. DOI: 10.1073/pnas.1424035112

Chabangborn, A., Yamoah, K.K., Phantuwongraj, S., Choowong, M. (2018). Climate in Sundaland and Asian monsoon variability during the last deglaciation. *Quaternary International, 479,* 141–147. DOI:10.1016/j.quaint.2017.04.017

Clarkson, C., Jacobs, Z., Marwick, B., Fullagar, R., Wallis, L., Smith, M., Roberts, R.G., Hayes, E., Lowe, K., Carah, X., Florin, S.A., McNeil, J., Cox, D., Arnold, L.J., Hua, Q., Huntley, J., Brand, H.E.A., Manne, T., Fairbairn, A., Shulmeister, J., Lyle, L., Salinas, M., Page, M., Connell, K., Park, G., Norman, K., Murphy, T., Pardoe, C. (2017). Human occupation of northern Australia by 65,000 years ago. *Nature*, *547*(7663), 306–310. DOI:10.1038/nature22968

Corny, J., Galland, M., Arzarello, M., Bacon, A.-M., Demeter, F., Grimaud-Hervé, D., Higham, C., Matsumura, H., Nguyen, L.C., Nguyen, T.K.T., Nguyen, V., Oxenham, M., Sayavongkhamdy, T., Sémah, F., Shackelford, L., Détroit, F. (2017). Dental phenotypic shape variation supports a multiple dispersal model for anatomically modern humans in Southeast Asia. *Journal of Human Evolution*, *112*, 41–56. DOI:10.1016/j.jhevol.2017.08.017

Davies, B.E. (1974). Loss-on-ignition as an estimate of soil organic matter 1. *Soil Science Society of America Journal*, *38*(1), 150–151. DOI:10.2136/sssaj1974.03615995003800010046x

Demeter, F., Manni, F., Coppens, Y. (2003). Late Upper Pleistocene human peopling of the Far East: Multivariate analysis and geographic patterns of variation. *Comptes Rendus Palevol*, *2*(8), 625–638. DOI:10.1016/j.crpv.2003.09.010

Demeter, F., Shackelford, L., Westaway, K., Barnes, L., Duringer, P., Ponche, J.-L., Dumoncel, J., Sénégas, F., Sayavongkhamdy, T., Zhao, J.-X., Sichanthongtip, P., Pätole-Edoumba, E., Dunn,

T., Zachwieja, A., Coppens, Y., Willerslev, E., Bacon, A.-M. (2017). Early modern humans from Tam Pa Ling, Laos: Fossil review and perspectives. *Current Anthropology*, *58*(S17), S000–S000. DOI:10.1086/694192

Dennell, R., Porr, M. (2014). Smoke and mirrors: The fossil record for *Homo sapiens* between Arabia and Australia. In R. Dennell, M. Porr (Eds.). *Southern Asia, Australia and the Search for Human Origins* (pp. 33–50). Cambridge, UK: Cambridge University Press. DOI:10.1017/CBO9781139084741.004

Derevianko, A.P., Kandyba, A.V., Tsybanbkov, A.A. (2012). The earliest stages of human colonization in Southeast Asia: archaeological and paleoecological data. In E.N. Chernykh (ed.). *Мегаструктуре Евразийского мира: Основные этапы формирования: Материалы Всероссийской научной конференции [Megastructure of the Eurasian world: The developmental milestones: Proceedings of the Russian National Scientific Conference]* (pp. 27–30). Moscow, RU: Taus.

Derevianko, A.P., Su, N.K., Tikhonov, A.N., Tsybanbkov, A.A., Kandyba, A.V., Doi, N.G., Cheka, A.M. (2014). Paleoecology of Con Moong Cave (based on faunal data). *Проблемы археологии, этнографии, антропологии Сибири и сопредельных территорий*, *20 [Problems of Archaeology, Ethnography, Anthropology of Siberia and Neighboring Territories, 20]*, 36–38.

Derevianko, A.P., Hai, N.G., Su, N.K., Tikhonov, A.N., Cheka, A.M., Doi, N.G., Toan, P.T., Kandyba, A.V., Tsybanbkov, A.A. (2012). Preliminary results of research studies carried out by the 2010-2011 Russian-Vietnamese expedition in Northern Vietnam. *Проблемы археологии, этнографии, антропологии Сибири и сопредельных территорий*, *18 [Problems of Archaeology, Ethnography, Anthropology of Siberia and Neighboring Territories, 18]*, 63–67.

Dykes, A. (2007). Mass movements in cave sediments: Investigation of a∼ 40,000-year-old guano mudflow inside the entrance of the Great Cave of Niah, Sarawak, Borneo. *Landslides*, *4*(3), 279–290. DOI: 10.1007/s10346-006-0077-5

Frost, R.L., Xi, Y., Palmer, S.J., Pogson, R.E. (2011). Vibrational spectroscopic analysis of taranakite (K, NH 4) Al 3 (PO 4) 3 (OH)· 9 (H 2 O) from the Jenolan Caves, Australia. *Spectrochimica Acta Part A: Molecular and Biomolecular Spectroscopy*, *83*(1), 106–111. DOI:10.1016/j.saa.2011.07.088

Galbraith, R.F., Roberts, R.G., Laslett, G.M., Yoshida, H., Olley, J.M. (1999). Optical dating of single and multiple grains of quartz from Jinmium rock shelter, northern Australia: Part I, experimental design and statistical models. *Archaeometry*, *41*(2), 339–364. DOI:10.1111/j.14754754.1999.tb00987.x

Gilbertson, D., Bird, M., Hunt, C., McLaren, S.J., Banda, R.M., Pyatt, B., Rose, J., Stephens, M. (2005). Past human activity and geomorphological change in a guano-rich tropical cave mouth: Initial interpretations of the Late Quaternary succession in the Great Cave of Niah, Sarawak. *Asian Perspectives*, *44*(1), 16–41. DOI:10.1353/asi.2005.0007

Gillieson, D. (1986). Cave sedimentation in the New Guinea highlands. *Earth Surface Processes and Landforms*, *11*(5), 533–543. DOI:10.1002/esp.3290110508

Gillieson, D. (2005). Karst in southeast Asia. In A. Gupta (Ed.). *The physical geography of Southeast Asia* (pp. 157–176). Oxford, UK: Oxford University Press.

Goldberg, P., Bar-Yosef, O. (2002). Site formation processes in Kebara and Hayonim caves and their significance in Levantine prehistoric caves. In T. Akazawa, K. Aoki, O. Bar-Yosef (Eds.). *Neandertals and modern humans in western Asia* (pp. 107–125). Boston, MA: Springer. DOI:10.1007/0-306-47153-1_8

Goldberg, P., Sherwood, S.C. (2006). Deciphering human prehistory through the geoarcheological study of cave sediments. *Evolutionary Anthropology: Issues, News, and Reviews*, *15*(1), 20–36. DOI:10.1002/evan.20094

Gupta, A. (2005). Landforms of Southeast Asia. In A. Gupta (Ed.). *The physical geography of Southeast Asia* (pp. 38–64). Oxford, UK: Oxford University Press.

Hall, R. (2009). Southeast Asia's changing palaeogeography. *Blumea - Biodiversity, Evolution and Biogeography of Plants*, *54*(1–2), 148–161. DOI:10.3767/000651909X475941

Hawkins, S., O'Connor, S., Kealy, S. (2016). Late Quaternary hominin–bat (Chiroptera) interactions in the Asia-Pacific. *Archaeology in Oceania*, *51*(1), 7–17. DOI:10.1002/arco.5084

Heiberg, L., Koch, C.B., Kjaergaard, C., Jensen, H.S., Hansen, H.C.B. (2012). Vivianite precipitation and phosphate sorption following iron reduction in anoxic soils. *Journal of Environmental Quality*, *41*(3), 938–949. DOI:10.2134/jeq2011.0067

Heiri, O., Lotter, A.F., Lemcke, G. (2001). Loss on ignition as a method for estimating organic and carbonate content in sediments: Reproducibility and comparability of results. *Journal of Paleolimnology, 25*(1), 101–110. DOI:10.1023/A:1008119611481

Hien, P.D., Bac, V.T., Tham, H.C., Nhan, D.D., Vinh, L.D. (2002). Influence of meteorological conditions on PM2. 5 and PM2. 5−10 concentrations during the monsoon season in Hanoi, Vietnam. *Atmospheric Environment*, *36*(21), 3473–3484. DOI:10.1016/S1352-2310(02)00295-9

Higham, C. (2014). *Early mainland Southeast Asia: From first humans to Angkor*. Bangkok, TH: River Books.

Hunt, C.O., Barker, G.W. (2014). Missing links, cultural modernity and the dead: Anatomically modern humans in the Great Cave of Niah (Sarawak, Borneo). In R. Dennell, M. Porr (Eds.). *Southern Asia, Australia, and the search for human origins* (pp. 90–107). Cambridge, UK: Cambridge University Press.

Hunt, C.O., Gilbertson, D.D., Hill, E.A., Simpson, D. (2015). Sedimentation, re-sedimentation and chronologies in archaeologically-important caves: Problems and prospects. *Journal of Archaeological Science*, *56*, 109–116. DOI:10.1016/j.jas.2015.02.030

Hunt, C.O., Gilbertson, D.D., Rushworth, G. (2012). A 50,000-year record of late Pleistocene tropical vegetation and human impact in lowland Borneo. *Quaternary Science Reviews, 37,* 61–80. DOI:10.1016/j.quascirev.2012.01.014

Mai Huong, N.T., Van Hai, P. (2009). Analytic results of spores and pollen from Con Moong Cave. *Vietnam Archaeology, 4,* 24–31.

Hutchison, C.S. (2005). The geological framework. In A. Gupta (Ed.). *The physical geography of Southeast Asia* (pp. 3–23). Oxford, UK: Oxford University Press

Jacobs, Z., Roberts, R.G. (2007). Advances in optically stimulated luminescence dating of individual grains of quartz from archeological deposits. *Evolutionary Anthropology: Issues, News, and Reviews*, *16*(6), 210–223. DOI:10.1002/evan.20150

Ji, X., Kuman, K., Clarke, R., Forestier, H., Li, Y., Ma, J., Qiu, K., Li, H., Wu, Y. (2016). The oldest Hoabinhian technocomplex in Asia (43.5 ka) at Xiaodong Rockshelter, Yunnan Province, southwest China. *Quaternary International, 400,* 166–174. DOI:10.1016/j.quaint.2015.09.080

Karkanas, P. (2010). Preservation of anthropogenic materials under different geochemical processes: A mineralogical approach. *Quaternary International*, *214*, 63–69. DOI:10.1016/j.quaint.2009.10.017

Karkanas, P. (2017). Guano. In C. Nicosia, G. Stoops (Eds.). *Encyclopedia of archaeological soil and sediment micromorphology* (pp. 83–89). Hoboken, NJ: John Wiley & Sons Ltd. DOI:10.1002/9781118941065.ch8

Karkanas, P., Bar-Yosef, O., Goldberg, P., Weiner, S. (2000). Diagenesis in prehistoric caves: The use of minerals that form in situ to assess the completeness of the archaeological record. *Journal of Archaeological Science, 27*(10)*,* 915–929. DOI:10.1006/jasc.1999.0506

Karkanas, P., Goldberg, P. (2010). Phosphatic features. In G. Stoops, V. Marcelino, F. Mees (Eds.). *Interpretation of micromorphological features of soils and regoliths* (pp. 521–541). Amsterdam, NL: Elsevier. DOI:10.1016/B978-0-444-53156-8.00023-4

Khang, P. (1985). The development of karst landscapes in Vietnam. *Acta Geologica Polonica, 35*(3–4), 305–324.

Kottek, M., Grieser, J., Beck, C., Rudolf, B., Rubel, F. (2006). World map of the Koppen-Geiger climate classification updated. *Meteorologische Zeitschrift, 15*(3), 259–263. DOI:10.1127/0941-2948/2006/0130

Kourampas, N., Simpson, I.A., Perera, N., Deraniyagala, S.U., Wijeyapala, W. (2009). Rockshelter sedimentation in a dynamic tropical landscape: Late Pleistocene–early Holocene archaeological deposits in Kitulgala Beli-lena, southwestern Sri Lanka. *Geoarchaeology*, *24*(6), 677–714. DOI:10.1002/gea.20287

Lam, D.D., Su, N.K. (2014). Stratigraphic sequence of the Con Moong Cave, Thanh Hoa Province, and its implications for the upper Quaternary Stratigraphy of Northern Vietnam. In R. Rocha, J. Pais, J. Kullberg, S. Finney (Eds.). *STRATI 2013: First International Congress on Stratigraphy: At the cutting edge of stratigraphy* (pp. 957–964). Cham, CH: Springer. DOI:10.1007/978-3-319-04364-7_180

Lewis, H. (2007). Preliminary soil micromorphology studies of landscape and occupation history at Tabon Cave, Palawan, Philippines. *Geoarchaeology, 22*(7), 685–708. DOI: 10.1002/gea.20182

Lipson, M., Cheronet, O., Mallick, S., Rohland, N., Oxenham, M., Pietrusewsky, M., Pryce, T.O., Willis, A., Matsumura, H., Buckley, H. (2018). Ancient genomes document multiple waves of migration in Southeast Asian prehistory. *Science*, *361*(6397), 92–95. DOI:10.1126/science.aat3188

Lisiecki, L.E., Raymo, M.E. (2005). A Pliocene-Pleistocene stack of 57 globally distributed benthic $\delta^{18}O$ records. *Paleoceanography*, *20*(1), PA1003. DOI:10.1029/2004PA001071

Liu, W., Martinón-Torres, M., Cai, Y.-J., Xing, S., Tong, H.-W., Pei, S.-W., Sier, M.J., Wu, X.-H., Edwards, R.L., Cheng, H., Li Y.-Y., Yang, X.-X., De Castro, J.M.B., Wu, X.-J. (2015). The earliest unequivocally modern humans in southern China. *Nature*, *526*(7575), 696–699. DOI:10.1038/nature15696

Macphail, R.I., Cruise, J. (2001). The soil micromorphologist as team player. In P. Goldberg, V.T. Holliday, C.R. Ferring (Eds.). *Earth sciences and archaeology* (pp. 241–267). New York, NY: Springer Science + Business Media. DOI:10.1007/978-1-4615-1183-0_9

Mallol, C., Goldberg, P. (2017). Cave and rock shelter sediments. In C. Nicosia, G. Stoops (Eds.). *Archaeological soil and sediment micromorphology* (pp. 359–381). Chichester, UK: John Wiley & Sons Ltd. DOI: 10.1002/9781118941065.ch34

Mallol, C., Mentzer, S.M. (2017). Contacts under the lens: Perspectives on the role of microstratigraphy in archaeological research. *Archaeological and Anthropological Sciences, 9*(8)*,* 1645–1669. DOI:10.1007/s12520-015-0288-6

Mallol, C., Mentzer, S.M., Wrinn, P.J. (2009). A micromorphological and mineralogical study of site formation processes at the late Pleistocene site of Obi-Rakhmat, Uzbekistan. *Geoarchaeology, 24*(5), 548–575. DOI:10.1002/gea.20280

Marwick, B. (2009). Biogeography of Middle Pleistocene hominins in mainland Southeast Asia: A review of current evidence. *Quaternary International*, *202*(1–2)*,* 51–58. DOI:10.1016/j.quaint.2008.01.012

Marwick, B. (2018). The Hoabinhian of Southeast Asia and its Relationship to Regional Pleistocene Lithic Technologies. In E. Robinson, F. Sellet (Eds.). *Studies in human ecology and adaptation 9: Lithic technological organization and paleoenvironmental change: Global and diachronic perspectives* (pp. 63–78). Cham, CH: Springer. DOI:10.1007/978-3-319-64407-3_4

Marwick, B., Gagan, M.K. (2011). Late Pleistocene monsoon variability in northwest Thailand: an oxygen isotope sequence from the bivalve *Margaritanopsis laosensis* excavated in Mae Hong Son province. *Quaternary Science Reviews*, *30*(21–22)*,* 3088–3098. DOI:10.1016/j.quascirev.2011.07.007

McColl, H., Racimo, F., Vinner, L., Demeter, F., Gakuhari, T., Moreno-Mayar, J.V., van Driem, G., Gram Wilken, U., Seguin-Orlando, A., de la Fuente Castro, C., Wasef, S., Shoocongdej, R., Souksavatdy, V., Sayavongkhamdy, T., Saidin, M.M., Allentoft, M.E., Sato, T., Malaspinas, A.-S., Aghakhanian, F.A., Korneliussen, T., Prohaska, A., Margaryan, A., de Barros Damgaard, P., Kaewsutthi, S., Lertrit, P., Nguyen, T.M.H., Hung, H.-C., Minh Tran, T., Nghia Truong, H., Nguyen, G.H., Shahidan, S., Wiradnyana, K., Matsumae, H., Shigehara, N., Yoneda, M., Ishida, H., Masuyama, T., Yamada, Y., Tajima, A., Shibata, H., Toyoda, A., Hanihara, T., Nakagome, S., Deviese, T., Bacon, A.-M., Duringer, P., Ponche, J.L., Shackelford, L., Patole-Edoumba, E., Nguyen, A.T., Bellina-Pryce, B., Galipaud, J.-C., Kinaston, R., Buckley, H., Pottier, C., Rasmussen, S., Higham, T., Foley, R.A., Lahr, M.M., Orlando, L., Sikora, M., Phipps, M.E., Oota, H., Higham, C., Lambert, D.M., Willerslev, E. (2018). The prehistoric peopling of Southeast Asia. *Science*, *361*(6397)*,* 88–92. DOI:10.1126/science.aat3628

Mees, F., Stoops, G. (2010). Sulphidic and sulphuric materials. In G. Stoops, V. Marcelino, F. Mees (Eds.). *Interpretation of micromorphological features of soils and regoliths* (pp. 543–568). Amsterdam, NL: Elsevier. DOI:10.1016/B978-0-444-63522-8.00013-9

Mentzer, S.M. (2014). Microarchaeological approaches to the identification and interpretation of combustion features in prehistoric archaeological sites. *Journal of Archaeological Method and Theory, 21*(3), 616–668. DOI:10.1007/s10816-012-9163-2

Mentzer, S.M., Quade, J. (2013). Compositional and isotopic analytical methods in archaeological micromorphology. *Geoarchaeology, 28*(1)*,* 87–97. DOI:10.1002/gea.21425

Mijares, A.S., Détroit, F., Piper, P., Grün, R., Bellwood, P., Aubert, M., Champion, G., Cuevas, N., De Leon, A., Dizon, E. (2010). New evidence for a 67,000-year-old human presence at Callao Cave, Luzon, Philippines. *Journal of Human Evolution, 59*(1)*,* 123–132. DOI:10.1016/j.jhevol.2010.04.008

Moormann, F.R. (1961). *The soils of The Republic of Vietnam: A reconnaissance survey with general soil map and description of the major soils in relation with their agricultural use and potential*. Saigon, RVN: National Geographic Service.

Morley, M.W. (2017). The geoarchaeology of hominin dispersals to and from tropical Southeast Asia: A review and prognosis. *Journal of Archaeological Science, 77,* 78–93. DOI:10.1016/j.jas.2016.07.009

Morley, M.W., Goldberg, P. (2017). Geoarchaeological research in the humid tropics: A global perspective. *Journal of Archaeological Science, 77,* 1–9. DOI:10.1016/j.jas.2016.11.002

Morley, M.W., Goldberg, P., Sutikna, T., Tocheri, M.W., Prinsloo, L.C., Saptomo, E.W., Wasisto, S., Roberts, R.G. (2017). Initial micromorphological results from Liang Bua, Flores (Indonesia): Site formation processes and hominin activities at the type locality of *Homo floresiensis*. *Journal of Archaeological Science, 77,* 125–142. DOI:10.1016/j.jas.2016.06.004

Moser, J. (2012). The Hoabinhian definition in the past and today: A short historical review of defining the Hoabinhian. In M. L. Tjoa-Bonatz, A. Reinecke, D. Bonatz (Eds.). *Crossing Borders: Selected papers from the 13th International Conference of the European Association of Southeast Asian Archaeologists, Volume 1* (pp. 3–25). Singapore, SG: National University of Singapore Press

Mücher, H., van Steijn, H., Kwaad, F. (2010). Colluvial and mass wasting deposits. In G. Stoops, V. Marcelino, F. Mees (Eds.). *Interpretation of micromorphological features of soils and regoliths* (pp. 37–48). Amsterdam, NL: Elsevier. DOI:10.1016/B978-0-444-63522-8.00002-4

Murray, A.S., Wintle, A.G. (2000). Luminescence dating of quartz using an improved single-aliquot regenerative-dose protocol. *Radiation Measurements, 32*(1), 57–73. DOI:10.1016/S1350-4487(99)00253-X

Nam, T.N. (1995). The geology of Vietnam: A brief summary and problems. *静岡大学地球科学研究報告,22[Geoscience Reports of Shizuoka University,22],* 1–9. DOI:10.14945/00000334

Nguyen-Le, D., Matsumoto, J., Ngo-Duc, T. (2014). Climatological onset date of summer monsoon in Vietnam. *International Journal of Climatology, 34*(11), 3237–3250. DOI:10.1002/joc.3908

O'Geen, A.T. (2012). Soil Water Dynamics. *Nature Education Knowledge*, *3,* 12.

O'Connor, S., Barham, A., Aplin, K., Maloney, T. (2017). Cave stratigraphies and cave breccias: Implications for sediment accumulation and removal models and interpreting the record of human occupation. *Journal of Archaeological Science, 77,* 143–159. DOI:10.1016/j.jas.2016.05.002

O'Connor, S., Bulbeck, D. (2014). *Homo sapiens* societies in Indonesia and South-Eastern Asia. In V. Cummings, P. Jordan, M. Zvelebil (Eds.). *The Oxford handbook of the archaeology and anthropology of hunter-gatherers* (pp. 346–367). Oxford, UK: Oxford University Press. DOI: 10.1093/oxfordhb/9780199551224.013.018

Olson, K.R., Morton, L.W. (2017). Why were the soil tunnels of Cu Chi and Iron Triangle in Vietnam so resilient? *Open Journal of Soil Science, 7*(02), 34–51. DOI:10.4236/ojss.2017.72003

Onac, B.P., Vereş, D.Ş. (2003). Sequence of secondary phosphates deposition in a karst environment: evidence from Măgurici Cave (Romania). *European Journal of Mineralogy, 15*(4), 741–745. DOI:10.1127/0935-1221/2003/0015-0741

Pääbo, S. (2015). The diverse origins of the human gene pool. *Nature Reviews Genetics*, *16*(6), 313–314. DOI:10.1038/nrg3954

Piper, P.J., Rabett, R.J. (2014). Late Pleistocene subsistence strategies in island Southeast Asia and their implications for understanding the development of modern human behaviour. In R. Dennell, M. Porr (Eds.). *Southern Asia, Australia and the search for human origins* (pp. 118–134). Cambridge, UK: Cambridge University Press.

Quang, P.V. (2009). Geological structure and karst characteristics of Cúc-phương area. *Vietnam Archaeology, 4,* 6–13.

R Core Team (2013). *R: A language and environment for statistical computing*. Vienna, AT: R Foundation for Statistical Computing. URL http://www.R-project.org/

Rabett, R., Appleby, J., Blyth, A., Farr, L., Gallou, A., Griffiths, T., Hawkes, J., Marcus, D., Marlow, L., Morley, M., Tâń, N.C., Son, N.V., Penkman, K., Reynolds, T., Stimpson, C., Szabó, K.(2011). Inland shell midden site-formation: Investigation into a late Pleistocene to early Holocene midden from Tràng An, northern Vietnam. *Quaternary International, 239*(1–2)*,* 153–169. DOI:10.1016/j.quaint.2010.01.025

Rabett, R., Ludgate, N., Stimpson, C., Hill, E., Hunt, C., Ceron, J., Farr, L., Morley, M., Reynolds, T., Zukswert, H., Simpson, D., Nyirii, B., Verhoeven, M., Appleby, J., Meneely, J., Phan, L., Dong, N.N., Lloyd-Smith, L., Hawkes, J., Blyth, A., Cao Tâń, N. (2017). Tropical limestone forest resilience and late Pleistocene foraging during MIS-2 in the Trang An massif, Vietnam. *Quaternary International, 448,* 62–81. DOI:10.1016/j.quaint.2016.06.010

Rabett, R.J. (2018). The success of failed *Homo sapiens* dispersals out of Africa and into Asia. *Nature Ecology & Evolution, 2*(2)*,* 212–219. DOI:10.1038/s41559-017-0436-8

Reyes-Centeno, H. (2016). Out of Africa and into Asia: Fossil and genetic evidence on modern human origins and dispersals. *Quaternary International, 416,* 249–262. DOI:10.1016/j.quaint.2015.11.063

Roberts, P., Perera, N., Wedage, O., Deraniyagala, S., Perera, J., Eregama, S., Gledhill, A., Petraglia, M.D., Lee-Thorp, J.A. (2015a). Direct evidence for human reliance on rainforest resources in late Pleistocene Sri Lanka. *Science*, *347*(6227)*,* 1246–1249. DOI:10.1126/science.aaa1230

Roberts, R.G., Jacobs, Z., Li, B., Jankowski, N.R., Cunningham, A.C., Rosenfeld, A.B. (2015b). Optical dating in archaeology: thirty years in retrospect and grand challenges for the future. *Journal of Archaeological Science, 56,* 41–60. DOI:10.1016/j.jas.2015.02.028

Roden, E., Edmonds, J. (1997). Phosphate mobilization in iron-rich anaerobic sediments: Microbial Fe (III) oxide reduction versus iron-sulfide formation. *Archiv fur Hydrobiologie, 139*(3)*,* 347–378.

Rohling, E.J., Liu, Q., Roberts, A., Stanford, J., Rasmussen, S.O., Langen, P.L., Siddall, M. (2009). Controls on the East Asian monsoon during the last glacial cycle, based on comparison between Hulu Cave and polar ice-core records. *Quaternary Science Reviews, 28*(27–28)*,* 3291–3302. DOI:10.1016/j.quascirev.2009.09.007

Rothe, M., Kleeberg, A., Hupfer, M. (2016). The occurrence, identification and environmental relevance of vivianite in waterlogged soils and aquatic sediments. *Earth-Science Reviews*, *158,* 51–64. DOI:10.1016/j.earscirev.2016.04.008

Rugendyke, B., Son, N.T. (2005). Conservation costs: Nature-based tourism as development at Cuc Phuong National Park, Vietnam. *Asia Pacific Viewpoint*, *46*(2)*,* 185–200. DOI:10.1111/j.1467-8373.2005.00265.x

Sehgal, J. (1989). *Classification & correlation of the Vietnamese soils: A technical report.* Strengthening of the National Institute for Agricultural Planning & Projections (NIAPP) Viet-Nam, project: VIE86/024. Hanoi, VT: United Nations Development Programme Food & Agricultural Organisation.

Shackelford, L., Demeter, F., Westaway, K., Duringer, P., Ponche, J.-L., Sayavongkhamdy, T., Zhao, J.-X., Barnes, L., Boyon, M., Sichanthongtip, P., Sénégas, P., Patole-Edoumba, E., Coppens, Y., Dumoncel, J., Bacon, A.-M., (2018). Additional evidence for early modern human morphological diversity in Southeast Asia at Tam Pa Ling, Laos. *Quaternary International, 466,* 93–106. DOI:10.1016/j.quaint.2016.12.002

Shahack-Gross, R. (2017). Archaeological formation theory and geoarchaeology: State-of-the-art in 2016. *Journal of Archaeological Science, 79,* 36–43. DOI: 10.1016/j.jas.2017.01.004

Shahack-Gross, R., Berna, F., Karkanas, P., Weiner, S. (2004). Bat guano and preservation of archaeological remains in cave sites. *Journal of Archaeological Science*, *31*(9), 1259–1272. DOI:10.1016/j.jas.2004.02.004

Sikora, M. (2017). A genomic view of the Pleistocene Population History of Asia. *Current Anthropology, 58*(S17)*,* S397–S405. DOI:10.1086/694422

Stephens, M., Rose, J., Gilbertson, D. (2017). Post-depositional alteration of humid tropical cave sediments: Micromorphological research in the great cave of Niah, Sarawak, Borneo. *Journal of Archaeological Science, 77,* 109–124. DOI:10.1016/j.jas.2016.01.015

Sterling, E., Hurley, M., Minh, L. (2006). *A natural history of Vietnam*. Yale, CT: Yale University Press.

Stiner, M.C., Kuhn, S.L., Surovell, T.A., Goldberg, P., Meignen, L., Weiner, S., Bar-Yosef, O. (2001). Bone preservation in Hayonim Cave (Israel): A macroscopic and mineralogical study. *Journal of Archaeological Science, 28*(6)*,* 643–659. DOI:10.1006/jasc.2000.0634

Stoops, G. (2003). *Guidelines for analysis and description of soil and regolith thin sections*. Madison, WI: Soil Science Society of America Inc. DOI:10.2136/2003

Su, N.K. (2009). Con Moong Cave: Data from exploration and new perception. *Vietnam archaeology, 4,* 40–52.

Sutikna, T., Tocheri, M.W., Morwood, M.J., Saptomo, E.W., Awe, R.D., Wasisto, S., Westaway, K.E., Aubert, M., Li, B., Zhao, J.-X., Storey, M., Alloway, B.V., Morley, M.W., Meijer, H.J.M., van den Bergh, G.D., Grün, R., Dossetto, A., Brumm, A., Jungers, W.L., Roberts, R.G. (2016). Revised stratigraphy and chronology for *Homo floresiensis* at Liang Bua in Indonesia. *Nature, 532*(7599)*,* 366–369. DOI:10.1038/nature17179

Tatur, A., Keck, A. (1990). Phosphates in ornithogenic soils of the maritime Antarctic. *Proceedings of the NIPR Symposium on Polar Biology, 3,* 133–150.

Thong, P.H. (1980). Con Moong Cave: a noteworthy archaeological discovery in Vietnam. *Asian Perspectives*, *23*(1), 17–21.

United Stated Department of Agriculture (1997). *Soil Moisture Regimes Map (1:5,000,000).* Retrieved from https://www.nrcs.usda.gov/wps/portal/nrcs/detail/soils/use/?cid=nrcs142p2_054017

Van Tan, H. (1997). The Hoabinhian and before. *Bulletin of the Indo-Pacific Prehistory Association, 16,* 35–41. DOI:10.7152/bippa.v16i0.11643

Wang, B. (2002). Rainy season of the Asian–Pacific summer monsoon. *Journal of Climate, 15*(4), 386–398. DOI:10.1175/1520-0442(2002)015%3C0386:RSOTAP%3E2.0.CO;2

Wang, P., Clemens, S., Beaufort, L., Braconnot, P., Ganssen, G., Jian, Z., Kershaw, P., Sarnthein, M. (2005). Evolution and variability of the Asian monsoon system: State of the art and outstanding issues. *Quaternary Science Reviews, 24*(5–6), 595–629. DOI:10.1016/j.quascirev.2004.10.002

Wedage, O., Amano, N., Langley, M.C., Douka, K., Blinkhorn, J., Crowther, A., Deraniyagala, S., Kourampas, N., Simpson, I., Perera, N., Picin, A., Boivin, N., Petraglia, M., Roberts, P. (2019). Specialized rainforest hunting by *Homo sapiens* ~ 45,000 years ago. *Nature Communications, 10*(1), 739. DOI:10.1038/s41467-019-08623-1

Weiner, S., Goldberg, P., Bar-Yosef, O. (1993). Bone preservation in Kebara Cave, Israel using on-site Fourier transform infrared spectrometry. *Journal of Archaeological Science, 20*(6), 613–627. DOI:10.1006/jasc.1993.1037

Weiner, S., Goldberg, P., Bar-Yosef, O. (2002). Three-dimensional distribution of minerals in the sediments of Hayonim Cave, Israel: Diagenetic processes and archaeological implications. *Journal of Archaeological Science, 29*(11), 1289–1308. DOI:10.1006/jasc.2001.0790

Weiner, S., Schiegl, S., Goldberg, P., Bar-Yosef, O. (1995). Mineral assemblages in Kebara and Hayonim caves, Israel: Excavation strategies, bone preservation, and wood ash remnants. *Israel Journal of Chemistry, 35*(2), 143–154. DOI:10.1002/ijch.199500022

Westaway, K.E., Louys, J., Awe, R.D., Morwood, M.J., Price, G.J., Zhao, J.X., Aubert, M., Joannes-Boyau, R., Smith, T., Skinner, M.M., Compton, T., Bailey, R.M., van den Bergh, G.D., de Vos, J., Pike, W.G., Stringer, C., Saptomo, E.W., Rizal, Y., Zaim, J., Santoso, W.D., Trihascaryo, A., Kinsley, L., Sulistyanto, B. (2017). An early modern human presence in Sumatra 73,000–63,000 years ago. *Nature, 548*(7667), 322–325. DOI:10.1038/nature23452

Wurster, C.M., Bird, M.I. (2016). Barriers and bridges: Early human dispersals in equatorial SE Asia. *Geological Society, London, Special Publications, 411*(1), 235–250. DOI:10.1144/SP411.2

Wurster, C.M., Bird, M.I., Bull, I.D., Creed, F., Bryant, C., Dungait, J.A., Paz, V. (2010). Forest contraction in north equatorial Southeast Asia during the Last Glacial Period. *Proceedings of the National Academy of Sciences, 107*(35)*,* 15508–15511. DOI:10.1073/pnas.1005507107

Wurster, C.M., Munksgaard, N., Zwart, C., Bird, M. (2015). The biogeochemistry of insectivorous cave guano: A case study from insular Southeast Asia. *Biogeochemistry, 124*(1–3)*,* 163–175. DOI:10.1007/s10533-015-0089-0

Zhang, T.-T., Li, T.-Y., Cheng, H., Edwards, R.L., Shen, C.-C., Spötl, C., Li, H.-C., Han, L.-Y., Li, J.-Y., Huang, C.-X., Zhao, X. (2017). Stalagmite-inferred centennial variability of the Asian summer monsoon in southwest China between 58 and 79 ka BP. *Quaternary Science Reviews, 160,* 1–12. DOI:10.1016/j.quascirev.2017.02.003

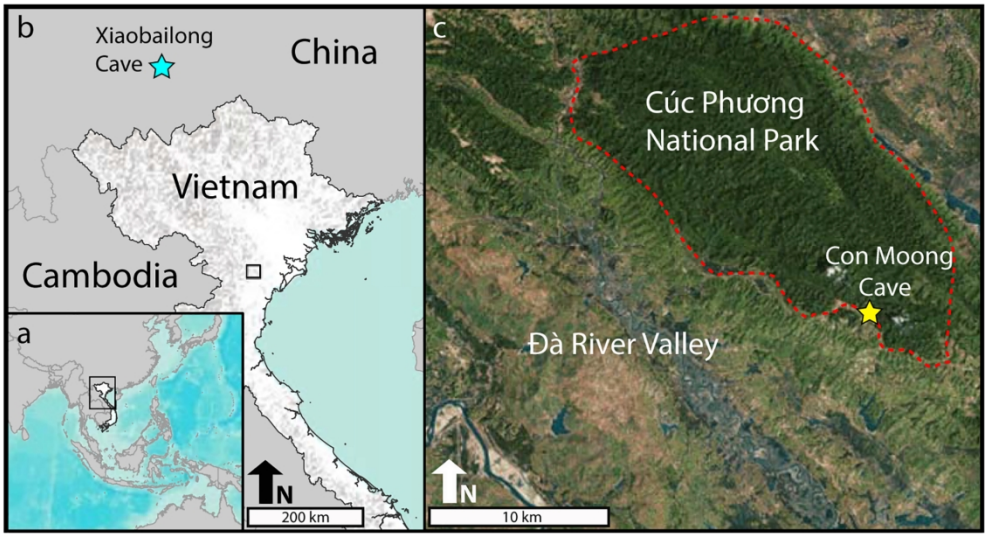


Fig. 1: (a) Inset map showing Vietnam in Southeast Asia. Extent of (b) marked by black rectangle; (b) Map showing the topography of North Vietnam with the position of Xiaobailong cave, southern China (Cai et al. 2015) marked by blue star. Extent of (c) demarcated by black rectangle; (c) Map showing the position of Con Moong Cave within Cúc Phương National Park, a nature reserve protecting densely forested limestone uplands to the south of the Hanoi basin.

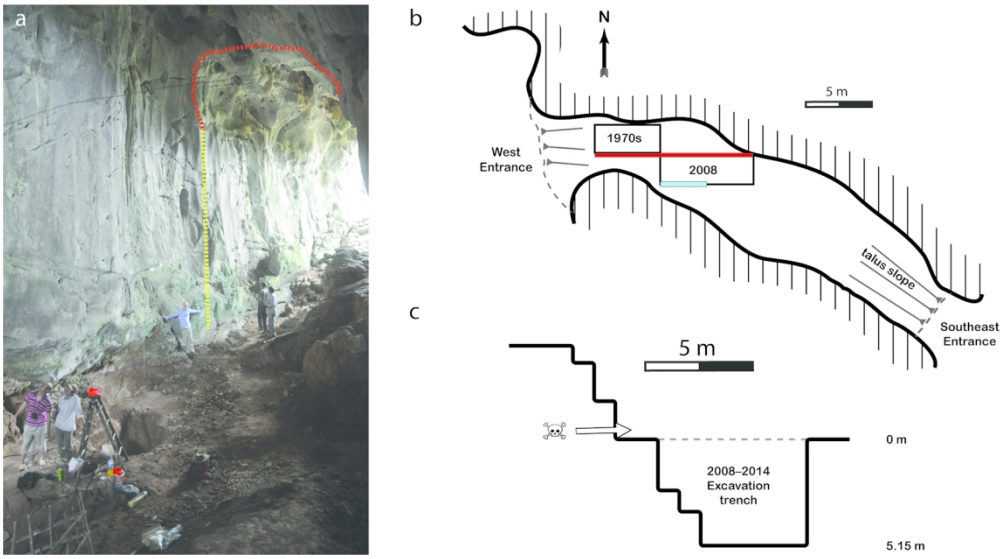


Fig. 2: (a) Photograph of the west-facing entrance of Con Moong Cave, highlighting features related to passage development. Red dashed line marks remains of phreatic section, yellow dashed line marks steep-sided passage resulting from vadose downcutting. The 2008–2014 excavation trench is visible in the foreground; (b) Plan of Con Moong Cave showing position of excavated trenches from investigations in the 1970s and 2008–2014. Position of (c) is marked by red line, and position of section drawing (Fig. 5) is marked by blue line; (c) Profile of excavated trenches as marked by red line in (b). Skull and crossbones symbol marks position of prehistoric human remains excavated during the 1970s and placed in a shrine.

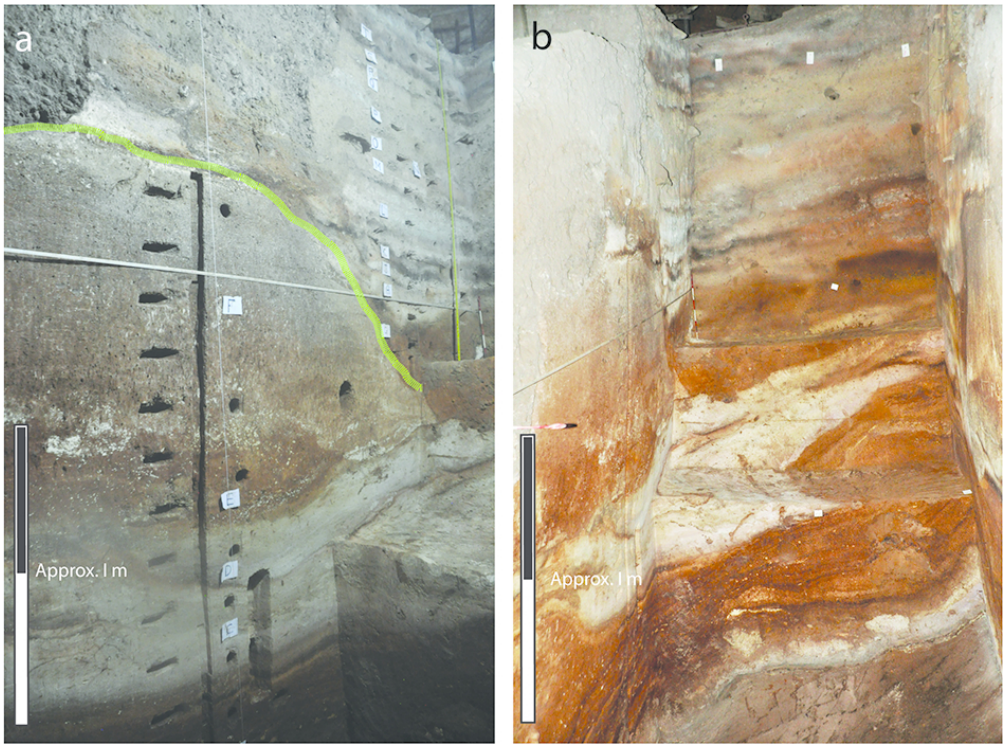


Fig. 3: (a) Photograph of the north-facing section of the trench excavated during the 2008–2014 investigations at Con Moong Cave. Dashed green line shows approximate position of the sloping unconformity between extensively bioturbated lithostratigraphic unit (LSU) F and the overlying sediments; (b) Photograph, taken facing west, of the sediments exposed during the 2008–2014 investigations. Convolute interfaces and flame and load structures are visible in LSUs B and C, suggestive of deformation of liquefied sediment.

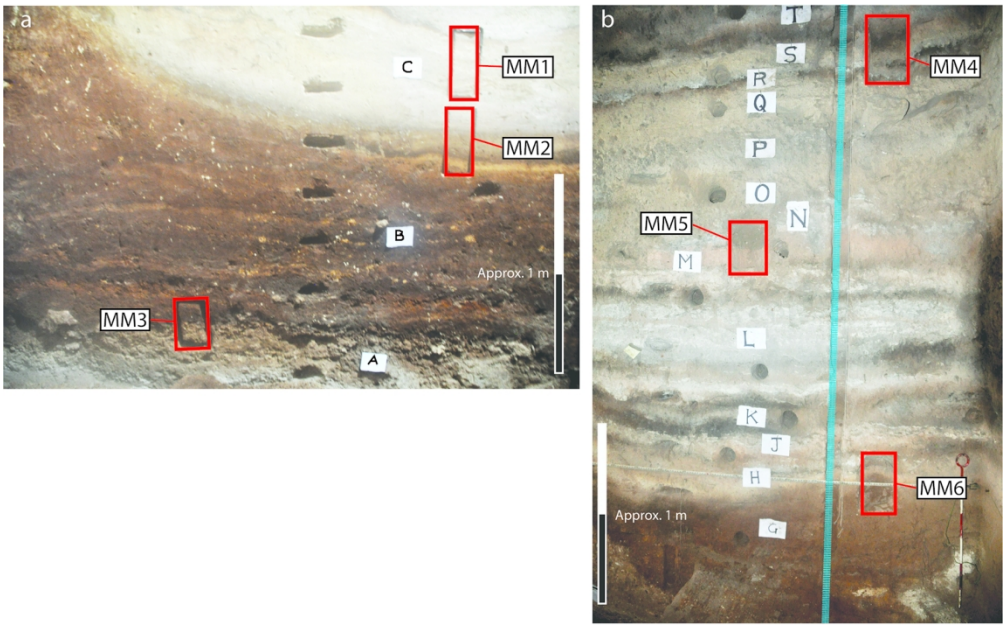


Fig. 4: (a) Photograph of the lower section of the trench profile showing LSUs A–C, taken during the 2014 excavations. Positions of undisturbed blocks MM1–3 are delimited by the labelled red rectangles; (b) Photograph of upper section during 2014 excavations at CMC, showing LSUs G–T. Positions of undisturbed blocks MM4–6 are delimited by the labelled red rectangles. Position of sediment sample column "Column 1" is shown in blue.

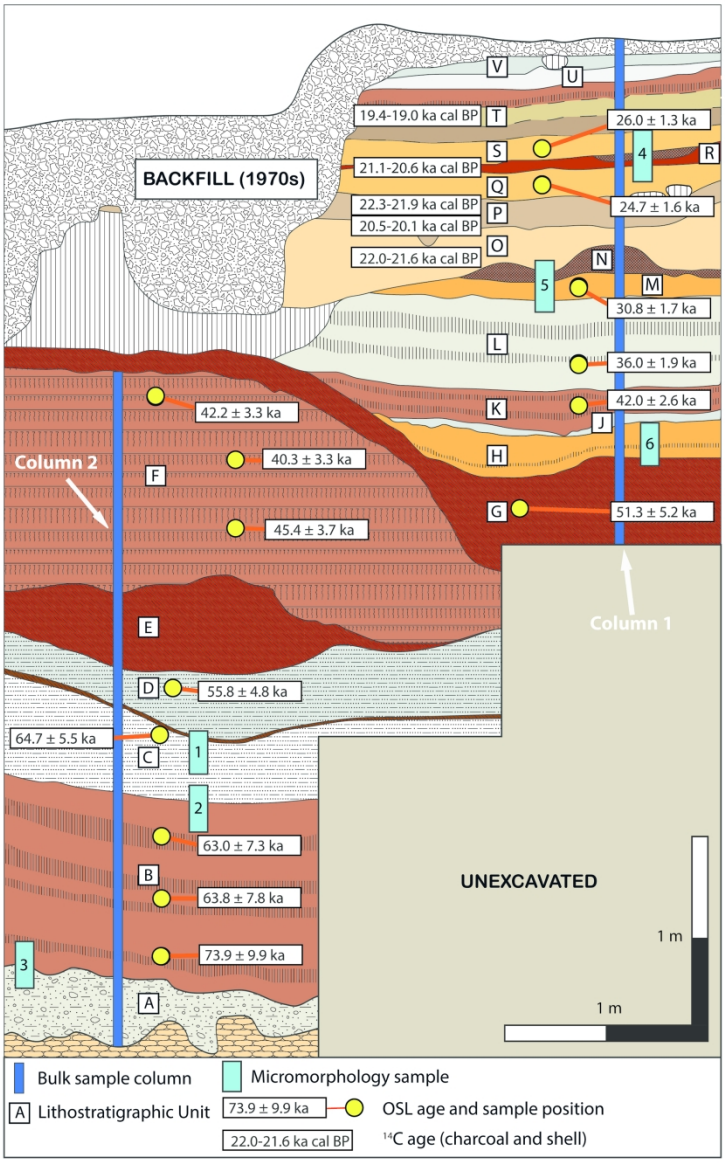


Fig. 5: Section drawing of the north-facing profile exposed during the 2008–2014 investigations (Fig. 2) showing the positions of observed lithostratigraphic units (LSUs), the positions of excavated micromorphological samples, the positions of sediment column samples and the positions and age estimates of OSL and radiocarbon samples. OSL ages are expressed at 1σ and calibrated 14C ages at the 95.4% confidence interval. LSU F demarcates a zone of intensive, macroscopically visible bioturbation (Fig. 3a).

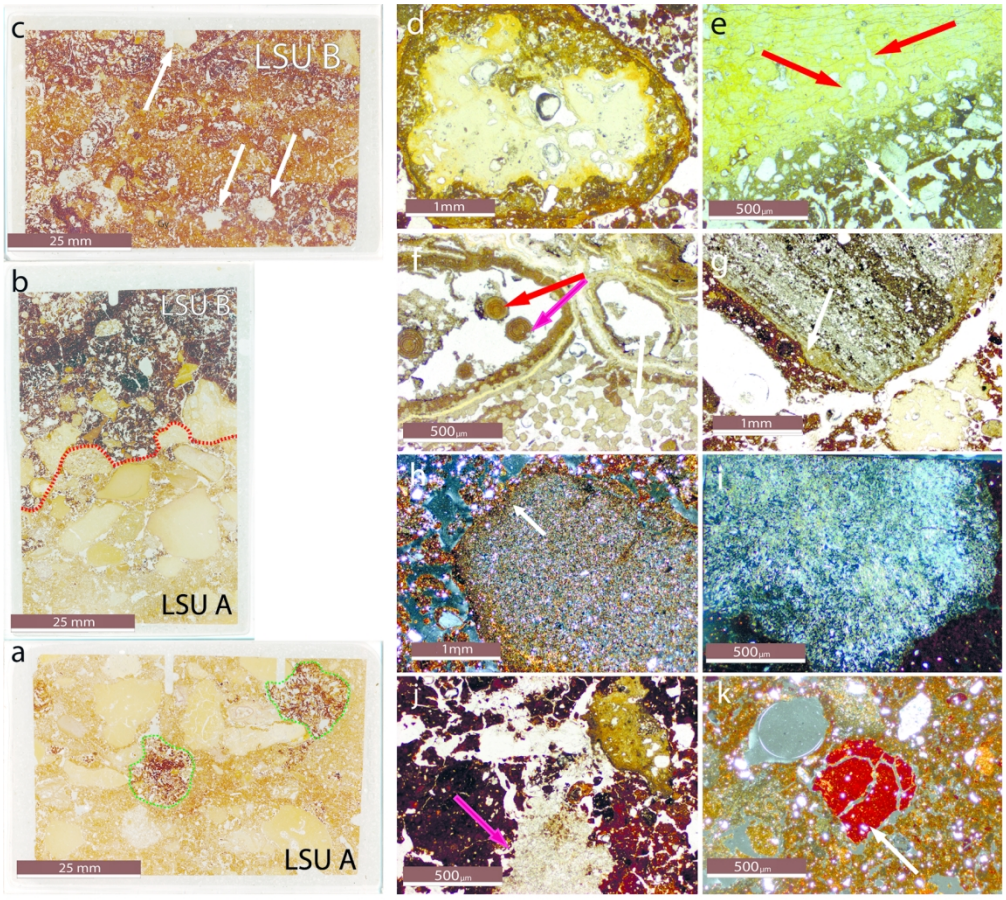


Fig. 6: (a) Flatbed scan of MM3A, with passage features demarcated by green dashed lines; (b) Flatbed scan of MM3B, with red line indicating approximate position of boundary between LSUs A and B; (c) Flatbed scan of MM3C showing concentrations of gypsum crystals (white arrows); (d) Photomicrograph showing authigenic phosphate minerals replacing carbonate gravel (LSU A, MM3B, PPL); (e) Photomicrograph of diagenetically altered bone fragment showing bacterial degradation of internal structure (red arrows) and a clay and quartz pendent (white arrow; LSU A, MM3A, PPL); (f) Photomicrograph showing arrangement of phosphate minerals forming banded nodules (red arrows) and spherulites (white arrows) in diagenetically altered rock fragment (LSU A, MM3A, PPL); (g) Photomicrograph of metamorphic rock fragment with phosphatic reaction rim (white arrow; LSU A, MM3B, PPL); (h) Photomicrograph of rock fragment with pellicular clay hypocoating (white arrow; LSU A, MM3B, XPL); (i) Photomicrograph of gypsic void infill, lenticular crystals (LSU B, MM3C, XPL); (j) Photomicrograph of lenticular gypsum crystals forming partial passage feature infill (red arrow; LSU B, MM3C, PPL); (k) Photomicrograph of fractured clay aggregate within groundmass (white arrow; LSU B, MM3C, XPL). PPL, plane-polarised light; XPL, cross-polarised light.

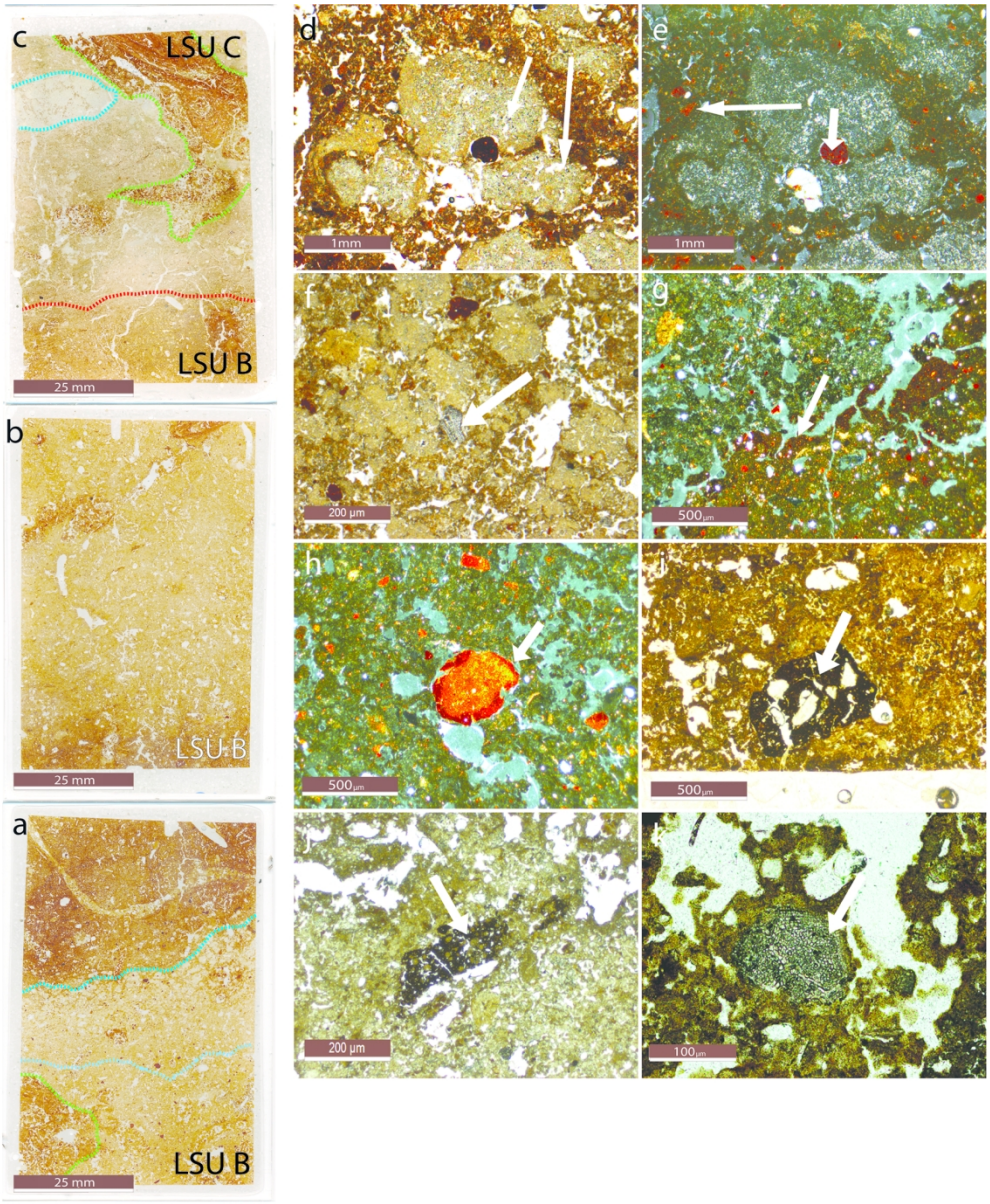


Fig. 7: (a) Flatbed scan of MM2A. Green dashed line marks approximate boundary of clay-lined passage feature. Blue dashed lines demarcate a fabric unit displaying clay weathering and taranakite nodule precipitation (lower boundary is diffuse); (b) Flatbed scan of MM2B; (c) Flatbed scan of MM2C. Red line marks approximate position of diffuse boundary between LSU B and LSU C. Green line demarcates clay-lined passage feature. Blue line encircles area of pronounced taranakite nodule precipitation; (d) Photomicrograph of cluster of taranakite/francoannelite nodules (white arrows) showing irregular alteration to unknown mineral (LSU B, MM2A, PPL); (e) As in panel d, white arrows show clay nodules within groundmass (LSU B, MM2A, XPL); (f) Photomicrograph of plant-derived siliceous aggregate (white arrow) within zone of nodule precipitation (LSU B, MM2A, PPL); (g) Photomicrograph showing difference in b-fabric between zone of nodule precipitation and clay-rich LSU B groundmass (white arrow marks boundary; LSUB, MM2A, XPL); (h) Photomicrograph of irregular, weathered clay nodules within groundmass, (white arrow; LSU B, MM2A, XPL); (I) Photomicrograph of Fe/Mn aggregate (white arrow) containing quartz sand (LSU B, MM2B, PPL);

(j) Photomicrograph of Fe/Mn aggregate containing banded phosphatic nodules (white arrow; LSU B, MM2B, PPL); (k) Photomicrograph of plant-derived siliceous aggregate (white arrow arrow; LSU B, MM2B, PPL).

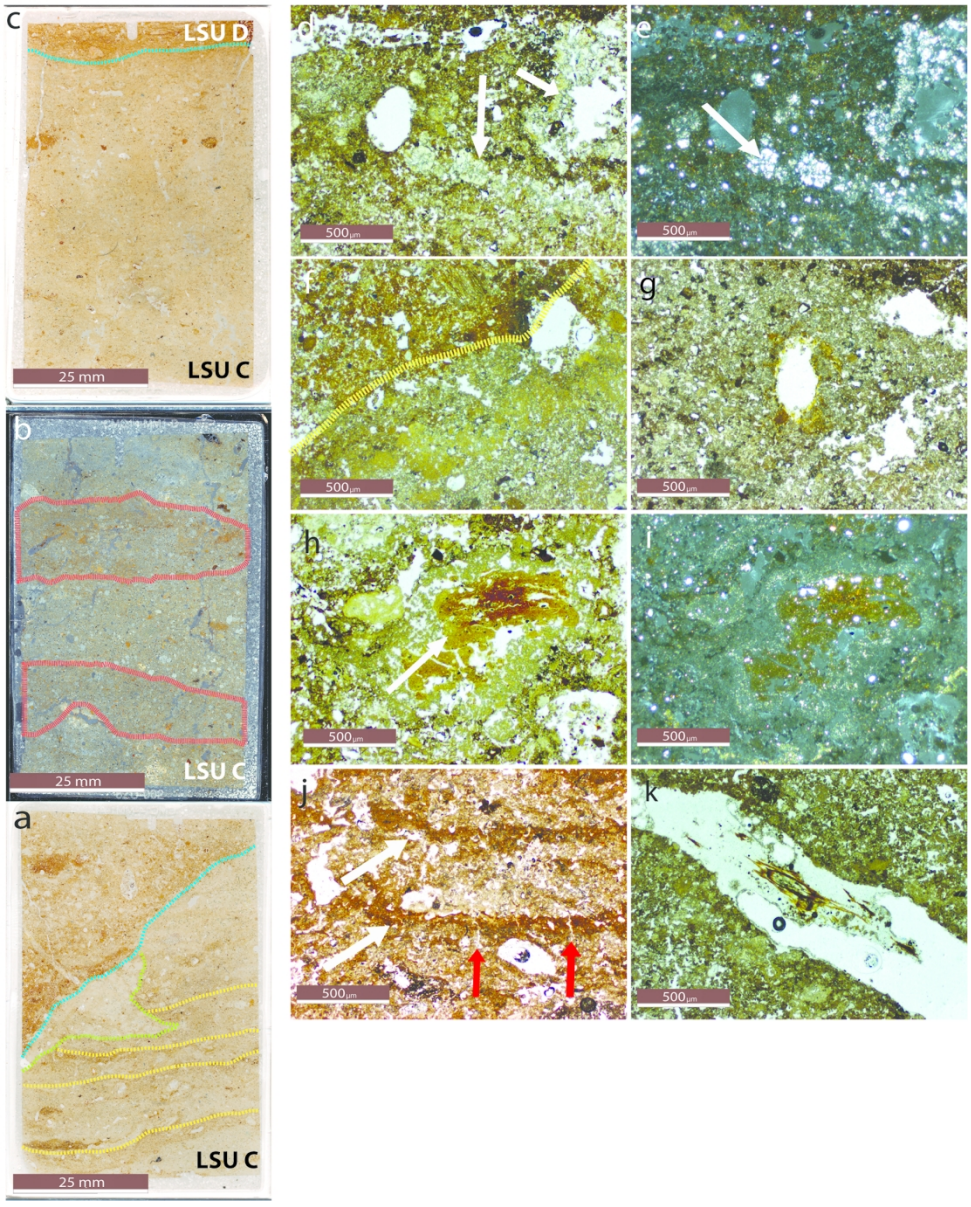


Fig. 8: (a) Flatbed scan of MM1A. Yellow lines show approximate positions of horizontally oriented concentrations of amorphous clays. Green line shows lower boundary of dense concentration of taranakite nodules. Blue line demarcates erosive contact, indicating mass movement event (also panel f); (b) Flatbed scan of MM1B with approximate extent of horizontally-banded, amorphous concentrations of clay demarcated by dashed red line (darkfield); (c) Flatbed scan of MM1C. Blue line indicates lower extent of upward-fining microlaminations (also panel j); (d) Photomicrograph showing diversity of authigenic minerals within groundmass. Birefringent minerals form horizontal concentrations and partial void infills (white arrows). Various isotropic nodules are also visible (LSU C, MM1A, PPL); (e) As in panel d, white arrow shows birefringent crystalline mineral (LSU C, MM1A, XPL); (f) Photomicrograph of erosive contact, associated with amorphous concentration of clay, marked by dashed yellow line (LSU C, MM1A, PPL); (g) Photomicrograph of clay coating/hypocoating on vugh (LSU C, MM1A, PPL); (h) Photomicrograph of multi-phase nodule with a strongly ferruginised core (white arrow; LSU C, MM1B, XPL) (i) As in panel h (LSU C, MM1B, XPL); (j) Photomicrograph of upward-fining microlaminations (white arrows) displaying micro-scale cracking (red arrows; LSU D, MM1C, PPL); (k) Photomicrograph of oxidised root pseudomorph (LSU C, MM1B, PPL).

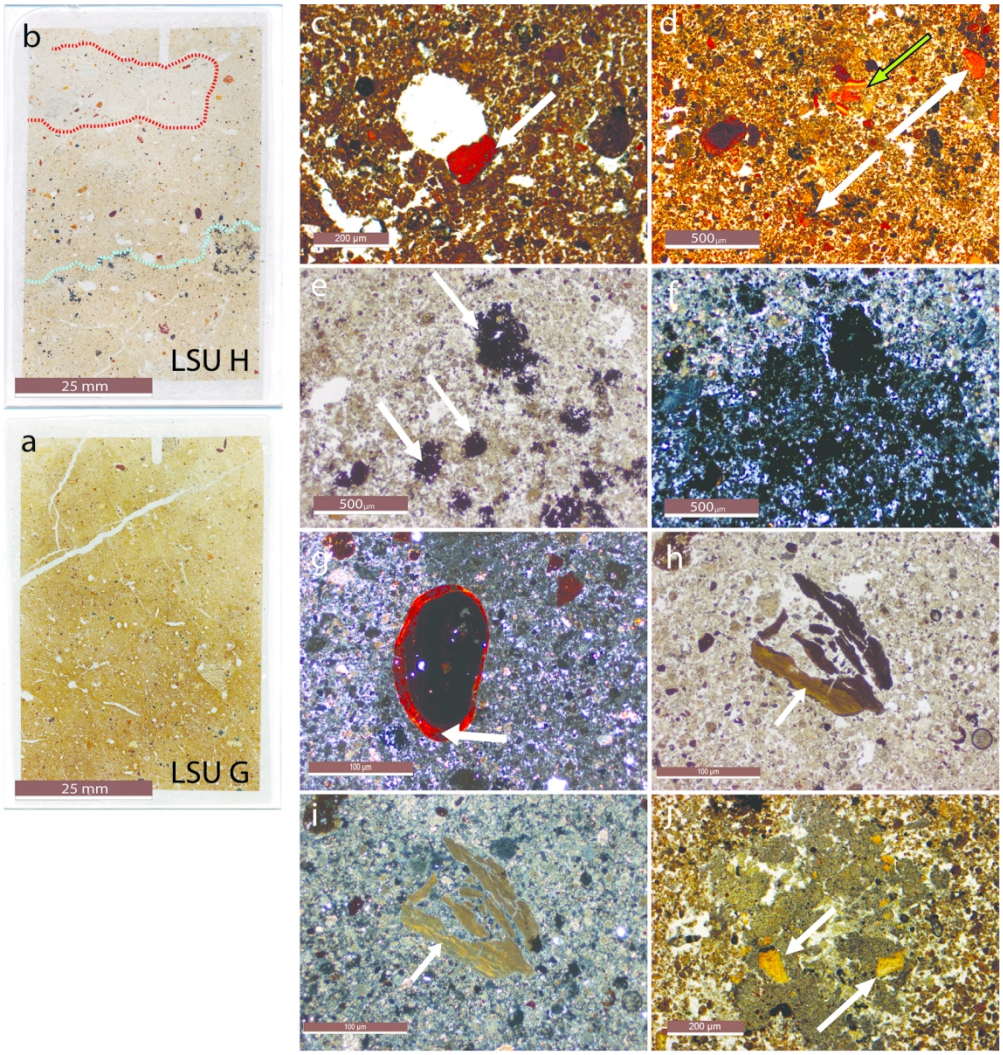


Fig. 9: (a) Flatbed scan of MM6A. (b) Flatbed scan of MM6B, with dashed blue line demarcating upper limit of phosphatisation in LSU H and dashed red line marking the extent of a welded, ashy aggregate; (c) Photomicrograph showing sand-sized, altered bone fragment associated with faunal void (white arrow; LSU G, MM6A, PPL); (d) Photomicrograph of fragmentary clay aggregates throughout groundmass (white arrows) and fragmentary phosphatised clay coatings (green arrow) (LSU G, MM6A, PPL); (e) Photomicrograph showing zone of Mn oxide nodule (white arrows) precipitation at upper limit of phosphatised sediment (LSU H, MM6B, PPL); (f) As in panel e (LSU H, MM6B, XPL); (g) Photomicrograph of clay nodule displaying Fe/Mn depletion hypocoating (white arrow), located at LSU H decalcification boundary (LSU H, MM6B, XPL); (h) Photomicrograph of Sand-sized, bone fragment, possibly burnt, fractured in situ (LSU H, MM6B, PPL); (i) As in panel h, showing replacement with calcite (LSU H, MM6B, XPL); (j) Photomicrograph of sand-sized bone fragments (white arrows) within irregular aggregate of grey, isotropic mineral (LSU H, MM6B, XPL).

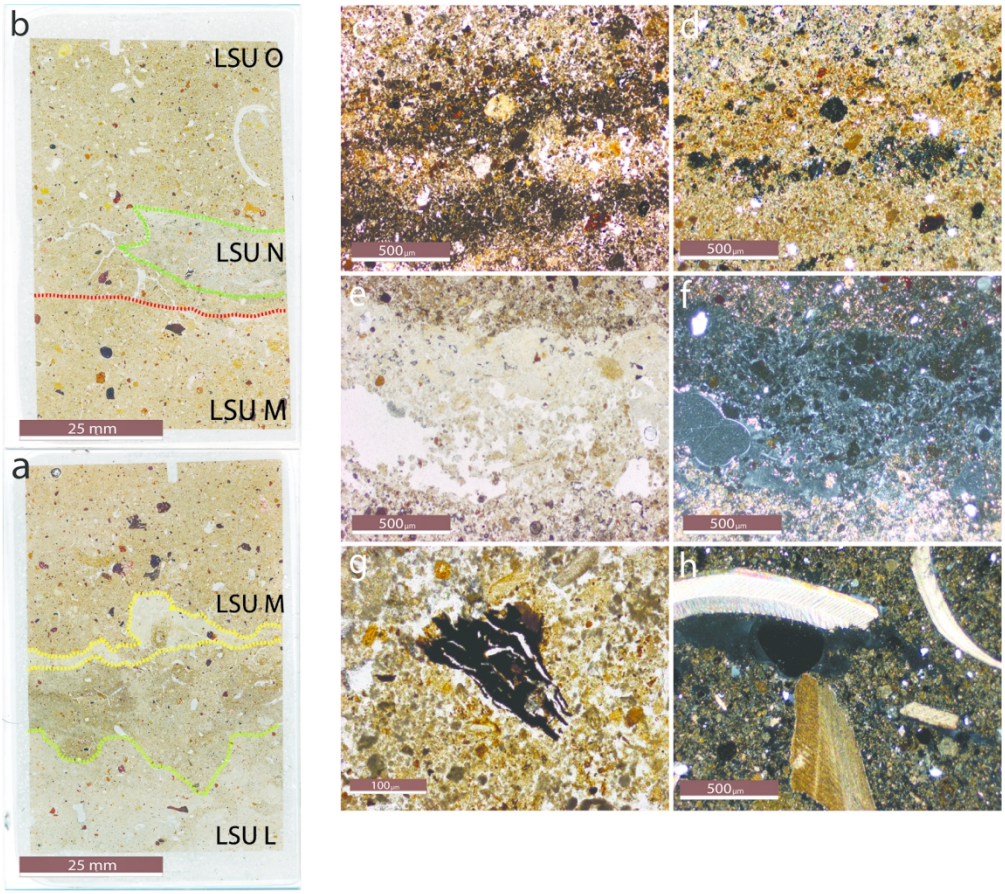


Fig. 10: (a) Flatbed scan of MM5A, showing LSUs L and M with a phosphatic crust precipitated at their interface (demarcated by dashed yellow lines) and the lower limit of an underlying zone of limited phosphatisation (marked with dashed green line); (b) Flatbed scan of MM5B, showing the interfaces between LSUs M, N and O. Upper boundary of LSU M is demarcated by a dashed red line. The extent of LSU N, as visible in this thin-section, is delimited with a dashed green line; (c) Photomicrograph of ashy laminations (LSU L, MM5A, PPL); (d) As in panel c (LSU L, MM5A, XPL); (e) Photomicrograph of isotropic phosphate crust precipitated between LSUs M and N (MM5A, PPL); (f) As in panel e (MM5A, XPL); (g) Photomicrograph of charcoal fragment (LSU O, MM5B, XPL); (h) Photomicrograph of shell fragments, some of which have been replaced with calcite (LSU O, MM5B, XPL).

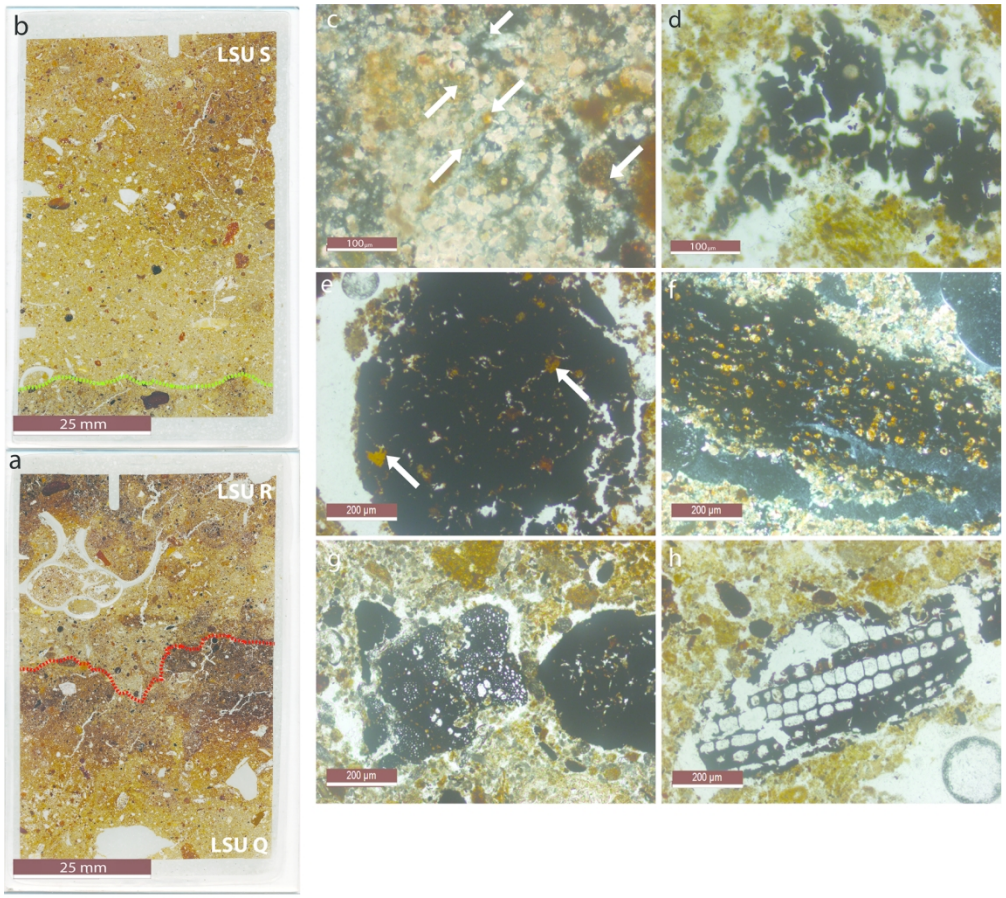


Fig. 11: (a) Flatbed scan of thin-section MM4A with dashed red line indicating upper boundary of LSU Q; (b) Flatbed scan of MM4b with dashed green line indicating approximate interface between LSUs R and S; (c) Photomicrograph showing concentration of ash rhombs (white arrows; LSU R, MM4A, PPL); (d) Photomicrograph showing charred organic aggregate displaying in situ fracturing (LSU R, MM4A, PPL); (e) Photomicrograph showing rounded, degraded charcoal fragment with clay infills in voids (white arrows; LSU R, MM4A, PPL); (f) Photomicrograph of degraded charcoal with clay infills of internal voids (LSU R, MM4A, XPL); (g) Photomicrograph of degraded and humified charcoal with deformation of internal voids, mineral precipitation and evidence of bioerosion (LSU R, MM4A, PPL); (h) Photomicrograph of well-preserved charcoal fragment displaying limited mineral precipitation in internal void and restricted humification around outer extent (LSU R, MM4B, PPL).

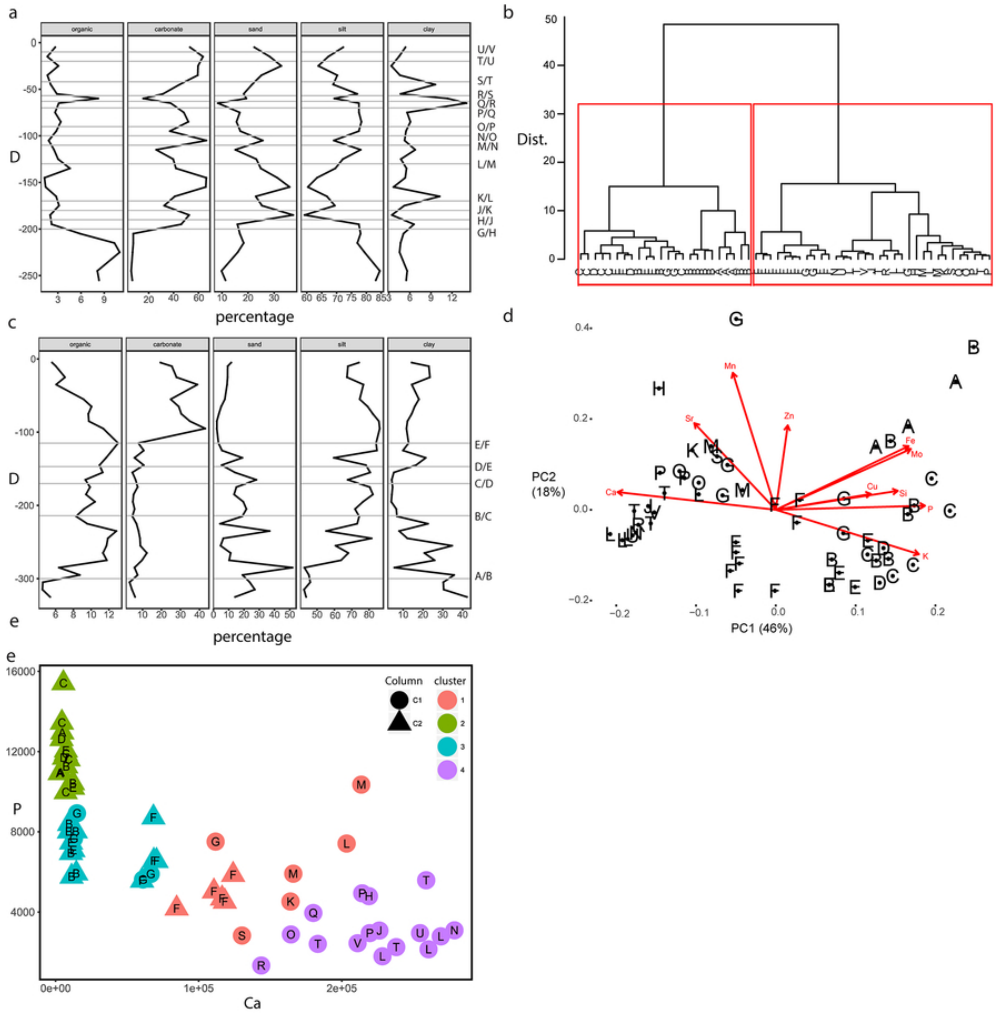


Fig. 12: (a) Loss-on-ignition and particle-size results for Column 1 samples with grey lines marking stratigraphic interfaces. "D" on y-axis indicates depth from top of sediment sample column; (b) Dendrogram showing results of hierarchical clustering (Ward's method) of portable X-ray fluorescence (pXRF) data, "Dist." on y-axis indicates Euclidean distance, samples are labelled by LSU. Red rectangles demarcate 2 stable clusters suggested by plotting within groups sum of squares; (c) Loss-on-ignition and particle-size results for Column 2 samples with grey lines marking interfaces. "D" on y-axis indicates depth from top of sediment sample column; (d) Score and loading biplot showing first two principal components of pXRF data (PC1 and PC2) and proportion of variance explained (%), labelled by LSU; (e) Scatterplot showing distribution of Ca/P values (µg/g; measured using pXRF) of sampled sediments and 4 k-means clusters, labelled by sediment sample column and LSU.

76x77mm (300 x 300 DPI)

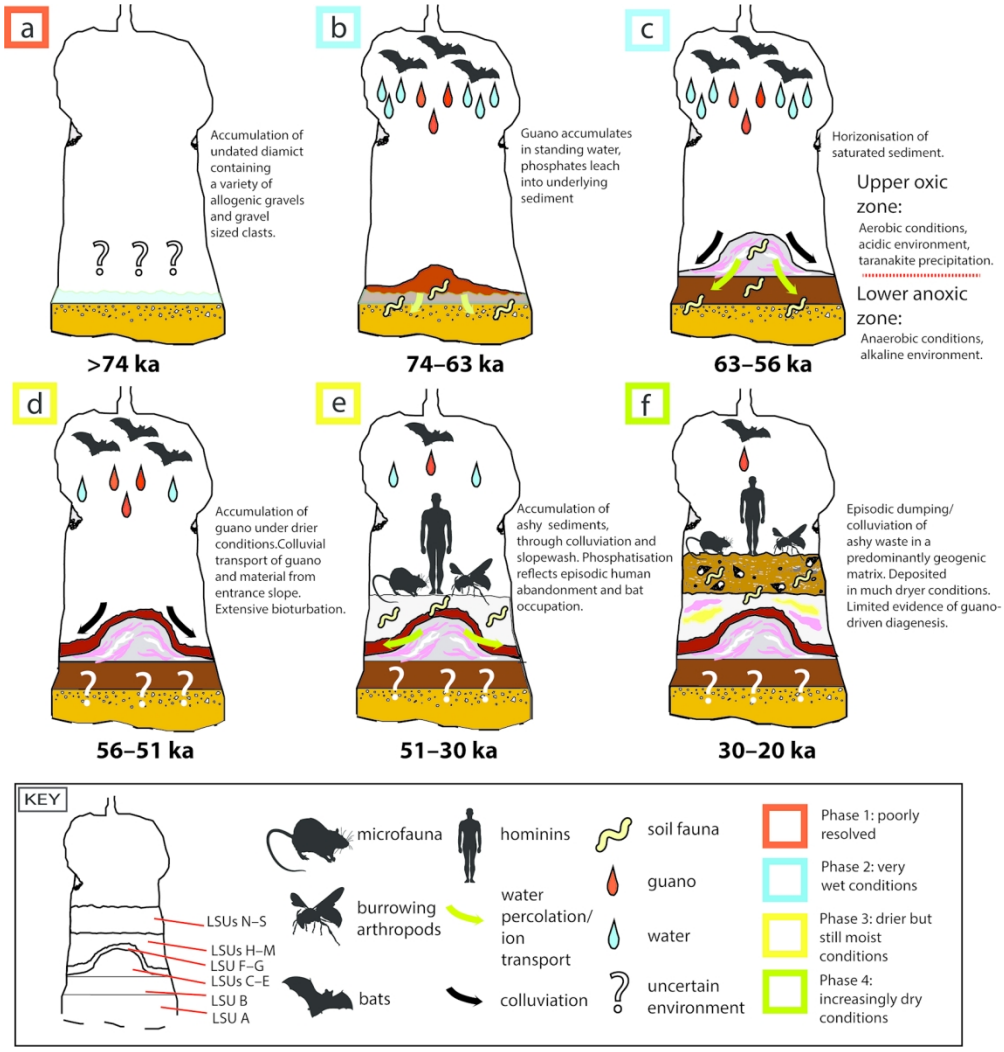


Fig. 13: Illustration showing phases of sedimentation at Con Moong Cave: (a) Deposition of undated basal diamict; (b) Accumulation of waterlogged guano deposit LSU B during early Marine Isotope Stage (MIS) 4; (c) Horizonisation of growing guano deposit due to differences in sedimentary redox environment, with LSUs C–E accumulating during MIS 4; (d) Colluvial deposition of guano and mixed allogenic and autogenic material (LSUs F and G) including soil aggregates, in a drier but still moist environment during early MIS 3; (e) Colluvial deposition and syn-depositional reworking of ashy occupation deposits, with layers of phosphatic silt indicating episodes of anthropogenic abandonment and bat colonisation (LSUs H–M); (f) Switch to drier conditions and predominantly geogenic deposition of carbonate silt and sand with pedological inputs during MIS 2. Evidence for sporadic human occupation is distributed throughout, sometimes forming ephemeral layers, episodic bat occupation is also evident (LSUs N–S). Wasp vector from svgsilh.com used under CCO 1.0; Rat vector by Natasha Sinegina, taken from http://www.supercoloring.com used under CC BY-SA 4.0; human vector by Ikaros Ainasoja hosted at http://freevectors.net.

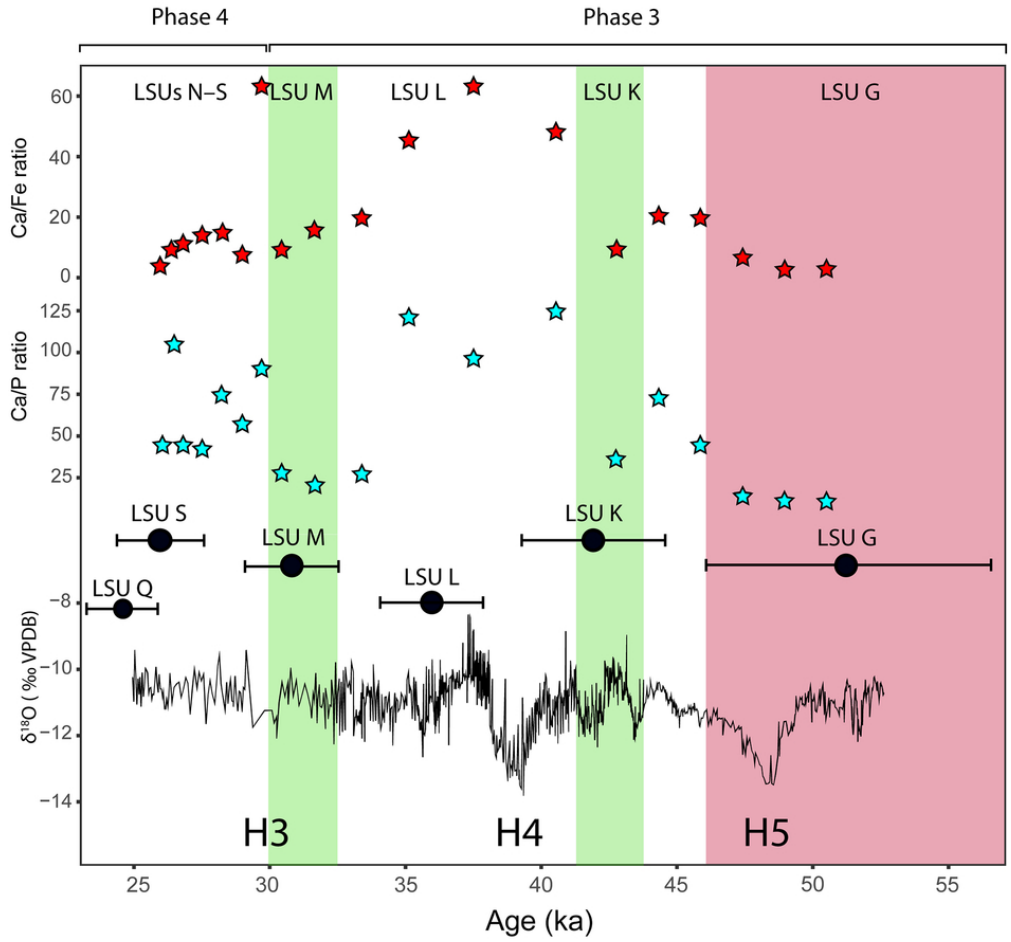


Fig. 14: Comparison of Ca/Fe ratios (red stars) and Ca/P ratios (blue stars) from Column 1 samples, reflecting proportions of pedogenic and guano/ash inputs, respectively. The composite δ18O record from Xiaobailong Cave, southern China (lower curve), is used here as a measure of Indian Monsoon Intensity and regional precipitation (Cai et al. 2006; 2015). H3–5 denote episodes of reduced monsoon signal linked to Heinrich events 3–5 (Cai et al. 2015). Green areas demarcate the linearly interpolated periods during which guano-rich LSUs M and K were deposited. Red area demarcates interpolated deposition of LSU G, another guano-rich unit. Black circles and error bars denote OSL ages and 1σ uncertainties for the LSUs shown. Plotted against the Xiaobailong Cave data, our results suggest that throughout MIS 3 periods of anthropogenic abandonment may correspond with millennial-scale reductions in precipitation. During MIS 2 rapid climate fluctuations correspond with large variations in the Ca/P ratio of LSUs N–S, reflecting the short-lived occupation events observed in thin section. The low Ca/Fe ratios during MIS 2 reflect the switch to geogenic deposition also observed in thin section.

80x78mm (300 x 300 DPI)

**Table 1:** Summary results of field observations, dating and thin section micromorphology for each investigated lithostratigraphic unit (LSU). OSL ages are expressed at 1σ and calibrated $^{14}$C ages at the 95.4% confidence interval.

| LSU | Field Description | Dates | Micromorphological features |
|---|---|---|---|
| V | Ashy grey/black silt with frequent mollusc shells. | NA | NA |
| U | Ashy grey/black silt and sand. | NA | NA |
| T | Banded black, grey and grey-brown silts, reddish lens at lower interface. | V14-1: 19,360–18,980 cal BP ($^{14}$C gastropod shell) | NA |
| S | Layered orange/buff-brown and grey brown silt. | CMC14-3: 26 ± 1.3 ka (OSL) | Spongey fabrics, weakly stipple-specked to undifferentiated, decalcified groundmass. Superimposed ashy coatings and calcite hypocoatings around vughs, concentrations grade upwards. Carbonates in groundmass grade upwards. Coarse, sub-rounded carbonate sand with weakly-expressed reaction rims. |
| R | Layered ashy grey-brown/black silt/ sand. Frequent fragmentary mollusc shells. | V14-2: 21,050–20,610 cal BP ($^{14}$C charcoal) | Well-preserved ashes within carbonate-rich matrix, charcoal shows extensive rounding and humification. Extensive bioturbation and microbial degradation of bone inclusions. |
| Q | Buff-brown silt/sand, poorly sorted. Frequent sub-angular carbonate gravel, occasional fragmentary mollusc shell. | CMC14-4: 24.7 ± 1.6 ka (OSL) | Coarse, sub-angular carbonate sand/gravel and quartz sand within brown silt matrix. Welded carbonate b-fabric. Infrequent bone and shell fragments. |
| P | Grey-brown silt. | V14-3: 22,320–21,880 cal BP ($^{14}$C gastropod shell)<br><br>V14-4: 20,500–20,100 cal BP ($^{14}$C gastropod shell) | NA |

| | | | |
|---|---|---|---|
| O | Grey-brown/buff-brown silt/sand, occasional fragmentary mollusc shells. | V14-5: 22,030–21,550 ($^{14}$C charcoal) | Poorly-sorted carbonate silt, sub-angular carbonate and quartz sand. Contains frequent shell fragments and soil aggregates with occasional charcoal fragments. |
| N | Irregular grey silt layer. | NA | Lens of extensively-bioturbated, welded, ashy micritic calcite. |
| M | Horizontally bedded pink silt layer, separated from LSU L by black/brown lens. | CMC14-6: 30.8 ± 1.7 ka (OSL) | Extensively-bioturbated pinkish silts with undifferentiated b-fabric and isotropic phosphate crust at lower boundary with carbonate-rich LSU L. Oxidised, iron-replaced organic matter visible throughout. |
| L | Ashy, grey layer with horizontally-banded lenses of black/brown silt. | CMC14-8: 36 ± 1.9 ka (OSL) | Spongey fabric throughout. Burned soil aggregates form minor inclusions as do sand-sized charcoal fragments. Microcharcoal distributed throughout groundmass. Localised fabric unit preserves laminations of ashy sediment. |
| K | Horizontally banded pink, grey-brown and black silts. | CMC14-9: 42 ± 2.6 ka (OSL) | NA |
| J | Horizontally bedded grey-brown and buff-brown silts. | NA | NA |
| H | Horizontally-bedded orange, grey-brown and buff-brown silts. | | Ashy sediments displaying extensive bioturbation and recrystallisation. The lower extent of the sediment displays undifferentiated b-fabric and frequent Fe/Mn nodules. Bone and shell display diagenetic alterations. |
| G | Red silt, apparently forms sloping interface with underlying LFU F, however extensive bioturbation obscures stratigraphic relationship. | CMC14-11: 51.3 ± 5.2 ka (OSL) | Reddish-brown silt aggregates. Undifferentiated b-fabric with extensively altered sand-sized bone fragments. Fragmentary laminar clay aggregates. Soil aggregates and Fe/Mn nodules throughout. |

| | | | |
|---|---|---|---|
| F | Reddish silt, evidence of extensive vertical burrowing which obscures relationship to other layers. Dense accumulation of white nodules throughout. | CMC14-12: 42.2 ± 3.3 ka (OSL)<br><br>CMC18-1: 40.3 ± 3.3 ka (OSL)<br><br>CMC18-2: 45.4 ± 3.7 ka (OSL) | NA |
| E | Buff-brown/reddish silt/clay with dense concentrations of white/grey nodules ~10mm diameter. | NA | NA |
| D | Grey silt. Extensive load structures and convolute bedding, grey/white nodules throughout. Lower boundary marked by sloping lens of dark material. | CMC14-15: 55.8 ± 4.8 ka (OSL) | Lowermost extent of D is visible, consisting of upward-fining laminations sorting material from sand-sized greyish microaggregates to isotropic clays. |
| C | Grey silt. Extensive load structures and convolute bedding, grey/white nodules throughout. | CMC14-16: 64.7 ± 5.5 ka (OSL) | Erosive contacts, horizontally-banded, amorphous clay concentrations, extensive bioturbation. Isotropic groundmass with extensive taranakite nodule formation throughout. Clay coatings/hypocoatings and clay lined passage features are present. Laminar fabrics make up a minor groundmass component. |
| B | Heterogeneous deposit of red/brown silt/clay. Evidence of deformation in the form of flame/load structures. Concave features of layered black and grey nodular silt lenses grade towards the | CMC14-18: 63.0 ± 7.3 (OSL)<br><br>CMC14–19: 63.8 ± 7.8 (OSL) | Extensive bioturbation and spatially varied mineral authigenesis. Undifferentiated b-fabric. Features include gypsum nodules, clay weathering and taranakite formation. Discrete areas of laminar fabric. |

| | | | |
|---|---|---|---|
| | upper boundary, forming a diffuse interface with overlying layer. | CMC14-20: 73.9 ± 9.9 (OSL) | |
| A | Diamict containing buff-coloured, gravel sized clasts in dark brown/black silt/clay matrix. | NA | Extensive bioturbation and phosphatic diagenesis. Gravels show extensive and varied alterations. |

| Lithotratigraphic unit | Visible in thin-sections | Mineral species identified through X-ray diffraction |
|---|---|---|
| A | MM3A, MM3B | quartz, leucophosphite, vivianite, variscite, gypsum |
| B (lower) | MM3B, MM3C | quartz, tinsleyite, vivianite, variscite, gypsum |
| B (upper) | MM2A, MM2B, MM2C | quartz, tinsleyite, vivianite, variscite |
| C (Lower) | MM2C | quartz, taranakite/ francoannelite , variscite, |
| C (upper) | MM1A, MM1B, MM1C | quartz biotite, taranakite/ francoannelite , variscite, vivianite, |
| D | As above | quartz, biotite, variscite, vivianite, taranakite/ francoannelite |
| E | NA | quartz, potassium aluminium phosphate, francoannelite |
| F | NA | quartz, gypsum, bassanite |
| G | MM6A | whitlockite, apatite (mixed), quartz, clays |
| H | MM6A, MM6B | calcite, aragonite Layer silicates |
| M | MM5A | quartz, apatites, calcite |
| N | MM5A, MM5B | quartz, calcite, aragonite, crandallite |
| O | MM5B | quartz, |

| | | |
|---|---|---|
| | | calcite,<br>aragonite,<br>apatites |
| Q | MM4A | quartz,<br>calcite,<br>apatites |
| S | MM4B | quartz,<br>apatites,<br>calcite |

**Table 2:** Mineral species identified through X-ray diffraction, by lithostratigraphic unit (LSU). Diffractograms are provided in Supplementary Information (Table S7).

| Variable | PC1 | PC2 | PC3 |
|---|---|---|---|
| cumulative proportion of variance explained (%) | 46 | 64 | 77 |
| Cu | 0.25772119 | 0.07553735 | **0.5639048** |
| Zn | 0.03241431 | 0.40226843 | **-0.58572096** |
| Si | 0.33044313 | 0.09026851 | -0.234027 |
| P | **0.40419011** | 0.01945502 | -0.249198298 |
| K | **0.38772014** | -0.21148764 | -0.281349116 |
| Ca | **-0.42872327** | 0.08422672 | 0.007156702 |
| Mn | -0.11656701 | **0.65252567** | -0.056746888 |
| Fe | 0.35978589 | 0.30323051 | 0.268751524 |
| Sr | -0.22100079 | 0.41275373 | 0.113080124 |
| Mo | 0.36600702 | 0.28986552 | 0.233732017 |

**Table 3:** Rotations of the first 3 principal components identified through principal component analysis of portable X-ray fluorescence data, along with cumulative proportion of variance explained. Significant scores are printed in **bold**.

# Supplementary Information

## Optically stimulated luminescence (OSL) dating

A total of 14 sediment samples were dated in this study (Tables S2–S4), comprising 12 samples collected in 2014 from stratigraphic units B to S (samples CMC14-3 to -20) and two samples collected in 2018 from unit F (samples CMC18-1 and -2). The OSL samples were collected at night under safe (dim red) light conditions or during the daytime using stainless steel tubes; in both cases, the section face was first cleaned before sampling. At each OSL sample location, separate sediment samples were collected and sealed in plastic zip-lock bags for moisture content determination and dose rate measurement in the laboratory. The OSL samples were prepared under dim red light in the Luminescence Dating Laboratory at the University of Wollongong, using the same procedures as described by Galbraith et al. (1999), including etching of the separated quartz grains with 40% hydrofluoric acid to remove their outer, alpha-dosed rinds. Grains of 180–212 µm in diameter were used for equivalent dose ($D_e$) determination.

$D_e$ values were estimated using a single-aliquot regenerative-dose procedure (Galbraith et al., 1999; Murray and Wintle, 2000), using the OSL IR depletion ratio test (Duller, 2003) to identify and reject quartz grains containing infrared-sensitive inclusions (e.g., feldspars). Table S1 lists the procedural steps used in this study. Individual quartz grains were mounted on 1 cm-diameter aluminium discs drilled with a 10 × 10 array of holes, each 300 µm deep and 300 µm in diameter (Bøtter-Jensen et al., 2003). OSL measurements were carried out on a Risø DA-20 TL/OSL reader using a focussed 10 mW green (532 nm) laser for optical stimulation and an Electron Tubes Ltd 9235QA photomultiplier tube (fitted with a 7.5 mm Hoya U-340 filter) for OSL detection. The OSL signals were measured at a readout temperature of 125 °C and recorded for 2 s. The net OSL signals for $D_e$ estimation were calculated from the counts in the initial 0.2 s of OSL decay, with the mean count over the final 0.3 s subtracted as background. A preheat of 240 °C for 10 s and a cutheat of 200 °C were given prior to the optical stimulations, based on the results of dose recovery tests (Galbraith et al., 1999) for three of three samples (Fig. S1). This combination yielded ratios of measured dose to given dose close to unity (0.96–1.01) and low 'overdispersion' values (5–7%) for the dose distributions (Galbraith et al., 2005). The rejection criteria of Jacobs et al. (2006, 2008) were applied to discard grains with aberrant luminescence characteristics (Table S2), which may result in inaccurate $D_e$ estimates. The resulting $D_e$ distributions have overdispersion values of between 17% and 60% and are spread around a central value (Fig. S2). There are no obvious clusters or other patterns in the distributions of $D_e$ values that suggest the samples suffered from partial bleaching or post-depositional disturbance resulting in discrete $D_e$ components (Jacobs and Roberts, 2007; Roberts et al., 2015), so the central age model (Galbraith et al., 1999; Galbraith and Roberts, 2012) was used to calculate the weighted mean $D_e$ of each sample for purposes of age determination.

The beta dose rates of all samples were measured using a Risø GM-25-5 beta counter (Bøtter-Jensen and Mejdahl, 1988) using the procedures described in Jacobs and Roberts (2015). We also measured the beta dose rates of 11 of the 14 samples using inductively-coupled plasma mass spectrometry/optical emission spectroscopy, to compare the beta dose rates calculated from the concentrations of the parent nuclides in the U and Th decay chains and of K (each measured separately), with the beta dose rates derived from beta counting, which detects the beta emissions from the U and Th chains and $^{40}K$ combined. The beta dose rates obtained using the two techniques (both measured on dried and powdered samples) are consistent at either 1σ or 2σ (Fig. S3) for all 11 samples. This implies that any disequilibrium in the U and Th chains is not a significant issue for our samples, and provides confidence in the reliability of the beta dose rate estimates. The gamma dose rates of all samples were measured in the field using an ORTEC digiDART gamma-ray spectrometer. Cosmic-ray dose rates were evaluated following Prescott and Hutton (1994),

taking into account the site latitude, longitude and altitude, as well as the thickness of the rock shielding (~50 m) and sediment overburden.

Allowance was made for attenuation of the external components of the total dose rate (beta, gamma and cosmic) due to the presence of moisture in the sediments, using the measured (field) moisture contents and the attenuation factors reported by Nathan and Mauz (2008) and Readhead (1987). Dose rate details are given in Table S3. The moisture contents were determined from sediment collected from the back of the OSL sampling holes and measured shortly after collection to avoid desiccation during storage. We assigned a relative error of ± 25% (at 1σ) to these measured values to accommodate (at 2σ) any likely fluctuations in the mean long-term moisture content over the period of burial of our samples, given the humid tropical environment of North Vietnam and the udic soil moisture regime of the region (United States Department of Agriculture, 1997; O'Geen, 2012). Climate-driven variations in soil moisture will be smaller in such environments than in climatic regimes with pronounced wet and dry seasons, and especially in a high-humidity cave setting, such as CMC.

Variability in moisture content can also depend on sediment properties (e.g., Nelson and Rittenour, 2015; Rosenzweig and Porat, 2015). At CMC, the moisture contents vary markedly among the different samples (Table S3), in accordance with differences in particle size between and within stratigraphic units (Fig. 12a,c). The silt- and clay-rich samples commonly have higher moisture contents than do samples with a greater proportion of sand. The three samples with the highest moisture contents are from unit G (CMC14-11, 74%) and the top half of unit B (CMC14-18, 72% and CMC14-19, 64%), both of which are enriched in silt and clay (Fig. 12a,c). The latter two samples overlie CMC14-20, which is also from unit B but has a lower moisture content (36%), consistent with its higher sand content. For age estimation, therefore, we have assumed that the field moisture contents of our samples are a reasonable approximation of the long-term mean values. Support for this assumption is provided by the stratigraphic consistency of the OSL ages and the correlation between the moisture contents and grain-size characteristics of the CMC samples.

The final OSL ages for all samples are summarised in Table S4; the calculated ages increase (or decrease) by ~1% for each 1% increase (or decrease) in moisture content. The ages are mostly in stratigraphic order and range from ~74 ka (base of unit B) to ~25 ka (units S and Q). The mean age of the sample from unit G (51.3 ka) is older than the mean ages of the three samples from the underlying unit F (40.3–45.4), but all four estimates are consistent at 2σ; the 'homogeneity test' (Galbraith, 2003; Galbraith and Roberts, 2012) indicates they are compatible with a common value, taking into account the associated age uncertainties ($p = 0.27$).

**Radiocarbon dating**

Two charcoal samples from units O and R and three freshwater shell samples from units P and T were submitted to the Radiocarbon Dating Laboratory at University of Waikato for accelerator mass spectrometry (AMS) radiocarbon ($^{14}C$) dating. Samples were first inspected under >10× magnification to select the visibly cleanest and least diagenetically altered fragments for dating, which were then washed in distilled water and crushed to increase the surface area for subsequent pretreatment. Charcoal samples were given a dilute acid / dilute alkali (base) / dilute acid (commonly termed AAA or ABA) pretreament. Freshwater shell samples were etched with dilute hydrochloric acid to minimise the possibility of contamination through isotopic exchange between the sample and its environment. The aragonitic shell samples were analysed by X-ray diffraction prior to dating to ensure that recrystallisation had not occurred. Charcoal samples were converted to $CO_2$ by oxidation at 800 °C overnight in the presence of pre-baked CuO wire and silver wire. $CO_2$ was collected from shells by reaction with 85% phosphoric acid under vacuum at 70 °C for ~30 min, and then reduced to graphite in a hydrogen atmosphere at 550 °C using an iron catalyst.

Pressed graphite was measured at the Keck Radiocarbon Dating Laboratory, University of California, Irvine using an AMS system coupled to an in-house modified ion source (Beverly et al., 2010), and the data were analysed following Santos et al. (2007). All $^{14}C$ results were corrected for fractionation using the $\delta^{13}C$ values measured on-line.

Table S5 lists the conventional $^{14}C$ ages for the five samples in radiocarbon years before present (BP, where the 'present' is defined as AD 1950) and as the corresponding calibrated age ranges, expressed in calendar years BP at the 68.2% and 95.4% confidence intervals. Calibrations were performed using the OxCal 4.2.4 platform (Bronk Ramsey, 2009; Bronk Ramsey and Lee, 2013). A comparison between the calibrated ages, which range between 22.3 and 19.0 ka BP at the 95.4% confidence interval, and the OSL ages for units Q and S (24.7 ± 3.2 and 26.0 ± 2.6 ka, respectively, with uncertainties also at the 95.4% confidence interval) shows that the latter are a few millennia older than the $^{14}C$ ages, for reasons that are not yet clear. We note, however, that the OSL age of 24.7 ± 3.2 ka for unit Q is consistent at 2σ with the two of the $^{14}C$ ages, and that all five $^{14}C$ ages and both OSL ages indicate that the upper units of the sampled CMC profile were deposited mostly during the first half of Marine Isotope Stage 2.

**References**


Beverly, R.K., Beaumont, W., Tauz, D., Ormsby, K.M., von Reden, K.F., Santos, G.M., Southon, J.R. (2010). The Keck Carbon Cycle AMS Laboratory, University of California, Irvine: status report. *Radiocarbon, 52*(2), 301–309. DOI:10.1017/S0033822200045343

Bøtter-Jensen, L., Mejdahl, V. (1988). Assessment of beta dose rate using a GM multicounter system. *Nuclear Tracks and Radiation Measurements*, *14*(1–2), 187–191. DOI:10.1016/1359-0189(88)90062-3

Bøtter-Jensen, L., Andersen, C.E., Duller, G.A.T., Murray, A.S. (2003). Developments in radiation, stimulation and observation facilities in luminescence measurements. *Radiation Measurements, 37*(4–5), 535–541. DOI:10.1016/S1350-4487(03)00020-9

Bronk Ramsey, C. (2009). Bayesian analysis of radiocarbon dates. *Radiocarbon, 51*(1), 337–360. DOI:10.1017/S0033822200033865

Bronk Ramsey, C., Lee, S. (2013). Recent and planned developments of the program OxCal. *Radiocarbon, 55*(2), 720–730. DOI:10.1017/S0033822200057878

Duller, G.A.T. (2003). Distinguishing quartz and feldspar in single grain luminescence measurements. *Radiation Measurements, 37*(2), 161–165. DOI:10.1016/S1350-4487(02)00170-1

Galbraith, R.F. (2003). A simple homogeneity test for estimates of dose obtained using OSL. *Ancient TL, 21*(2), 75–77.

Galbraith, R.F., Roberts, R.G. (2012). Statistical aspects of equivalent dose and error calculation and display in OSL dating: an overview and some recommendations. *Quaternary Geochronology, 11,* 1–27. DOI:10.1016/j.quageo.2012.04.020

Galbraith, R.F., Roberts, R.G., Laslett, G.M., Yoshida, H., Olley, J.M. (1999). Optical dating of single and multiple grains of quartz from Jinmium rock shelter, northern Australia: Part I, experimental design and statistical models. *Archaeometry, 41(2),* 339–364. DOI:10.1111/j.1475-4754.1999.tb00987.x

Galbraith, R.F., Roberts, R.G., Yoshida, H. (2005). Error variation in OSL palaeodose estimates from single aliquots of quartz: a factorial experiment. *Radiation Measurements, 39*(3), 289–307. DOI:10.1016/j.radmeas.2004.03.023

Jacobs, Z., Roberts, R.G. (2007). Advances in optically stimulated luminescence dating of individual grains of quartz from archeological deposits. *Evolutionary Anthropology: Issues, News, and Reviews, 16*(6), 210–223. DOI:10.1002/evan.20150

Jacobs, Z., Roberts, R.G. (2015). An improved single grain OSL chronology for the sedimentary deposits from Diepkloof Rockshelter, Western Cape, South Africa. *Journal of Archaeological Science, 63,* 175–192. DOI:10.1016/j.jas.2015.01.023

Jacobs, Z., Duller, G.A.T., Wintle, A.G. (2006). Interpretation of single grain $D_e$ distributions and calculation of $D_e$. *Radiation Measurements, 41*(3), 264–277. DOI:10.1016/j.radmeas.2005.07.027

Jacobs, Z., Wintle, A.G., Roberts, R.G., Duller, G.A.T. (2008). Equivalent dose distributions from single grains of quartz at Sibudu, South Africa: context, causes and consequences for optical dating of archaeological deposits. *Journal of Archaeological Science, 35*(7), 1808–1820. DOI:10.1016/j.jas.2007.11.027

Murray, A.S., Wintle, A.G. (2000). Luminescence dating of quartz using an improved single-aliquot regenerative-dose protocol. *Radiation Measurements, 32*(1), 57–73. DOI:10.1016/S1350-4487(99)00253-X

Nathan, R.P., Mauz, B. (2008). On the dose-rate estimate of carbonate-rich sediments for trapped charge dating. *Radiation Measurements, 43(1),* 14–25. DOI:10.1016/j.radmeas.2007.12.012

Nelson, M.S., Rittenour, T.M. (2015). Using grain-size characteristics to model soil water content: application to dose-rate calculation for luminescence dating. *Radiation Measurements, 81,* 142–149. DOI:10.1016/j.radmeas.2015.02.016

O'Geen, A.T. (2012). Soil water dynamics. *Nature Education Knowledge, 3*(6), 12.

Prescott, J.R., Hutton, J.T. (1994). Cosmic ray contributions to dose rates for luminescence and ESR dating: large depths and long-term time variations. *Radiation Measurements, 23*(2–3), 497–500. DOI:10.1016/1350-4487(94)90086-8

Readhead, M.L. (1987). Thermoluminescence dose rate data and dating equations for the case of disequilibrium in the decay series. *International Journal of Radiation Applications and Instrumentation. Part D. Nuclear Tracks and Radiation Measurements, 13*(4), 197–207. DOI:10.1016/1359-0189(87)90037-9

Roberts, R.G., Jacobs, Z., Li, B., Jankowski, N.R., Cunningham, A.C., Rosenfeld, A.B. (2015). Optical dating in archaeology: thirty years in retrospect and grand challenges for the future. *Journal of Archaeological Science, 56,* 41–60. DOI:10.1016/j.jas.2015.02.028

Rosenzweig, R., Porat, N., 2015. Evaluation of soil-moisture content for OSL dating using an infiltration model. *Ancient TL, 33*(2), 10–14.

Santos, G.M., Moore, R.B., Southon, J.R., Griffin, S., Hinger, E., Zhang, D. (2007). AMS $^{14}C$ sample preparation at the KCCAMS/UCI facility: status report and performance of small samples. *Radiocarbon, 49*(2), 255–269. DOI:10.1017/S0033822200042181

United Stated Department of Agriculture (1997). *Soil Moisture Regimes Map (1:5,000,000).* Retrieved from https://www.nrcs.usda.gov/wps/portal/nrcs/detail/soils/use/?cid=nrcs142p2_054017

**Table S1** Regenerative-dose procedure used for single-grain OSL measurements.

| Step [a] | Treatment<br>Observed [b] |
|---|---|
| 1 | Natural or regenerative dose |
| 2 | Preheat to 240 °C for 10 s |
| 3 | Stimulate with infrared LEDs at 50 °C for 100 s |
| 4 | Stimulate with green laser at 125 °C for 2 s<br>$L_n$, $L_x$ |
| 5 | Test dose |
| 6 | Cutheat to 200 °C |
| 7 | Stimulate with green laser at 125 °C for 2 s<br>$T_n$, $T_x$ |
| 8 | Stimulate with blue LEDs at 250 °C for 40 s |
| 9 | Repeat steps 1–8 for several regenerative doses |

[a] Step 3 is included only when measuring the OSL IR depletion ratio (Duller, 2003).

[b] $L_n$, OSL signal arising from the natural dose; $L_x$, OSL signal arising from each regenerative dose; $T_n$ and $T_x$, OSL signals arising from the test doses given in the natural and regenerative-dose cycles, respectively.

**Table S2** Number of individual quartz grains measured and rejected for each OSL sample, and the reasons for their rejection.

| Sample | CMC14-3 | CMC14-4 | CMC14-6 | CMC14-8 | CMC14-9 | CMC14-11 | CMC14-12 | CMC18-1 | CMC18-2 | CMC14-15 | CMC14-16 | CMC14-18 | CMC14-19 | CMC14-20 |
|---|---|---|---|---|---|---|---|---|---|---|---|---|---|---|
| **Total number of grains measured** | 1100 | 300 | 400 | 500 | 300 | 2300 | 500 | 300 | 500 | 500 | 500 | 1500 | 1600 | 2400 |
| **Reason for rejecting grains** | | | | | | | | | | | | | | |
| $T_n$ < 3σ background [a] | 807 | 187 | 173 | 131 | 132 | 1774 | 252 | 116 | 247 | 155 | 115 | 1077 | 1092 | 1722 |
| $T_n$ relative standard error > 20% | 155 | 54 | 44 | 77 | 64 | 340 | 92 | 78 | 120 | 96 | 36 | 253 | 303 | 497 |
| Recycling ratio ≠ 1 at 2σ | 11 | 10 | 30 | 29 | 8 | 16 | 15 | 12 | 21 | 20 | 93 | 23 | 27 | 32 |
| OSL IR depletion ratio < 1 at 2σ | 4 | 2 | 0 | 7 | 1 | 12 | 5 | 4 | 7 | 8 | 5 | 0 | 27 | 42 |
| Recuperation > 5% | 1 | 2 | 0 | 0 | 0 | 6 | 0 | 1 | 6 | 2 | 0 | 4 | 3 | 7 |
| Anomalous dose response | 25 | 12 | 19 | 54 | 14 | 35 | 28 | 23 | 32 | 37 | 39 | 76 | 49 | 51 |
| Saturated grains | 2 | 0 | 1 | 7 | 0 | 16 | 17 | 3 | 6 | 57 | 83 | 16 | 37 | 6 |
| Zero-dose grains | 2 | 0 | 0 | 0 | 0 | 5 | 5 | 3 | 3 | 1 | 1 | 10 | 4 | 16 |
| **Sum of rejected grains** | 1007 | 267 | 267 | 305 | 219 | 2204 | 414 | 240 | 442 | 376 | 372 | 1459 | 1542 | 2373 |
| **Sum of accepted grains** | 93 | 33 | 133 | 195 | 81 | 96 | 86 | 60 | 58 | 124 | 128 | 41 | 58 | 27 |

[a] $T_n$, OSL signal measured in response to the test dose given after stimulation of the natural OSL signal ($L_n$).

**Table S3** Dose rate details for each OSL sample.

| Sample number [a] | Field sample code | Stratigraphic unit | Grain size (□m) | Moisture content (%) [b] | Beta dose rate (Gy/ka) [c] | Gamma dose rate (Gy/ka) [d] | Cosmic-ray dose rate (mGy/ka) [e] | Total dose rate (Gy/ka) [f] |
|---|---|---|---|---|---|---|---|---|
| 3 | CMC14-3 | S | 180–212 | 14 | 0.72 ± 0.04 | 0.38 ± 0.02 | 9 ± 4 | 1.14 ± 0.04 |
| 4 | CMC14-4 | Q | 180–212 | 17 | 0.57 ± 0.03 | 0.35 ± 0.02 | 9 ± 4 | 0.96 ± 0.04 |
| 6 | CMC14-6 | M | 180–212 | 20 | 0.60 ± 0.04 | 0.42 ± 0.02 | 8 ± 4 | 1.06 ± 0.05 |
| 8 | CMC14-8 | L | 180–212 | 16 | 0.53 ± 0.03 | 0.47 ± 0.02 | 8 ± 4 | 1.04 ± 0.04 |
| 9 | CMC14-9 | K | 180–212 | 23 | 0.57 ± 0.04 | 0.35 ± 0.02 | 8 ± 4 | 0.96 ± 0.05 |
| 11 | CMC14-11 | G | 180–212 | 74 | 0.61 ± 0.07 | 0.42 ± 0.05 | 5 ± 2 | 1.06 ± 0.09 |
| 12 | CMC14-12 | F | 180–212 | 34 | 1.48 ± 0.12 | 0.63 ± 0.05 | 7 ± 3 | 2.15 ± 0.13 |
| 23 | CMC18-1 | F | 180–212 | 32 | 1.43 ± 0.11 | 0.89 ± 0.07 | 7 ± 3 | 2.36 ± 0.13 |
| 24 | CMC18-2 | F | 180–212 | 37 | 0.85 ± 0.07 | 0.66 ± 0.05 | 7 ± 3 | 1.55 ± 0.09 |
| 15 | CMC14-15 | D | 180–212 | 44 | 2.74 ± 0.25 | 0.97 ± 0.09 | 5 ± 3 | 3.75 ± 0.27 |
| 16 | CMC14-16 | C | 180–212 | 49 | 2.50 ± 0.24 | 1.00 ± 0.10 | 5 ± 3 | 3.53 ± 0.26 |
| 18 | CMC14-18 | B | 180–212 | 72 | 1.50 ± 0.18 | 0.74 ± 0.09 | 4 ± 2 | 2.27 ± 0.20 |
| 19 | CMC14-19 | B | 180–212 | 64 | 1.62 ± 0.18 | 0.80 ± 0.09 | 5 ± 2 | 2.46 ± 0.20 |
| 20 | CMC14-20 | B | 180–212 | 36 | 1.18 ± 0.10 | 0.96 ± 0.08 | 6 ± 3 | 2.17 ± 0.12 |

[a] Corresponds to the sample number shown in Fig. 5.

[b] Based on the measured (field) moisture content. A relative uncertainty of ± 25% was assigned to this value.

[c] Determined using beta-counting, following Jacobs and Roberts (2015).

[d] Measured in the field using an ORTEC DigiDART-LF portable gamma spectrometer.

[e] Estimated following Prescott and Hutton (1994), accounting for geomagnetic latitude and thickness of sediment and rock overburden.

[f] An assumed internal dose rate of 0.03 ± 0.01 Gy/ka is included in the total dose rate for each sample.

**Table S4** Total dose rate, equivalent dose and age estimate for each OSL sample.

| Sample number [a] | Field sample code | Stratigraphic unit | Total dose rate (Gy/ka) | Number of accepted / measured grains | OD (%) [b] | $D_e$ (Gy) [b] | Age (ka) [c] |
|---|---|---|---|---|---|---|---|
| 3 | CMC14-3 | S | 1.14 ± 0.04 | 93 / 1100 | 17 ± 2 | 29.6 ± 0.8 | 26.0 ± 1.3 |
| 4 | CMC14-4 | Q | 0.96 ± 0.04 | 33 / 300 | 18 ± 4 | 24.5 ± 1.1 | 24.7 ± 1.6 |
| 6 | CMC14-6 | M | 1.06 ± 0.05 | 133 / 400 | 31 ± 2 | 32.7 ± 1.0 | 30.8 ± 1.7 |
| 8 | CMC14-8 | L | 1.04 ± 0.04 | 195 / 500 | 35 ± 2 | 37.5 ± 1.1 | 36.0 ± 1.9 |
| 9 | CMC14-9 | K | 0.96 ± 0.05 | 81 / 300 | 24 ± 3 | 40.3 ± 1.4 | 42.0 ± 2.6 |
| 11 | CMC14-11 | G | 1.06 ± 0.09 | 96 / 2300 | 44 ± 4 | 54.5 ± 2.8 | 51.3 ± 5.2 |
| 12 | CMC14-12 | F | 2.15 ± 0.13 | 86 / 500 | 39 ± 4 | 90.7 ± 4.5 | 42.2 ± 3.3 |
| 13 | CMC18-1 | F | 2.36 ± 0.13 | 60 / 300 | 40 ± 5 | 94.8 ± 5.6 | 40.3 ± 3.3 |
| 14 | CMC18-2 | F | 2.17 ± 0.12 | 58 / 500 | 35 ± 4 | 70.2 ± 3.7 | 45.4 ± 3.7 |
| 15 | CMC14-15 | D | 3.75 ± 0.27 | 124 / 500 | 39 ± 4 | 209.4 ± 9.2 | 55.8 ± 4.8 |
| 16 | CMC14-16 | C | 3.53 ± 0.26 | 128 / 500 | 34 ± 3 | 228.5 ± 8.6 | 64.7 ± 5.5 |
| 18 | CMC14-18 | B | 2.27 ± 0.20 | 41 / 1500 | 36 ± 6 | 143.1 ± 10.5 | 63.0 ± 7.3 |
| 19 | CMC14-19 | B | 2.46 ± 0.20 | 58 / 1600 | 60 ± 7 | 156.6 ± 13.7 | 63.8 ± 7.8 |
| 20 | CMC14-20 | B | 2.17 ± 0.12 | 27 / 2400 | 52 ± 10 | 160.6 ± 19.1 | 73.9 ± 9.9 |

[a] Corresponds to the sample number shown in Fig. 5.

[b] Overdispersion (OD) and equivalent dose ($D_e$) values calculated using the central age model of Galbraith et al. (1999).

[c] Mean ± standard error (1□). A relative error of 2% is included in the age uncertainty to allow for possible bias in beta-source calibration.

**Table S5** Radiocarbon age determinations.

| Sample code | Waikato lab code | Sample depth (m) | Stratigraphic unit | Material | Family | Species | Age ($^{14}$C yr BP) | Calibrated age range (yr cal BP) | |
|---|---|---|---|---|---|---|---|---|---|
| | | | | | | | | 68.2% CI | 95.4% CI |
| V14-1 | WK43309 | 0.42 | T, lower | Whole shell | Viviparidae | *Filopaludina boettgeri* | 15,898 ± 43 | 19,250-19,060 | 19,360-18,980 |
| V14-2 | WK43310 | 0.53–0.55 | R, upper | Charcoal | – | – | 17,274 ± 63 | 20,940-20,710 | 21,050-20,610 |
| V14-3 | WK43311 | 0.79–0.82 | P | Whole shell | Pachychilidae | *Brotia* sp. | 18,242 ± 55 | 22,230-21,980 | 22,320-21,880 |
| V14-4 | WK43312 | 0.79–0.82 | P | Whole shell | Viviparidae | *Bellamya quadrata* sp. | 16,833 ± 48 | 20,420-20,200 | 20,500-20,100 |
| V14-5 | WK43313 | 0.90–0.95 | O | Charcoal | – | – | 17,922 ± 70 | 21,910-21,680 | 22,030-21,550 |

| Thin-Section | Fabric unit/ LSU | Micro-structure | Fabric | Groundmass | Material of biological origin | Primary mineral components | Authigenic minerals | Origin of deposit | Post-depositional alteration |
|---|---|---|---|---|---|---|---|---|---|
| 3A | LSU A | Vughy/ channel<br><br>Porosity = 30% | Spongey | Buff/grey brown isotropic diamict<br><br>C/f † 50 microns = 10% | Bone/shell pseudomorphs, guano from overlying layer (LSUB) | Varied sedimentary/ metamorphic gravel clasts (30%), quartz sand | Extensive clast alteration, irregular nodules within groundmass | Diamict of uncertain origin | Extensive bioturbation, guano-driven phosphatic diagenesis |
| 3B | LSU A | Vughy/ channel<br><br>Porosity = 30% | Spongey | Buff/grey brown, isotropic diamict<br><br>C/f 50 microns = 10% | Bone/shell pseudomorphs, guano derived leachates from overlying layer (LSUB), amorphous organic matter | Sedimentary/ metamorphic gravel clasts (30%), quartz sand | Extensive clast alteration, irregular nodules within groundmass | Diamict of uncertain origin | Extensive bioturbation, guano-driven phosphatic diagenesis |
| | LSU B | Vughy/ channel<br><br>Porosity = 40% | Spongey | Reddish isotropic silt/dusty clay with oxide staining<br><br>C/f 50 microns <2% | Guano | Quartz sand, v. occa. gravel clasts concentrated towards lower boundary, clay aggregates | Void infills, nodules within groundmass, carbonate clast alteration | Waterlogged guano, subsequently oxidised | Gypsum precipitation, oxide precipitation, extensive bioturbation, Phosphate authigenesis |
| 3C | LSU B | Vughy/ channel<br><br>Porosity = 40% | Spongey, Laminar fabric (<5%) | Reddish isotropic silt/dusty clay with oxide staining<br><br>C/f 50 microns <2% | Guano | Quartz sand, v. occa. gravel clasts concentrated towards lower boundary, clay aggregates | Void infills, nodules within groundmass, carbonate clast alteration | Waterlogged guano, subsequently oxidised | Gypsum precipitation, oxide precipitation, extensive bioturbation, phosphate authigenesis |
| 2A | LSU B<br><br>(lowest fabric unit) | Vughy/channel<br><br>Porosity = 25% | Spongey, passage features | Reddish isotropic silt/clay, Quartz sand <2%<br><br>C/f 50 microns <2% | Guano | Quartz sand, clay | Oxide hypocoatings,, varied phosphate nodules within groundmass | Waterlogged guano deposit, subsequently oxidised | Extensive bioturbation, phosphatic diagenesis |

| Thin-Section | Fabric unit/ LSU | Micro-structure | Fabric | Groundmass | Material of biological origin | Primary mineral components | Authigenic minerals | Origin of deposit | Post-depositional alteration |
|---|---|---|---|---|---|---|---|---|---|
| | | | | | | | | | |
| 2B | LSU B<br><br>(middle fabric unit) | Vughy/ channel<br><br>Porosity = 30% | Spongey, nodular | Nodules within isotropic silt matrix, clay forming sub-rounded to subangular nodules<br><br>C/f 50 microns <2% | Guano<br><br>Siliceous plant-derived material, diatoms, clay lined passage features. | Quartz sand, clay | Varied phosphate nodules, clay nodules | Guano deposited in saturated/extremely wet conditions with fluctuating redox environment | Silicate weathering, Al phosphate precipitation, bioturbation |
| | LSU B<br><br>(upper fabric unit) | Vughy/channel<br><br>Porosity = 30% | Spongey | Reddish isotropic silt/clay, Quartz sand <2%<br><br>C/f 50 microns <2% | Guano | Quartz sand, clay | Oxide hypocoatings,, varied phosphate nodules within groundmass | Waterlogged guano deposit, subsequently oxidised | Extensive bioturbation, |
| 2B | LSU B | Vughy/ channel<br><br>Porosity = 30% | Spongey | Reddish isotropic silt/clay, Quartz sand <2%, areas of greyish isotropic silt/clay <20% of groundmass grading towards upper<br><br>C/f 50 microns <2% | Guano | Quartz sand, clay | Oxide hypocoatings, varied phosphate nodules within groundmass | Waterlogged guano, subsequently oxidised | Extensive bioturbation, |
| 2C | LSU B | Vughy/channel<br><br>Porosity = 30% | Spongey | Reddish isotropic silt/clay, Quartz sand <2%, areas of greyish isotropic silt/clay <20% of groundmass grading towards upper<br><br>C/f 50 microns <2% | Guano, | Quartz sand, clay | Oxide hypocoatings,, varied phosphate nodules within groundmass | Guano deposited in very wet/saturated conditions with fluctuating redox conditions | Bioturbation, silicate weathering, taranakite formation |
| | LSU C | Vughy/ channel<br><br>Porosity = 20% | Spongey/ nodular | Sand-sized nodules within isotropic silt matrix, clay forming | Clay lined passage features, possible burrow? | Quartz sand, clay | Varied phosphate nodules, occasional… | Guano deposited in very wet, oxic environment | Bioturbation, Silicate weathering, taranakite… |

| Thin-Section | Fabric unit/ LSU | Micro-structure | Fabric | Groundmass | Material of biological origin | Primary mineral components | Authigenic minerals | Origin of deposit | Post-depositional alteration |
|---|---|---|---|---|---|---|---|---|---|
| 2C (cont.) | | | | sub-rounded to… subangular nodules<br><br>C/f 50 microns <2% | | | …orthic/anorthic oxide nodules, hypocoatings and oxide depletion hypocoatings | | …nodule formation |
| 1A | Lower, C | Vughy/channel<br><br>Porosity = 20% | spongey, laminar (10%) | Sand-sized nodules within isotropic silt matrix, clay forming sub-rounded to subangular nodules and amorphous, laminated concentrations<br><br>C/f 50 microns <2% | Siliceous plant-derived material | Quartz sand, clay | Varied phosphate nodules, amorphous siliceous void infills, varied multi-phase void infills | Guano deposited in very wet, oxic environment | Bioturbation, colluviation, Silicate weathering, Taranakite precipitation, bioturbation |
| | Upper, C | Vughy/channel<br><br>Porosity = 20% | Spongey, laminar (10%) | Sand-sized nodules within isotropic silt matrix, clay forming sub-rounded to subangular nodules and amorphous, quasi-laminated concentrations<br><br>C/f 50 microns <2% | Siliceous plant-derived material, occa. Root pseudomorphs, unidentified siliceous aggregates | Quartz sand, clay | Varied phosphate nodules, amorphous opal void infills , varied multi-phase void infills | Guano deposited in very wet, oxic environment | Bioturbation, colluviation, Silicate weathering, Al phosphate precipitation, bioturbation |
| 1B | C | Vughy/channel<br><br>Porosity = 30% | Spongey, laminar (<10%) | Sand-sized nodules within isotropic silt matrix, dusty clays form sub-rounded nodules and amorphous, quasi-laminated concentrations, Quartz sand (<2%) | Iron replaced root pseudomorphs, siliceous plant-derived material | Quartz sand, clay | Varied phosphate nodules, laminations and coatings, silicate void infills, varied multi-phase void infills | Guano deposited in very wet, oxic environment | Bioturbation, colluviation, Silicate weathering, Al phosphate precipitation, bioturbation |

| Thin-Section | Fabric unit/ LSU | Micro-structure | Fabric | Groundmass | Material of biological origin | Primary mineral components | Authigenic minerals | Origin of deposit | Post-depositional alteration |
|---|---|---|---|---|---|---|---|---|---|
| 1B (cont.) | | | | C/f 50 microns <2% | | | | | |
| 1C | C | vughy/ channel,<br><br>porosity = 30% | Spongey | Sand-sized nodules within isotropic silt matrix, clay forming sub-rounded to subangular nodules and amorphous, laminated concentrations Quartz sand<br><br>C/f 50 microns <2% | some unusual aggregates, Iron replaced root pseudomorphs, rare charcoal, fractured *in-situ* | Quartz sand, clay | Varied phosphate nodules, amorphous opal void infills (?), varied multi-phase void infills | Guano deposited in very wet, oxic environment | Bioturbation, colluviation, Silicate weathering, Al phosphate precipitation, bioturbation |
| | LSU D | Vughy/channel<br><br>Porosity 25% | Laminar | C/f 50 microns <2% | Organic punctuations, amorphous oxidised organic matter, pellety microaggregates | Clay | | Guano and translocated clays deposited in wet conditions/Standing water, subsequent drying | Water sorting, Post depositional drying/cracking |
| 6A | LSU G | Vughy/channel<br><br>Porosity = 20% | Double-spaced fine enaulic to gefuric | Reddish brown isotropic silt and clay, red grading towards bottom w/ clays<br><br>C/f 50 microns = 5% | Sand sized altered bone, guano | Carbonate sand/gravel, quartz sand | Varied nodules within groundmass, small, weathered phosphate nodules, anorthic Fe/Mn nodules | Colluvially deposited material from guano mound, accumulation of auto- and allogenic material upon moist, colluvial cave floor environment | Extensive bioturbation, decalcification of groundmass |
| 6B | Lower, LSU H | Vughy/channel<br><br>Porosity = 20% | Spongey to Double-spaced fine enaulic | Grey/Brown isotropic silt w/ sub angular- sub-rounded clay nodules<br><br>C/f 50 microns = 2%% | Sand sized altered bone | Quartz sand v. weathered. | Varied nodules within groundmass, , weathered phosphate nodules, anorthic Fe/Mn nodules concentrated at upper boundary | Decalcification of colluvially deposited ashy sediment due to episodic saturation by phosphate rich groundwater. | Extensive bioturbation, decalcification of groundmass, oxide precipitation |

| Thin-Section | Fabric unit/ LSU | Micro-structure | Fabric | Groundmass | Material of biological origin | Primary mineral components | Authigenic minerals | Origin of deposit | Post-depositional alteration |
|---|---|---|---|---|---|---|---|---|---|
| 6B (cont.) | Upper, LSU H | Vughy/channel<br><br>Porosity = 20% | Double-spaced fine enaulic to spongey | Grey/Brown silt, welded calcitic b-fabric<br><br>C/f 50 microns = 5% | Sand sized altered bone, fractured *in-situ* | Micritic calcite ashes, quartz sand, occa. Carbonate sand | Quartz sand concentrations with oxides, Nodule w/ reaction rims | Colluvially deposited ashes with autogenic and allogenic, carbonate rich silt. | Extensive bioturbation, weathering of nodules. Formation of solid layer from carbonate recystallisation |
| 5A | Lower, LSU L | Vughy/ channel<br><br>Porosity = 15% | Double-spaced fine enaulic. Restricted area of laminations | Grey/Brown silt, welded calcitic b-fabric<br><br>C/f 50 microns = <5% | Sand-sized altered bone showing heating, passage features infilled w/ phosphatic material,<br>Ashy dumps | Quartz sand minor weathering, fractured clay aggregates, burned soil aggregates | Phosphatic crust formed at upper boundary, oxides precipitated below crust, varied nodules, minor angular charcoal fragments | Ashy occupation waste deposited via slopewash, accumulation of carbonate rich auto- and allogenic material on cave floor | Extensive bioturbation, ash recrystallisation. phosphate crust formed at contact with overlying deposit. Quartz weathering |
| | Upper, M | Vughy/ channel<br><br>Porosity = 15% | Double-spaced fine enaulic to spongey | Pinkish silt, weakly-expressed stipple-specked b-fabric<br><br>C/f 50 microns = 5% | Sand-sized cooked bone; shell, aggregates of oxidised iron-replaced organic matter, oxide replaced root pseudomorphs | Weathered quartz | Calcite hypocoatings, Anorthic nodules, | Guano deposition with continued colluvial deposition of carbonate rich auto- and allogenic material on cave floor | Extensive bioturbation, limited diagenesis, phosphatisation of carbonate fines |
| 5B | Lower, M | Vughy/ channel<br><br>Porosity = 15% | Spongey | Pinkish silt, weakly-expressed stipple-specked b-fabric<br><br>C/f 50 microns = 5% | Oxidised, iron-replaced organic matter | Quartz sand and fine gravel showing extensive weathering, soil aggregates | Calcite hypocoatings, Anorthic nodules | Guano deposition with continued accumulation of carbonate rich auto- and allogenic material on cave floor | Extensive bioturbation, limited phosphatc diagenesis |
| | Middle, N | Vughy/ channel<br><br>Porosity = 10% | Spongey | Grey silt, welded calcitic b-fabric<br><br>C/F 50 microns = 2% | Sand-sized degraded bone, Microcharcoal, organic punctuations | Quartz sand | Welded b-fabric, passage features | Syn-depositionally reworked ashy occupation waste | Extensive bioturbation, cementing of calcite through water movement |
| | Upper, O | Vughy/channel | Double-spaced fine enaulic | Buff-grey silt, stipple specked b-fabric | Sand-sized to gravel sized shell fragments, | Sub-angular coarse carbonate sand, quartz… | NA | Accumulation of carbonate rich auto- and allogenic… | Limited bioturbation |

| Thin-Section | Fabric unit/ LSU | Micro-structure | Fabric | Groundmass | Material of biological origin | Primary mineral components | Authigenic minerals | Origin of deposit | Post-depositional alteration |
|---|---|---|---|---|---|---|---|---|---|
| 5b (cont.) | | Porosity = 5% | | C/f 50 microns = 5% | Sand-sized charcoal fragments, organic punctuations | …sand, burned and unburned soil aggregates | | …material in dusty, cave floor environment | |
| 4A | Lower, Q | Vughy/ Channel<br><br>Porosity = 20% | Double-spaced fine enaulic | Brown silt, welded calcitic b-fabric<br><br>C/f 50 microns = 10% | Infrequent sand-sized shell frags, infrequent cooked and uncooked bone, microcharcoal | Carbonate sand/gravel, quartz sand | NA | Accumulation of carbonate rich auto- and allogenic material in dusty, cave floor environment | Bioturbation |
| | Upper, R | Vughy /Channel<br><br>Porosity = 20% | Double-spaced fine enaulic | Brown silt, welded calcitic b-fabric<br><br>C/f 50 microns = <5% | Sand/gravel sized shell frags, cooked and uncooked sand-sized bone, charcoal showing varied preservation | Carbonate sand/gravel, quartz sand | Clays within humified charcoal, occa. Calcite pseudmorphs of shell | Ashy occupation debris | Bioturbation, humification |
| 4B | Lower, R | Vughy /Channel<br><br>Porosity = 10% | Double-spaced fine enaulic to spongey | Pinkish silt, welded calcitic b-fabric<br><br>C/f 50 microns = <10% | Infrequent Sand sized shell frags, cooked and uncooked sand-sized bone, charcoal (varied preservation) | Carbonate sand/gravel, quartz sand, soil aggregates (occasionally burned) | Sand sized irregular nodules throughout groundmass | Accumulation of carbonate rich auto- and allogenic material in dusty, cave floor environment, anthropogenic inclusions | Bioturbation |
| | Upper, S | Vughy/Channel<br><br>Porosity = 20% | Spongey | Grey-brown and red-brown silt, undifferentiated b-fabric with weakly expressed stipple specked b-fabric grading upwards<br><br>C/f 50 microns = 5% | Humified organic matter, aggregates of plant pseudomorphs, occasional charcoal fragments | Quartz sand, occa. Coarse carbonate sand w/ weakly expressed reaction rims, soil aggregates | Ashy void coatings, calcite hypocoatings, irregular nodules throughout groundmass | Decalcified sediment w/ significant guano component, post-depositional carbonate transport. | Bioturbation, decalcification |

† C/f = coarse/fine ratio

**Table S6 (Above)**: A summary of the results of micromorphological analysis of thin-section samples. Descriptions follow Stoops (2003).

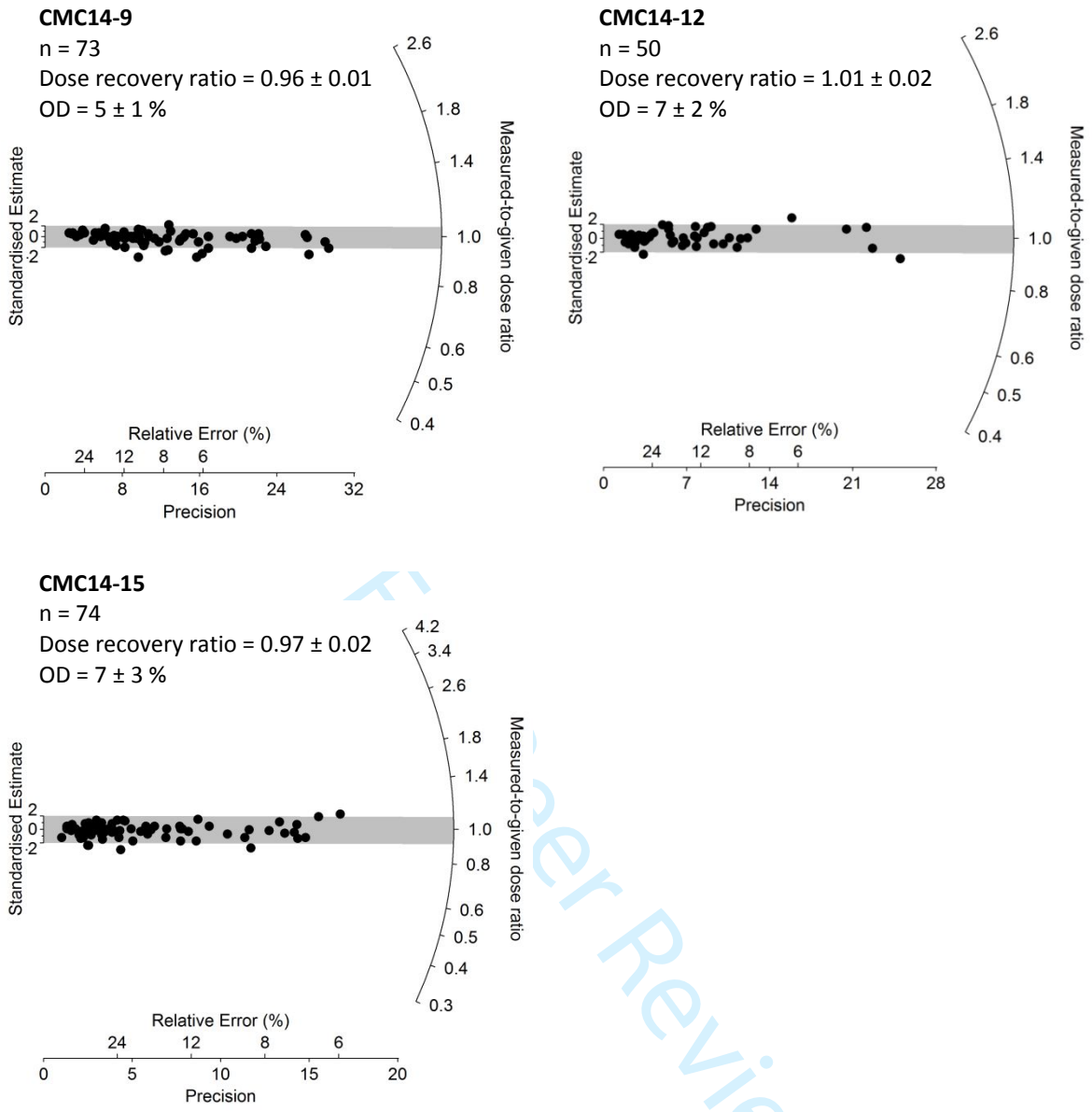


**Figure S1** Results of dose recovery tests for three representative samples, displayed as radial plots (Galbraith et al., 1999). Individual quartz grains of each sample were first bleached under a solar simulator for 1 hr to reset the natural OSL signals, and then given a beta dose close to their expected natural $D_e$ value, to act as a surrogate natural dose. The irradiated grains were then preheated and measured using the single-aliquot regenerative-dose procedure listed in Table S1. The resulting dose values are shown as filled circles and the grey bands are centred on a dose recovery ratio of unity. Grains with measured doses equal to the given dose have measured-to-given dose ratios equal to 1. If the measurement errors are sufficient to account for the observed scatter among the individual dose values at 2σ, then 95% of the data points should fall within the grey bands. Additional scatter is referred to as 'overdispersion' (OD, or $\sigma_b$ in the statistical notation of Galbraith et al., 2005), which ranges between 5 ± 1% and 7 ± 3% for these three samples.

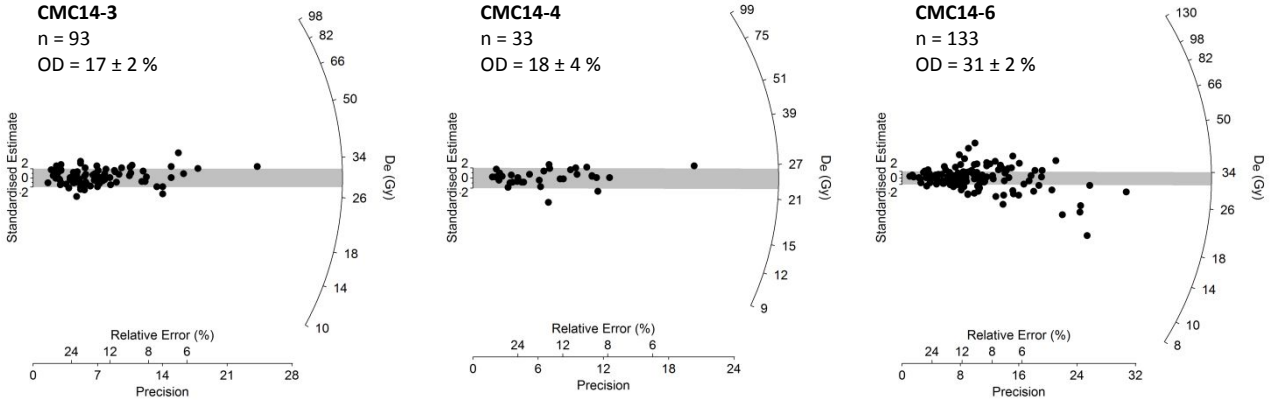
CMC14-3
n = 93
OD = 17 ± 2 %
CMC14-4
n = 33
OD = 18 ± 4 %
CMC14-6
n = 133
OD = 31 ± 2 %
Standardised Estimate
De (Gy)
Relative Error (%)
Precision

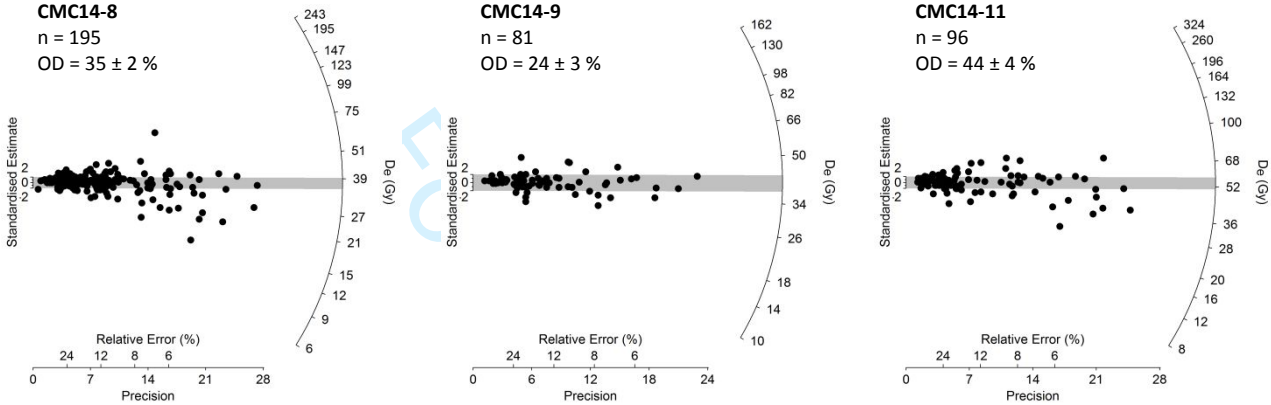
CMC14-8
n = 195
OD = 35 ± 2 %
CMC14-9
n = 81
OD = 24 ± 3 %
CMC14-11
n = 96
OD = 44 ± 4 %
Standardised Estimate
De (Gy)
Relative Error (%)
Precision

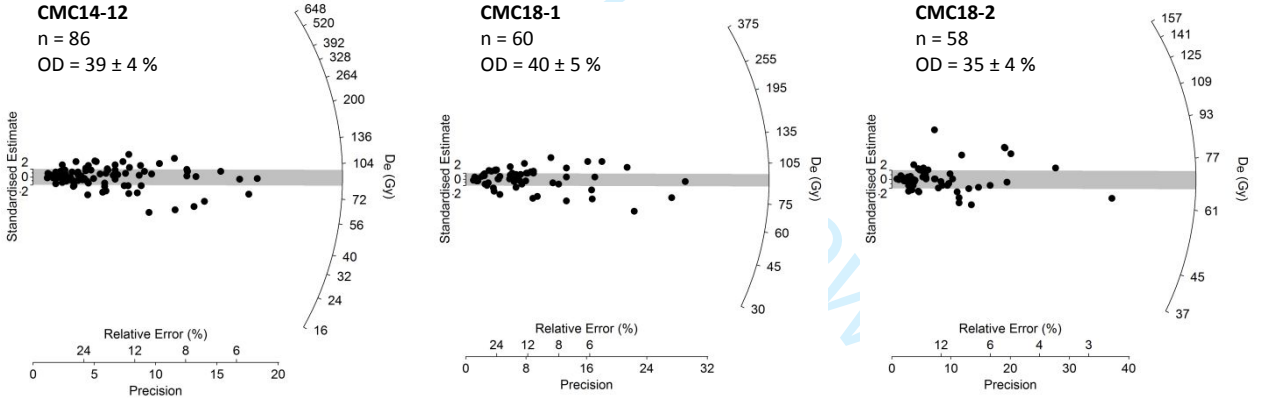
CMC14-12
n = 86
OD = 39 ± 4 %
CMC18-1
n = 60
OD = 40 ± 5 %
CMC18-2
n = 58
OD = 35 ± 4 %
Standardised Estimate
De (Gy)
Relative Error (%)
Precision

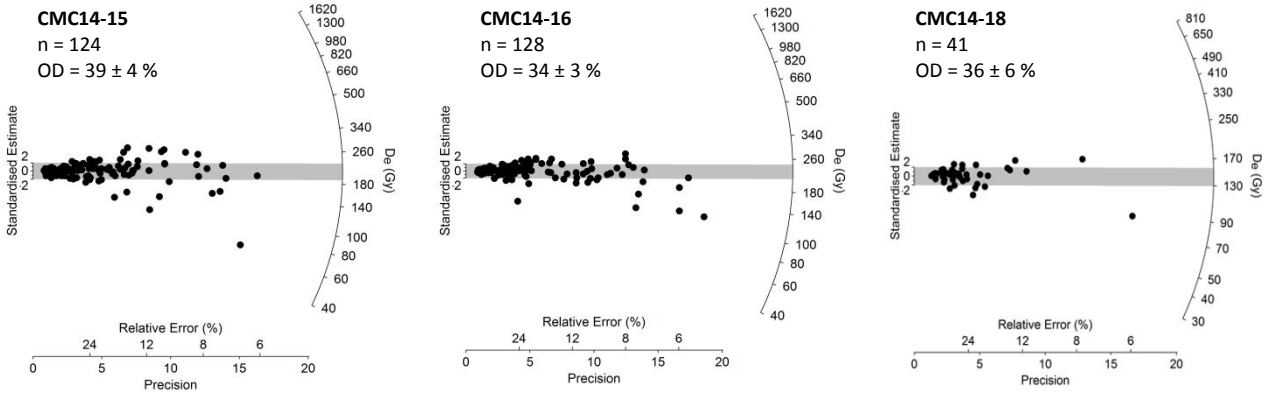
CMC14-15
n = 124
OD = 39 ± 4 %
CMC14-16
n = 128
OD = 34 ± 3 %
CMC14-18
n = 41
OD = 36 ± 6 %
Standardised Estimate
De (Gy)
Relative Error (%)
Precision

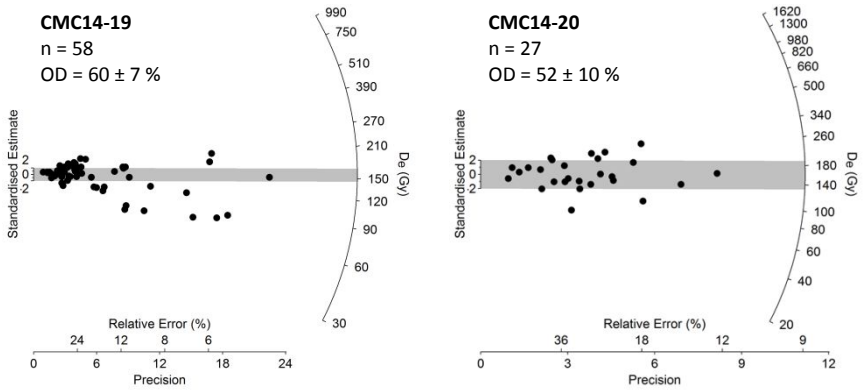


**Figure S2** Radial plots of the $D_e$ distribution for each of the 14 samples. The grey bands are centred on the weighted mean $D_e$ values determined using the central age model (Galbraith et al., 1999).

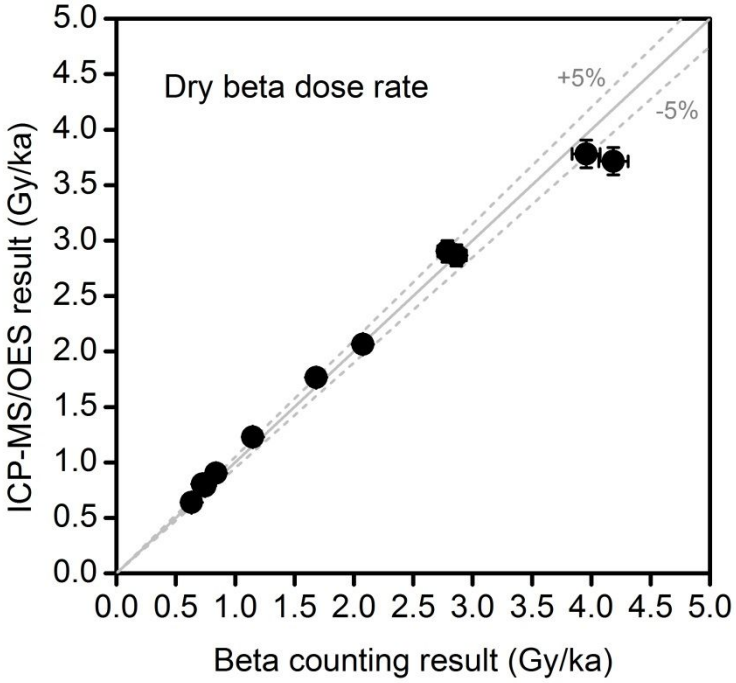


**Figure S3** Beta dose rates derived from beta-counting and inductively-coupled plasma mass spectrometry/optical emission spectroscopy (ICP-MS/OES) for 11 of the OSL samples. Error bars are at 1σ. For both methods, samples were dried and powdered (to ensure homogeneity) prior to measurement. The solid line shows the 1:1 ratio and the dashed lines denote deviations of ± 5% from this ratio.